Chirality effects in transition metal monogermanides and -silicides

Dissertation
zum Erlangen des Doktorgrades
des Fachbereichs Physik
der Universität Hamburg

vorgelegt von
Sven-Arne Siegfried
aus Braunschweig

Hamburg
2016

Gutachter der Dissertation:
Prof. Dr. Andreas Schreyer
Prof. Dr. Sergey V. Grigoriev

Gutachter der Disputation:
Prof. Dr. Andreas Schreyer
Prof. Dr. Sergey V. Grigoriev
Dr. Dieter Lott
Prof. Dr. Daniela Pfannkuche
Prof. Dr. Andreas Stierle

Datum der Disputation:
11. November 2016

Vorsitzender des Fach-Promotionsausschusses PHYSIK
Prof. Dr. Wolfgang Hansen

Dekan der MIN-Fakultät:
Prof. Dr. Heinrich Graener

Kurzfassung

In der folgenden Doktorarbeit werden die Ergebnisse der Analyse des Zusammenspieles zwischen der strukturellen und magnetischen Chiralität in den verschiedenen Übergangsmetallmonogermaniden und -monosiliziden: $\mathrm{Mn}_{1-x}\mathrm{Fe}_x\mathrm{Ge}$, $\mathrm{Fe}_{1-y}\mathrm{Co}_y\mathrm{Ge}$ und $\mathrm{Fe}_{1-z}\mathrm{Co}_z\mathrm{Si}$ präsentiert. Unterhalb der Ordnungstemperatur T_c weisen diese kubischen B20 Verbindungen, die über keine Inversionssymmetrie verfügen, eine helikale (homochirale) Spinstruktur auf, die auf dem konkurrierenden Zusammenspiel zwischen der starken ferromagnetischen (FM) Wechselwirkung J mit der schwächeren Dzyaloshinskii-Moriya (DM) Austauschwechselwirkung D basiert. Resonante Röntgendiffraktion und polarisierte Neutronenstreuung wurden angewendet, um die strukturelle Γ_C und magnetische γ_m Chiralitäten zu bestimmen. Die mikroskopischen Messungen wurden dabei durch makroskopische magnetische SQUID Messungen ergänzt. Für alle untersuchten Materialsysteme konnte der experimentelle Nachweis erbracht werden, dass der Zusammenhang zwischen den beiden Chiralitäten ($\Gamma_c \leftrightarrow \gamma_m$) von den $3d$-Elementen abhängt. Für die Systeme, die auf Mn und Co basieren, sind die kristalline und magnetische Chiralität gleich ($\Gamma_c \times \gamma_m = +1$), während für Systeme, die auf Fe basieren ($\Gamma_c \times \gamma_m = -1$) das Gegenteil der Fall ist. Zusammen mit der Fähigkeit die strukturelle Chiralität der Monosilizide mittels Czochralski-Methode zu kontrollieren, zeigen die hier präsentierten Ergebnisse die Möglichkeit, die chirale magnetische-Gitter Kopplung phänomenologisch durch die DM abgebildet, für zukünftige spintronische Bauelemente zu nutzen, die auf der elektrischen Ladung und dem magnetischen Moment des Elektrons basieren (wie es z. B. im magnetischen "Racetrack" Speicher realisiert werden könnte). In allen Verbindungen zeigt der spirale Wellenvektor $k_s = 2\pi/d$, mit der Helixlänge d, eine starke Konzentrationsabhängigkeit seiner Größe. Die Möglichkeit diese zu variieren ist von großem Interesse für maßgeschneiderte Werkstoffe. Der absolute Wert von $|\boldsymbol{k}_s|$ wird bei einer bestimmten Konzentration zu null. Damit einhergehend ändert die Kopplung zwischen struktureller und magnetischer Chiralität ihr Vorzeichen. Das monotone Verhalten des Wellenvektors führt zu der Schlussfolgerung, dass die DM Wechselwirkung ebenfalls zu null wird. Der Wellenvektor $k_s = 0$ bei den kritischen Konzentrationen x_c, y_c, z_c, sowie der Nachweis einer magnetischen Ordnung durch die SQUID Messungen, deuten darauf hin, dass bei $x, y, z \rightarrow x_c, y_c.z_c$ der helikale Zustand in einen ferromagnetischen transformiert wird. Der Unterschied zwischen der FM und der DM Austauschwirkung ist durch den Wellenvektor $k_s = D/J$ gegeben, während die Energiedifferenz zwischen dem helikalen und ferromagnetischen Zustand durch das zweite kritische Feld H_{c2} bestimmt ist, ab welchem die helikal Phase in die Feld-induzierte ferromagnetische Phase übergeht. Die Ergebnisse unterstreichen die wichtige Rolle der kubischen Anisotropie, welche die helikale Struktur, im Bereich kleiner k_s destabilisiert und ebenfalls einen Beitrag

zur Größe des zweiten kritischen Feldes H_{c2} liefert. Basierend auf den experimentellen Ergebnissen, welche in dieser Arbeit vorgestellt werden, konnte die Konkurrenz zwischen der kubischen Anisotropie und der Dzyaloshinskii-Moriya Austauschwirkung als verantwortlicher Mechanismus für die Transformation der helikalen zur ferromagnetischen Anordnung identifiziert werden. Dadurch konnte der experimentelle Nachweis für die notwendige Erweiterung des bisherigen Modells von Bak-Jensen für kubische B20 Helimagnete erbracht werden.

Abstract

The thesis presented here investigates the interplay between structural and magnetic properties of the three different series of transition metal monogermanides and -silicides: $Mn_{1-x}Fe_xGe$, $Fe_{1-y}Co_yGe$ and $Fe_{1-z}Co_zSi$. These non-centrosymmetric cubic B20 compounds show a helical (homochiral) spin structure, based on the competition of the large ferromagnetic-exchange (FM) interaction J and the weaker antisymmetric Dzyaloshinskii-Moriya (DM) interaction D below T_c. Resonant x-ray diffraction has been combined with polarised neutron scattering to determine the structural Γ_c and magnetic γ_m chirality, respectively. The microscopic measurements have been further complemented by macroscopic magnetic SQUID measurements. For all three investigated compounds it could be experimentally demonstrated that the relation between both chiralities ($\Gamma_c \leftrightarrow \gamma_m$) depends on the $3d$-element concentrations. For the Mn-/Co- based compounds the crystalline and magnetic chirality have the same sense ($\Gamma_c \times \gamma_m$= +1), while for the Fe-based compounds the chiralities are opposite to each other ($\Gamma_c \times \gamma_m$= -1). Together with the ability to control the structural chirality in the monosilicide based compounds via the Czochralski method these results show the potential to use the chiral magneto-lattice coupling, mapped phenomenologically as DM, to produce customised magnetic chiral systems for future spintronic applications, using the magnetic moment in addition to the electric charge of the electron (as it might be realised in 'Racetrack' memories for example). In all compounds the absolute value of the spiral wavevector $k_s = 2\pi/d$, where d is the spiral period, shows a large variation in dependence on the concentration of up to two orders of magnitude. The ability to tune the spiral size is of great interest for tailored materials. The absolute value of $|\boldsymbol{k}_s|$ reaches zero at a certain critical concentration accompanied with the switch of the chiral link between structural and magnetic chirality. The monotonic behaviour in respect to the changes in the concentration ratios leads to the conclusion that the DM also becomes zero. The fact that the value of the helical wavevector goes to zero at the critical concentrations x_c, y_c, z_c and the clear evidence for an existing magnetic order from the macroscopic magnetisation measurements suggests a transition from the helical to a ferromagnetic state at $x, y, z \rightarrow x_c, y_c, z_c$. The differences in the two competing interaction FM and DM is given by the wavevector $k_s = D/J$, while the difference in the energies of the helical and the ferromagnetic collinear spin state be experimentally determined by measuring the second critical field H_{c2}, that transforms the helical into a field-induced ferromagnetic phase. The results obtained in this work underline the important role of the cubic anisotropy, which can destabilise the entire helix structure for small k_s and furthermore makes a contribution to the second critical field H_{c2}. Based on the experimental data presented in this work the mechanism responsible for the transformation from the helical to the ferromagnetic spin state is realised

via the competition between the cubic anisotropy and the Dzyaloshinskii-Moriya interaction and delivers the experimental evidence for the extension of the established Bak-Jensen model for cubic B20 helimagnetic systems.

Vorabveröffentlichungen von Ergebnissen der Dissertation

Teilergebnisse aus dieser Arbeit wurden in folgenden Beiträgen vorab veröffentlicht:

Publikationen:

S. V. Grigoriev, N. M. Potapova, S.-A. Siegfried, V. A. Dyadkin, E. V. Moskvin, V. Dmitriev, D. Menzel, C. D. Dewhurst, D. Chernyshov, R. A. Sadykov, L. N. Fomicheva, and A. V. Tsvyashchenko. *Chiral Properties of Structure and Magnetism in* $Mn_{1-x}Fe_xGe$ *Compounds: When the Left and the Right are Fighting, Who Wins?*, Phys. Rev. Lett. **110**, 207201 (2013).

S. V. Grigoriev, S.-A. Siegfried, E. V. Altynbayev, N. M. Potapova, V. Dyadkin, E. V. Moskvin, D. Menzel, A. Heinemann, S. N. Axenov, L. N. Fomicheva, and A. V. Tsvyashchenko. *Flip of spin helix chirality and ferromagnetic state in* $Fe_{1-x}Co_xGe$ *compounds*, Phys. Rev. B **90**, 174414 (2014).

S.-A. Siegfried, E. V. Altynbaev, N. M. Chubova, V. Dyadkin, D. Chernyshov, E. V. Moskvin, D. Menzel, A. Heinemann, A. Schreyer, and S. V. Grigoriev. *Controlling the Dzyaloshinskii-Moriya interaction to alter the chiral link between structure and magnetism for* $Fe_{1-x}Co_xSi$, Phys. Rev. B **91**, 184406 (2015).

weitere Veröffentlichungen aus Projekten während dieser Dissertation:

Publikationen:

E. Altynbaev, S.-A. Siegfried, V. Dyadkin, E. Moskvin, D. Menzel, A. Heinemann, C. Dewhurst, L. Fomicheva, A. Tsvyashchenko, and S. Grigoriev. *Intrinsic instability of the helix spin structure in MnGe and order-disorder phase transition*, Phys. Rev. B **90**, 174420 (2014).

S. V. Grigoriev, A. S. Sukhanov, E. V. Altynbaev, S.-A. Siegfried, A. Heinemann, P. Kizhe, and S. V. Maleyev. *Spin waves in full-polarized state of Dzyaloshinskii-Moriya helimagnets: Small-angle neutron scattering study*, Phys. Rev. B **92**, 220415(R) (2015).

E. V. Altynbaev, A. S. Sukhanov, S.-A. Siegfried, V. A. Dyadkin, E. V. Moskvin, D. Menzel, A. Heinemann, A. Schreyer, L. N. Fomicheva, A. V. Tsvyashchenko and S. V. Grigoriev. *Doping-induced temperature evolution of a helicoidal spin structure in the MnGe compound*, J. Synch. Investig. **10**, 777 (2016).

Contents

Chapter 1

Introduction

... Perhaps looking-glass milk isn't good to drink ...

in *Through the Looking Glass* by Lewis Carroll [Car], Alice expresses her concern respective the looking-glass milk. Carroll refers to so called *enantiomers*, discovered by Pasteur in 1848 [Pas]. *Enantiomers* are two *stereoisomers* related to each other by mirror reflection. These two molecules consist of the same kinds and number of atoms, but a different orientation in space. Many molecules are chiral and they react different depending on their chirality. Chirality is moreover of critical importance in different scientific fields, some examples will be given in the next passage (see e.g. [Wag] for a more detailed review).

In 2001 Knowles, Noyori and Sharpless received the Noble prize in chemistry for their work on chiral catalysis [Nob]. One of the most fascinating example of chiral molecules is without doubt the deoxyribonucleic acid (DNA), always existing in a right handed screw. The weak nuclear force, which is responsible for the nuclear decay, has the opposite preferred handedness. The prediction by Lee and Yang [LY] in 1956 (Nobel prize in physics 1957) that the parity of weak interaction is violated, could be experimentally verified by Wu and co-workers in 1957 [WAH$^+$]. For this reason, they used the β^- decay of ${}^{60}_{27}\mathrm{Co}\rightarrow {}^{60}_{28}\mathrm{Ni} + e^- + \overline{\nu}_e + 2\,\gamma$ and compared the direction of emitted electrons and gammas with the nuclear spin of the Co. In the same year Goldhaber and co-workers could reveal that all existing neutrinos are left-handed, while all antineutrinos are right-handed [GGS].

In this work the focus will be on another manifestation of chirality: the interplay of structural and magnetic chirality in cubic B20 structures without inversion symmetry. The coupling between structure and magnetism in condensed matter physics was found to be of crucial scientific and technologically interest: the magnetoelastic effect, magnetostriction, magnetoelectric coupling are some examples [Jen, Jou, EWP$^+$]. Another important type of coupling is the chiral one, where a chiral spin structure forms on a chiral crystal lattice [DCGD]. This link has been experimentally demonstrated for a broad variation of itinerant magnets with the cubic space group $P2_13$ like as for example MnSi [IEM+, TTIE], $Mn_{1-x}Fe_xSi$ [GCD+b], $Fe_{1-x}Co_xSi$ [DGM+] or Cu_2OSeO_3 [DPG+]. A further, topologically non-trivial structure can be observed in a certain magnetic field range within the $H-T$ phase diagram of the B20 magnets. Originally described as chiral vortices, these objects are called nowadays *skyrmions*, named after the nuclear physicist Tony Skyrme, who developed a nonlinear field theory of mesons and baryons, showing that topologically stable field configurations occur as a particle like solution [Sky]. A topologically protected, particle-like magnetic structure is highly interesting because of the potential applications in novel spintronic devices, for example, based on its motion. The idea of using moveable magnetic structures for data storage was proposed by Parkin and co-workers as 'Racetrack' memory [Par, PHT]. Originally they suggested to use domains within ferromagnetic wires, coding information in the sequence of the different oriented domain walls (DW). The DW would be electrically moved by a spin polarised current, carrying a spin angular momentum [PJK+] and transferring spin-momentum to the DW [Slo, Bera], that causes the movement of the domain walls [Berb, TK, LZ, ZL, TNMS, BM]. The great advantages of such a memory device are the non-volatility combined with the one-dimensionality of the used wires, allowing a highly increased data storage density as compared with two-dimensional devices, as for example, magnetoresistive random access memory (MRAM) [Åke]. Furthermore, since each wire consists of many bits, one needs just one reading-and-writing unit, while in MRAMS every bit needs his own processing unit. However, the current density necessary to move a ferromagnetic domain wall fast enough is on the order of 10^8 A/cm^2 to be competitive with other technologies [PHT]. Such high current densities, on the other hand, lead to Joule heating in the wires that might cause thermal fluctuations that subsequently cause uncontrolled movements of the domain walls [FYN+]. The topologically protected, particle-like *skyrmions* are here extremely promising candidates to overcome this problem. The current density to move such a magnetic whirl-structure is reported to be five orders of magnitude smaller as it is needed for ferromagnetic DWs [JMP+, FCS]. Notwithstanding the great interest, the helimagnetic structure that forms the basis of the phase diagram in these B20 compounds is still not yet fully understood. Due to the fact that the helical and the *A-phase* are based on the same hierarchy of interactions the understanding of the helical phase will have an important impact on the path of tailoring the *A-phase*. Therefore, further experimental and theoretical work is necessary for a complete picture of the underlying concept. Two experimental techniques, the resonant x-ray diffraction and polarised neutron scattering, are highly suitable to determine the structural Γ_c and magnetic chirality γ_m, respectively. Using a refinement of the so-called Flack-parameter [Fla, FB, SSF], a standard tool of modern crystallographic, the absolute structure of a crystal can be determined. In contrast to electro-magnetic waves, neutrons carry a magnetic moment which makes them a powerful probe for magnetic structures in condensed matter physics. For chiral magnetic structures polarised small angle neutron scattering (SANS) offers unique possibility to directly probe the magnetic handedness. In this work the combination of these two powerful techniques, complemented by superconducting quantum interference device (SQUID) susceptibility measurements, is used to probe the structural and magnetic chirality in three different series of compounds: $Mn_{1-x}Fe_xGe$, $Fe_{1-y}Co_yGe$ and $Fe_{1-z}Co_zSi$. While the monosilicide-based cubic B20 helimagnetic systems, like MnSi, have been studied in detail in the last decades, this was not the case for germanide based compounds due to the complicate and laborious synthesises. Similar to MnSi, the cubic MnGe and FeGe compounds show both a helical structure arising from the Dzyaloshinskii-Moriya interaction, interfering with the ferromagnetic exchange. Nevertheless, the magnetic properties are remarkable different. At $T_c \approx 278.7$ K FeGe transforms from the paramagnetic to an ordered state evincing a long wavelength helical structure with a period of approximate 690 Å. The critical field at which the transition from this helimagnetic structure into a field aligned ferromagnetic occurs is approximately 0.3 Tesla [LBF] and it has a magnetic moment of 1 μ_B per Fe atom at low temperatures [WH]. The pure MnGe compound exhibits remarkably different properties: a very short spiral length of approximate 3 Å below the magnetic ordering temperature of $T_c \approx 140$ K, a high magnetic moment of 1.9 μ_B per Mn atom at 2 K, the field induced transformation from the helical to the ferromagnetic state at above 10 T and a giant Topological Hall Effect [KOA+, MTA+, KKI+]. Recent small angle neutron scattering studies revealed an intrinsic instability of the spiral structure in MnGe along with a complex temperature driven order-disorder phase transition in a temperature range of more than 100 K above the ordering temperature [ASD+], as also reported from studies using Mössbauer spectroscopy [DMH+]. In addition, both MnGe and FeGe manifest a complex pressure induced spin transition due spin fluctuations [DBT+]. Without doubt, a collective understanding of the underlying mechanism generating these wide varieties of magnetic properties is of significant importance. It is well known that for Mn-based silicide-based compounds ($Mn_{1-x}Fe_xSi$ and $Mn_{1-x}Co_xSi$) the crystalline and magnetic chirality have the same sense [IEM+, TTIE, GCD+b], while the connection for Fe-based systems ($Fe_{1-z}Co_zSi$) seems to be opposite for the low Co concentration range [GCD+a]. Pure FeSi and CoSi are not magnetically ordered, for this reason, $Mn_{1-x}Fe_xSi$ and $Mn_{1-x}Co_xSi$ do not allow to prove the hypothesis of different signs of the DM interaction in Mn/Co and Fe based compounds. In contrast to the germanide based compounds, $Mn_{1-x}Fe_xGe$ and $Fe_{1-y}Co_yGe$ are magnetically ordered in a broader concentration range.

In this work, the evolution of the helical magnetic structure in $\mathrm{Mn}_{1-x}\mathrm{Fe}_x\mathrm{Ge}$ by mixing the two kinds of magnetic atoms Fe and Mn from $x = 0.0$ to $x = 1.0$ is investigated. The same approach has been applied to $\mathrm{Fe}_{1-y}\mathrm{Co}_y\mathrm{Ge}$ by substituting the Fe by Co atoms. For both compounds unpolarised SANS measurements have been used to investigate the evolution of the helix wavevector k_s in dependence on the transition metal concentration x and y, respectively. Moreover, the idea of controlling the sign of the DM by using single crystals has been exploited. Due to the fact that powder samples consist of equal amount of grains of both chiralities a determination of the chiral link is just possible in single crystalline samples. Since one is able to fabricate single crystals of sufficient size for the monosilicide series of $\mathrm{Fe}_{1-z}\mathrm{Co}_z\mathrm{Si}$, they turn out as a good candidate to gain full control of the crystalline and magnetic chirality.

All three systems considered within this thesis allow in addition to test the hypothesis by Kataoka and co-workers [NYHK], who pointed out the important role of the weak cubic anisotropy interaction in the case of small wavevector $|\boldsymbol{k}_s|$. In this limited case the interaction between the cubic anisotropy and the Dzyaloshinskii-Moriya interaction should enable the transformation from the spiral to the ferromagnetic spin structure at a certain critical concentration.

In the following, the concept of chirality in general and, in particular, in chiral magnetism will be introduced. Chapter 2 gives a compact overview about the basic principles of the scattering techniques used in this work. In Chapter 3 the fundamental structural properties of the investigated cubic B20 crystals, as well as the used techniques for samples preparation and x-ray characterisation, are presented. In Chapter 4 the results obtained for $\mathrm{Mn}_{1-x}\mathrm{Fe}_x\mathrm{Ge}$, $\mathrm{Fe}_{1-y}\mathrm{Co}_y\mathrm{Ge}$ and $\mathrm{Fe}_{1-z}\mathrm{Co}_z\mathrm{Si}$ are presented. The last chapter summarises this work and give an outlook for future research.

1.1 Chirality

In this chapter a definition of chirality in general and an overview about the magnetic chirality in cubic B20 structures is given.

1.1.1 Inversion symmetry and physical quantities

In physics three fundamental symmetry operations exist corresponding to distinct inversions, namely: parity, time reversal and charge conjugation. The invariance of a physical law under a transformation follows from the invariance of the Hamiltonian H under the same transformation. The inversion of the coordinates of all particles in a system is called parity inversion (operator: P). The replacement of the time coordinates t by $-t$ is called time reversal (operator: T). The interconversion from particle and antiparticle is the so called charge conjunction (operator: C).

In physics a distinction is drawn between *scalar* physical quantities (e.g. energy), with a magnitude but without a direction, *vector* quantities with a magnitude and a direction (e.g. linear momentum $\boldsymbol{p}$) and *tensors* with a magnitude with more than one direction (e.g. stress tensor). If its sign is reversed by P a vector is called *polar* or *true* vector (e.g. position $\boldsymbol{r}$). An *axial* or *pseudovector* is not changed by P, a typical example for a *pseudovector* is the angular momentum $\boldsymbol{L} = \boldsymbol{r} \times \boldsymbol{p}$. If T does not change the sign of the vector it is called *time even* (e.g. $\boldsymbol{r}$), otherwise *time odd* (e.g. $\boldsymbol{p}$ or $\boldsymbol{L}$). The magnetism in condensed matter is usually caused by the spins or the angular moments of electrons, which are both pseudovectors.

1.1.2 Definition of chirality

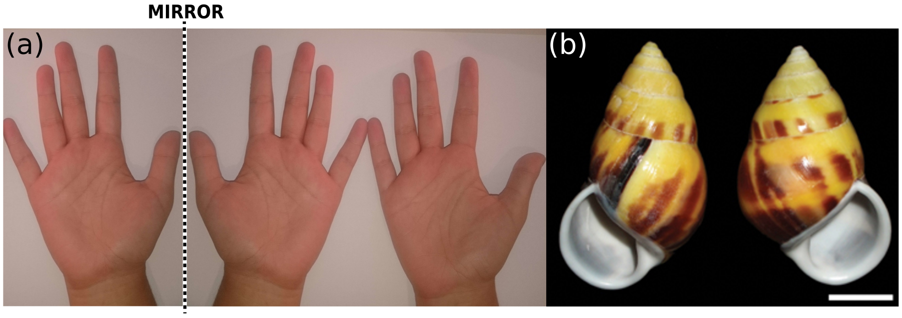

Figure 1.1: (a) Left- and right hand together with the mirror image of the left hand and (b) Sinistral (left) and dextral (right) shells of *Amphidromus perversus* a species with chiral dimorphism (Reprinted by permission from Macmillan Publishers Ltd: NATURE [GP], copyright 2009).

The concept of chirality (greek $\chi\varepsilon\iota\rho$ for hand) was first introduced into science by Lord Kelvin [Kel] in the early nineteenth century:

> *I call any geometrical figure, or group of points, chiral, and say that it has chirality, if its image in a plane mirror, ideally realised, cannot be brought to coincide with itself.*

Regarding ones left and right hand this idea makes immediately sense. Obvious the human hands cannot be superimposed by rotation or translation with each other, while this is possible with the respective opposing mirror image (presented in Fig.1.1). An object which is superposable with its mirror image is called achiral. As long as exclusive static, enantiomer objects (under space inversion P or mirror reflections) are considered the definition given by Lord Kelvin is sufficient.
Considering moveable systems, time-reversal arguments cannot be neglected any more. Hence a mathematical stricter definition of chirality has been given by Barron [Barb]:

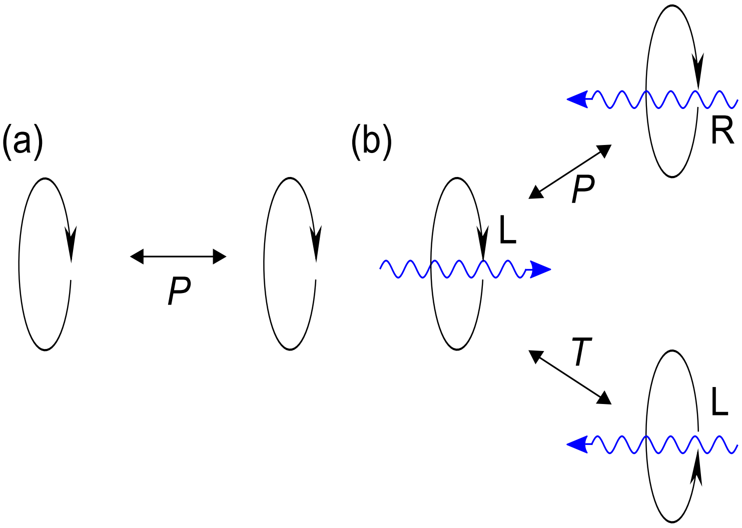

Figure 1.2: P and T effect on a stationary spinning particle (a) and a translating spinning particle (b) (figure taken from [Bara]).

> *True chirality is exhibited by systems existing in two distinct enantiomeric states that are interconverted by space inversion, but not by time reversal combined with any proper spatial rotation.*

For distinction: time non-invariant spatial enantiomorphism are called *false chirality* by Barron. Thus true chiral systems are time invariant. As pointed out in

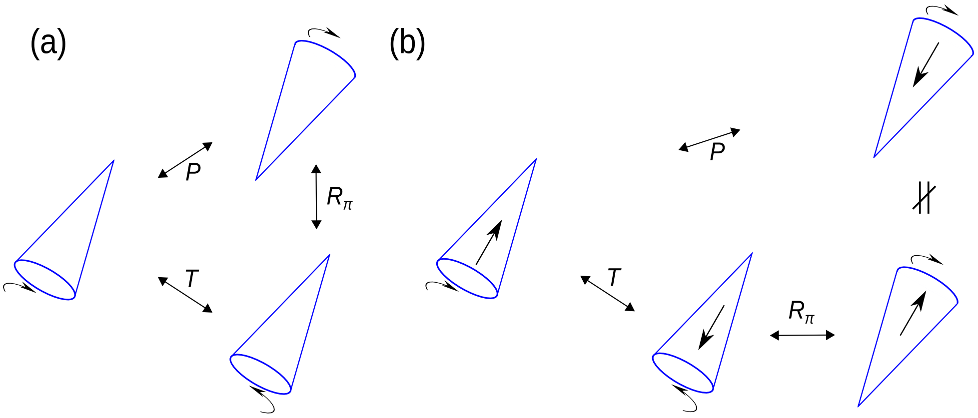

Figure 1.3: The effect of P, T and R_π on (a) a stationary spinning cone, that has false chirality and on (b) a translating spinning cone, that has true chirality (Reprinted with permission from [Barb]. Copyright 1986 American Chemical Society.).

Fig.1.2 (a) a stationer spinning electron is non-chiral (due to the missing enantimor under P inversion), whereas an electron translating with a spin projection parallel/ antiparallel to the direction of motion is truly chiral (see Fig.1.2 (b)). Fig.1.3 illustrates an example for false (a) and true (b) chirality. The spinning cone illustrated in Fig.1.3 (a) is a false chiral object because time reversal T followed by a rotation R_π produces the same object as space inversion P. Fig.1.3 (b) presents the same spinning cone with an additional translating as it is a true chiral object.

1.2 Chiral magnetism

One more fascinating example for chirality is the helical spin arrangement in noncentrosymmetric crystals. To minimise the free energy and enable a chiral arrangement of the magnetic moments a further interaction is necessary, which could be in form of the Dzyaloshinski-Moriya (DM) interaction that will be discussed in more detail in the next section. Another possible source leading to a chiral magnetic order is frustration, which will not be discussed here. To describe the helimagnetic spin structure [as illustrated in Fig.1.4] in cubic B20 compounds without inversion symmetry, two models had been developed based on the phenomenological Landau-like theory. In 1.2.2 the Bak-Jensen model [BJ] will be introduced and a similar model by Nakanishi, Yanase, Hasegawe and Kataoka [NYHK] will be presented in 1.2.3. While both groups used a similar approach, Kataoka and coworkers took the cubic anisotropy into account, which is an important extension of the Bak-Jensen model respective small wavevector $|\boldsymbol{k}_s|$, as it will be revealed in chapter 4.

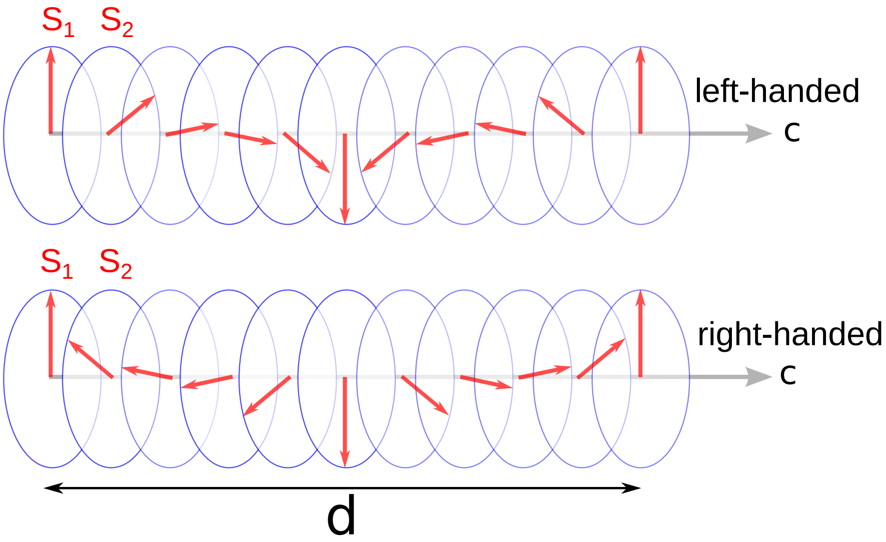

Figure 1.4: Left- and right-handed magnetic spiral.

1.2.1 Dzyaloshinskii-Moriya interaction

Magnetic long range order is usual driven by Heisenberg [Hei] or superexchange interaction [And], which is described by the Hamiltonian

$$H = J\boldsymbol{S}_i \cdot \boldsymbol{S}_j. \tag{1.1}$$

Depending on the sign of the exchange constant J, this term describes a parallel or antiparallel alignment of the magnetic spins. To describe a spiral spin arrangement as it is exemplified in Fig.1.4 an additional term is necessary.
In the middle of the last century the weak ferromagnetic behaviour observed in otherwise antiferromagnetic compounds e.g. α-Fe$_2$O$_3$ was of great interest. The experimentally determined ordered magnetic moment in this compounds was 10^{-2} - 10^{-5} times smaller than the expected ferromagnetic coupling. In 1958 Dzyaloshinskii [Dzyb] gave a phenomenological answer to the question if the weak ferromagnetism is an intrinsic property of α-Fe$_2$O$_3$. He could reveal that an α-Fe$_2$O$_3$ crystal with spins perpendicular to the trigonal axis (antiferromagnetic arrangement) has the same symmetry as with a canted spin arrangement and a net magnetisation perpendicular to the trigonal axis. Writing down the free energy in terms of the spin variables, resulted into an expression that favours the canted spin arrangement

over the antiferromagnetic one:

$$H = \boldsymbol{D}\boldsymbol{S}_i \times \boldsymbol{S}_j, \tag{1.2}$$

with a constant vector $\boldsymbol{D}$. The nature of $\boldsymbol{D}$ was neither clearly defined nor given an expression how to calculate it.

By taking the spin orbit coupling into account Moriya [Mor] was able to extend the theory of Anderson for the anisotropic superexchange [And] in 1960. He provided evidence that Eq.1.2 which was phenomenological introduced by Dzyaloshinskii [Dzyb], appears as relativistic correction of the superexchange interaction due spin-orbit coupling. Moreover, Moriya pointed out the importance of the crystal symmetry. Regarding two ions located at the points A and B, and the straight line AB denoted as C, he formulated the following rules:

1. When a centre of inversion is located at C,
   $\boldsymbol{D} = 0$.
2. When a mirror plane perpendicular to AB passes through C,
   $\boldsymbol{D} \parallel$ mirror plane or $\boldsymbol{D} \perp AB$.
3. When there is a mirror plane including A and B,
   $\boldsymbol{D} \perp$ mirror plane.
4. When a two-fold rotation axis perpendicular to AB passes through C,
   $\boldsymbol{D} \perp$ two-fold axis.
5. When there is an n-fold axis ($n \geq 2$) along AB,
   $\boldsymbol{D} \parallel AB$.

1.2.2 The Bak-Jensen model

In 1958 the idea of a magnetic superstructure with the periodicity many time bigger than the interatomic spacing was proposed simultaneously by Villain [Vil], Kaplan [Kap] and Yoshimory [Yos], based on the symmetric part of the exchange interaction. Six years later, Dzyaloshinskii [Dzya] suggested a mechanism for such a superstructure by an instability of a ferromagnetic structure with respect to small relativistic spin-lattice or spin-spin interactions. The first realisation of such a helical structure was experimentally found by Lundgren and co-workers in the week itinerant ferromagnet FeGe [LBA^{+}] and in 1976 by Ishikawa and co-workers [ITBR] in MnSi. In 1980 Bak and Jensen [BJ] were able to explain the long-period helimagnetic structure in these compounds by including the Dzyaloshinskii-Moriya interaction into the free energy. They expanded the free energy in terms of a slow-varying spin density $\boldsymbol{S(r)}$ according to the theory of Landau and Lifshitz [LL]

$$
\begin{aligned}
F(\boldsymbol{r}) = &\frac{1}{2}A\left(S_x^2+S_y^2+S_z^2\right)+D\boldsymbol{S}\left(\nabla\times\boldsymbol{S}\right)\\
&+\frac{1}{2}B_1\left[(\nabla S_x)^2+(\nabla S_y)^2+(\nabla S_z)^2\right]\\
&+\frac{1}{2}B_2\left[\left(\frac{\partial S_x}{\partial x}\right)^2+\left(\frac{\partial S_y}{\partial y}\right)^2+\left(\frac{\partial S_z}{\partial z}\right)^2\right]\\
&+C_1\left(S_x^2+S_y^2+S_z^2\right)^2\\
&+C_2\left(S_x^4+S_y^4+S_z^4\right). \qquad (1.3)
\end{aligned}
$$

A is here the ferromagnetic exchange energy, D is the DM constant, $B_{1,2}$ are the coefficients for the first and second order anisotropy and $C_{1,2}$ are the fourth-order coefficients. Below T_c the free energy is minimised by periodic structures of the form:

$$
\boldsymbol{S}(\boldsymbol{r})=\frac{1}{\sqrt{2}}\left[\boldsymbol{S}\exp(i\boldsymbol{k}\cdot\boldsymbol{r})+\boldsymbol{S}^*\exp(i\boldsymbol{k}\cdot\boldsymbol{r})\right]. \qquad (1.4)
$$

Insert Eq.1.4 into 1.3 the free energy density becomes (to second order in $\boldsymbol{S}$):

$$
\begin{aligned}
F(\boldsymbol{k}) = &\frac{1}{2}A|\boldsymbol{S}|^2+iD\boldsymbol{k}\left(\boldsymbol{S}\times\boldsymbol{S}^*\right)+\frac{1}{2}B_1k^2|\boldsymbol{S}|^2\\
&+\frac{1}{2}B_2\left(k_x^2|S_x|^2+k_y^2|S_y|^2+k_z^2|S_z|^2\right). \qquad (1.5)
\end{aligned}
$$

Set $\boldsymbol{S}=\boldsymbol{S_1}+i\boldsymbol{S_2}$, Eq.1.5 is minimised when $\boldsymbol{S_1}\perp\boldsymbol{S_2}$, $|\boldsymbol{S_1}|=|\boldsymbol{S_2}|$ and $\boldsymbol{k}$ antiparallel to $[\boldsymbol{S_1}\times\boldsymbol{S_2}]$ for $D>0$ or $\boldsymbol{k}$ parallel to $[\boldsymbol{S_1}\times\boldsymbol{S_2}]$ for $D<0$, describing a right- and left-handed spiral, respectively. The term D has fully rotational symmetry, so no preferred direction is given for $\boldsymbol{k}$, while the anisotropic second order gradient term with coefficient B_2 could fix the direction of $\boldsymbol{k}$ along the easy axis:

$$
\begin{aligned}
&B_2<0:\boldsymbol{k}\parallel(111)\\
&B_2>0:\boldsymbol{k}\parallel(001). \qquad (1.6)
\end{aligned}
$$

Based on first experimental results obtained by magnetisation and neutron diffraction measurements for MnSi [ITBR] and FeGe [LBA+] it was concluded that $B_2<0$ for both alloys. Based on further small angle neutron scattering measurements Lebech and co-workers revealed a more complex behaviour of the propagation vector in FeGe compounds [LBF]. The direction of the $\boldsymbol{k}$ points along the equivalent $\langle 100\rangle$ directions between the upper ordering temperature $T_c=278.8$ K (where the paramagnetic phase transforms into the helimagnetic structure) and T_2 (the second critical temperature at which the propagation vector changes its direction), with decreasing temperature $T_{2\downarrow} = 211$ K and increasing temperature $T_{2\uparrow} = 245$ K. Below the second critical temperature the propagation direction of $\boldsymbol{k}$ is along the equivalent $\langle 111 \rangle$ directions. The relative small value of the anisotropic second order term enables already a weak applied magnetic field to rotate $\boldsymbol{k}$ into any direction [IKB, GS]. The free energy is finally given by:

$$F = \left(\frac{1}{2}A - |D|k\right)|\boldsymbol{S}|^2 + \left(\frac{1}{2}B_1 + \frac{1}{6}B_2 k^2 |\boldsymbol{S}|^2\right) \tag{1.7}$$

and is minimised by:

$$k = |D| / \left(B_1 + \frac{1}{3}B_2\right). \tag{1.8}$$

The small value of D compared to $B_1 + \frac{1}{3}B_2$ results in a small magnitude of k. In Fig.1.5 the free energy given in Eq.1.7 is plotted versus k for the left-handed ($D < 0$) and the right-handed ($D > 0$) spiral structures. It could be clearly seen that, the ferromagnetic spin structure (illustrated as dashed line) is non-stable ($k = 0$). The Bak-Jensen model does not impose any limitations for the value of k that can become infinite small. As it will be evidenced in chapter 4 the cubic anisotropy has to be taken into account to make the model working in these cases.

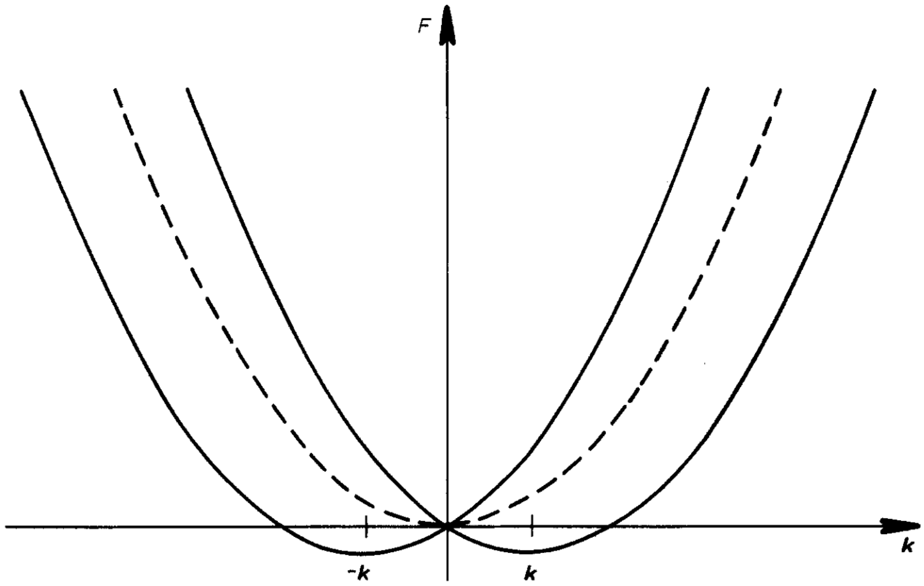

Figure 1.5: Free energy as function of wavevector k for left- and right handed spirals. The dashed line represents the free energy for a system with inversion symmetry (D = 0) (figure taken from [BJ]).

1.2.3 The Nakanishi-Yanase-Hasegawa-Kataoka model

In the same year as Bak and Jensen, the group of Kataoka independently published their work on *the origin of the helical spin density wave in MnSi* [NYHK]. They considered the spin structures of an itinerant electron magnet without inversion symmetry with an exchange energy favourable for a *ferromagnetic state* (FMS). Starting from a spin structure defined in terms of a single $\boldsymbol{k}$, a spatial variation of the spin density $\boldsymbol{S}(\boldsymbol{r})$ is expressed by:

$$\begin{aligned}\boldsymbol{S}\left(\boldsymbol{r}\right) =&\boldsymbol{S}_1\cos\left(\boldsymbol{k}\cdot\boldsymbol{r}\right)+\boldsymbol{S}_2\sin\left(\boldsymbol{k}\cdot\boldsymbol{r}\right)\\ =&\frac{1}{2}\left[\boldsymbol{S}\left(\boldsymbol{r}\right)\exp\left(-i\boldsymbol{k}\cdot\boldsymbol{r}\right)+\boldsymbol{S}\left(\boldsymbol{r}\right)^{*}\exp\left(i\boldsymbol{k}\cdot\boldsymbol{r}\right)\right]\end{aligned}\tag{1.9}$$

For $\boldsymbol{S}_1\perp\boldsymbol{S}_2$ and $S_1=S_2$, $\boldsymbol{S}\left(\boldsymbol{r}\right)$ expresses a *helical spin density wave* (HSDW) and a *sinusoidal spin density wave* (SSDW) for $\boldsymbol{S}_1\ ||\ \boldsymbol{S}_2$. Expanding the free energy F in powers of $\boldsymbol{S}\left(\boldsymbol{r}\right)$ and taking the the space group $P2_13\left(T^4\right)$ into account, the following expression was obtained:

$$\begin{aligned}F=&\left\{\tfrac{1}{2}\left[\chi\left(0\right)^{-1}+ck^2\right]\left\langle S^2\right\rangle_p+\tfrac{1}{4}\gamma\left\langle S^4\right\rangle_p\right\}\\ &+D\left[\boldsymbol{S}_1\times\boldsymbol{S}_2\right]\cdot\boldsymbol{k}+\tfrac{1}{2}\left\{A_1\left[\left\langle 3S_z^2-S^2\right\rangle_p\left(3k_z^2-k^2\right)\right.\right.\\ &\left.+3\left\langle S_x^2-S_y^2\right\rangle_p\left(k_x^2-k_y^2\right)\right]+A_2\left[\left\langle 3S_z^2-S^2\right\rangle_p\right.\\ &\left.\times\left(k_x^2-k_y^2\right)-\left\langle S_x^2-S_y^2\right\rangle_p\left(3k_z^2-k^2\right)\right]\\ &+4A_3\left[\left\langle S_xS_y\right\rangle_p k_xk_y+\left\langle S_yS_z\right\rangle_p k_yk_z\right.\\ &\left.\left.+\left\langle S_zS_x\right\rangle_p k_zk_x\right]\right\}-\tfrac{1}{2}K_1\left[\left\langle S_x^4\right\rangle_p+\left\langle S_y^4\right\rangle_p+\left\langle S_z^4\right\rangle_p\right].\end{aligned}\tag{1.10}$$

With positive c and γ the first two terms stabilise a FMS below the ordering temperature T_c. The second term in Eq.1.10 is responsible for the helical plane in the HSDW perpendicular to the direction of $\boldsymbol{k}$. A distinction is made between a negative and a positive sign of D. A negative sign of D produces a clockwise rotation of the spins ($[\boldsymbol{S_1}\times\boldsymbol{S_2}]$ parallel to $\boldsymbol{k}$), whereas a counterclockwise rotation ($[\boldsymbol{S_1}\times\boldsymbol{S_2}]$ antiparallel to $\boldsymbol{k}$) is energetically favourable for a positive sign of D. The anisotropic energy given in the third term depends on both, the direction of the spins and k. The fourth term represents the magnetic anisotropy energy independent of k. Following Kataoka and co-workers, all terms beside the first one should vanish if the spin-lattice interaction is absence. The spin-orbit interaction is involved into the Dzyaloshinskii-Moriya interaction (second term). Unless the direction of the propagation vector k is along $\langle 111\rangle$ or $\langle 100\rangle$, the third term of Eq.1.10 disturbers the perpendicular configuration. From Eq.1.10 Kataoka and co-workers obtained the three following expressions:

$$\begin{aligned} F_{HSDW} = &\tfrac{1}{2}\left[\chi(0)^{1} - 2|D|k + \left(c + A_1 - A_3\right)k^2\right]S^2 \\ &+ \tfrac{1}{4}\left(\gamma - \tfrac{3}{4}K_1\right)S^4 + \tfrac{1}{2}\left[\left(A_3 - 3A_1\right)S^2k^2 - \tfrac{3}{8}K_1S^4\right] \\ &\times\left(\beta_1^4 + \beta_2^4 + \beta_3^4\right) \end{aligned} \tag{1.11}$$

with $S \equiv S_1 = S_2$; β_1, β_2 and β_3 are the direction cosines of k.

$$F_{SSDW} = \tfrac{1}{2}\left[\chi(0)^{1} + ck^2\right]S^2 + \tfrac{3}{8}\gamma S^4 + (\text{anisotropy energy}) \tag{1.12}$$

$S = \left[\left(S_1^2 = S_2^2\right)/2\right]^{1/2}$ and the anisotropy energy came from the third term in Eq.1.10. The DM interaction does not contribute to the SSDW. For the free energy of the ferromagnetic state they obtained ($k = 0$ and $\boldsymbol{S(r)} = \boldsymbol{S}$):

$$F_{FMS} = \tfrac{1}{2}\chi(0)^{-1}S^2 + \tfrac{1}{4}\gamma S^4 + \tfrac{1}{2}K_1S^4\left(\alpha_1^4 + \alpha_2^4 + \alpha_3^4\right) \tag{1.13}$$

α_1, α_2 and α_3 are the direction cosines of $\boldsymbol{S}$. Minimising the free energies given in Eqs.1.11-1.13, Kataoka and co-workers obtained the following expressions with respect to S below the ordering temperature (small terms are neglected):

$$\begin{aligned} F_{HSDW} &= -\tfrac{1}{4\gamma\chi(0)^2}\left\{\left[1 + \left(\tfrac{3K_1}{4\gamma}\right) - 4|D|\chi(0)k + 2\left(c + A_1 - A_3\right)\chi(0)k^2\right]\right. \\ &\quad \left. + \left[\left(\tfrac{3K_1}{4\gamma}\right) + 2\left(A_3 - 3A_1\right)\chi(0)k^2\right]\left(\beta_1^4 + \beta_2^4 + \beta_3^4\right)\right\} && (1.14) \\ F_{SSDW} &= -\tfrac{1}{6\gamma\chi(0)^2}\left[1 + 2c\chi(0)k^2\right] + (\text{anisotropy energy}) && (1.15) \\ F_{FMS} &= -\tfrac{1}{4\gamma\chi(0)^2}\left[1 + \left(\tfrac{2K_1}{\gamma}\right)\left(\alpha_1^4 + \alpha_2^4 + \alpha_3^4\right)\right]. && (1.16) \end{aligned}$$

Based on the free energy some characteristics for the spin structure in MnSi could be given:

- only if $k \to 0$ the F_{HSDW} is higher than F_{FMS} by a part of the magnetic anisotropy (see Fig.1.6)
- caused by the missing inversion symmetry: $D\left[\boldsymbol{S}_1 \times \boldsymbol{S}_2\right] \cdot \boldsymbol{k}$ causes a decrease of F_{HSDW} with increasing k and has its minimum at k_0 (see Fig.1.6)
- the SSDW spin structure might be just considerable in a domain structure
- HSDW is the most stable structure for a small magnetic anisotropy energy K_1, for an increasing anisotropic energy the HWSD becomes unstable
- as the magnitude of spin decreases, the fourth term decreases faster than the second term in Eq.1.10 → with increasing temperature HSDW is getting more stable than FMS

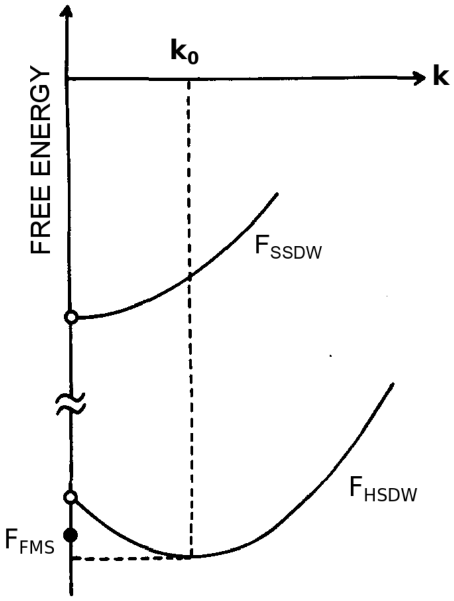

Figure 1.6: Free energies F_{HSDW}, F_{SSDW} and F_{FMS} given by Eq.1.14 - 1.16.The solid circle represents F_{FMS}. HSDW and SSDW have no meaning at $k = 0$. The minimum of F_{HSDW} is at $k_0\,(\approx |D|/c)$ for small K_1 (Reprinted from [NYHK], Copyright (1980), with permission from Elsevier).

The magnitude of k for the minimum of F_{HSDW} is given by:

$$k_0 = \frac{|D|}{c}\left[1 + \left(\frac{A_3 - A_1}{c}\right) + \left(\frac{3A_1 - A_3}{c}\right)\left(\beta_1^4 + \beta_2^4 + \beta_3^4\right)\right] \tag{1.17}$$

Due the small value of the second and third term in Eq.1.17 k_0 is approximated by $k_0 \approx |D|/c$, which leads to a small dependence of k_0 on the direction $\boldsymbol{k}$. When substituting Eq.1.17 into Eq.1.14 one obtains the anisotropy energy of the direction of $\boldsymbol{k}$ (neglecting small terms) as:

$$-\frac{3K_1}{[4\gamma\chi(0)]^2}\left(\beta_1^4 + \beta_2^4 + \beta_3^4\right) \tag{1.18}$$

For a negative or positive value of K_1, $\boldsymbol{k}$ is directed into the $\langle 111\rangle$ and $\langle 100\rangle$ direction, respectively. Without anisotropic energies the free energy is isotropic with respect to the direction of $\boldsymbol{k}$.

In contrast to Bak and Jensen, Kataoka and co-workers take the cubic anisotropy into account, limiting the stability of the helical spin structure in case of small k_s. However, they do not consider the influence of the cubic anisotropy of the second critical field H_{c2} at which the spiral is transformed into the field aligned ferromagnetic spin structure.

Chapter 2

Scattering Theory

In this chapter a brief overview of the scattering theory used in this thesis will be given. Since the 1960s neutron scattering is established as a unique technique to provide information on the atomic level of condensed matter systems. The main advantages are [Squ]:

- The de-Broglie wavelength of thermal neutrons is in the order of interatomic distances in solids and liquids (a few Å). From the interference effects occurring during the scattering process it is possible to gain information about the atomic structure of the investigated system.
- Because neutrons are uncharged, there is no Coulomb barrier to overcome. Thus neutrons are scattered by the nuclear forces, which allow to penetrate deeply and provides information about bulk material. Contrary to X-ray scattering the scattering length is no monotonic function of the atomic number. It varies strongly for neighbouring elements and even for different isotopes of the same element. For example, the light element hydrogen is virtually transparent to X-ray, but a strong scatterer for neutrons.
- Neutrons are spin one-half particles: they carry a magnetic moment. This leads to an interaction with the unpaired electrons in a solid. From the elastic scattering it is possible to gain information about the electron spin arrangement and density distribution of the unpaired electrons.
- The energy of many excitations in condensed matter is of the same order as that of thermal neutrons. Therefore, the measurements of the energy gain or loose of the neutrons during inelastic scattering by creation or annihilation of an excitation provides information about the energy of these excitations.

This chapter is based on the books of Lovesey [Lov] and Squires [Squ], where also most of the formulas are taken from. The de-Broglie wavelength of neutrons with a velocity v is given by

$$\lambda = \frac{h}{mv} = \frac{h}{p}. \tag{2.1}$$

Within a typical scattering process neutrons with an initial momentum $\hbar\boldsymbol{k}_i$ are scattered due the interaction with a sample into another state with the momentum $\hbar\boldsymbol{k}_f$. Due the conservation laws the momentum and energy are conserved in this process and the relevant momentum and energy transfers are given by

$$\begin{aligned} \hbar\boldsymbol{Q} &= \hbar\left(\boldsymbol{k}_i - \boldsymbol{k}_f\right) \\ \hbar\omega &= E_i - E_f = \frac{\hbar}{2m_n}\left(|\boldsymbol{k}_i|^2 - |\boldsymbol{k}_f|^2\right). \end{aligned} \tag{2.2}$$

The scattering function $S\left(\boldsymbol{Q},\omega\right)$ gives the probability of the scattering of a neutron with the incoming wavevector $\boldsymbol{k}_i$ into a certain direction with the outgoing wavevector $\boldsymbol{k}_f$. A Fourier transformation of $S\left(\boldsymbol{Q},\omega\right)$ grants the scattering potential in real space and time. The probability of the scattering is given by the partial differential neutron scattering cross section (exemplified in Fig.2.1)

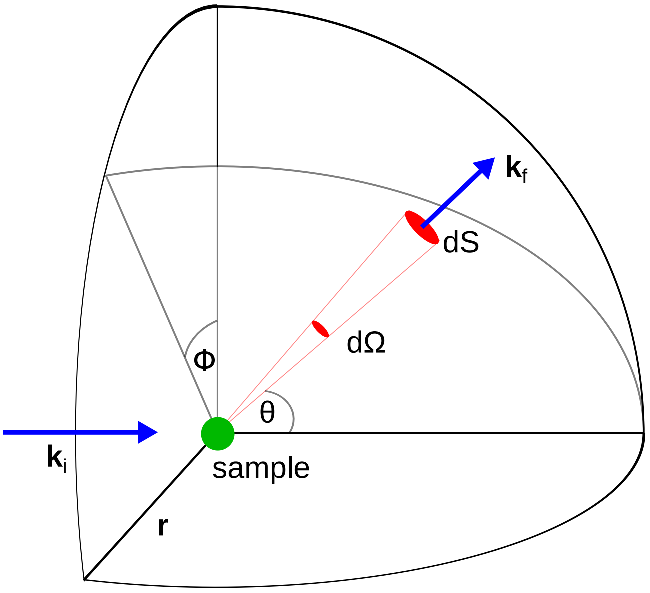

Figure 2.1: Geometry for a scattering experiment (adapted from [Squ]).

$$\frac{d^2\sigma}{d\Omega dE_f} = \frac{\text{neutrons scattered into the solid angle } d\Omega \text{ and energy interval } dE_f}{\text{Incident flux of neutrons } \Phi \; d\Omega_f \; dE_f}. \tag{2.3}$$

By using Fermi's golden rule, the partial differential neutron scattering cross-section can by given in mathematical terms (see [Squ,Lov] for a detailed derivation) as:

$$\frac{d^2\sigma}{d\Omega dE_f} = \frac{k_f}{k_i} \sum_{\lambda_i,\sigma_i} p_\lambda p_\sigma \sum_{\lambda_f,\sigma_f} |\left\langle \boldsymbol{k}_f, \sigma_f, \lambda_f | V | \boldsymbol{k}_i, \sigma_i, \lambda_i \right\rangle|^2 \delta\left(\hbar\omega + E_{\lambda_i} - E_{\lambda_f}\right), \quad (2.4)$$

where σ_i/σ_f represent the ratio of incoming to outgoing spin states of the neutrons. The (normalised) weights p_λ of the initial state is given as product of the thermodynamics factors $\exp\left(-E_\lambda/k_B T\right)$ at the sample temperature T. For an unpolarised beam the probability for the neutron spin to be in the up or down state is equally $\mathrm{p}_\sigma = \frac{1}{2}$. Eq.2.4 takes all possible initial and final state into account. The matrix element $\langle ... \rangle$ represents the transition probability from the initial state to the final state of the system due the interaction operator V. The δ-function ensure the energy conservation.

2.1 Nuclear scattering

2.1.1 The Fermi pseudopotential

The interaction of the neutron with matter takes place via the nuclear force. The range of these interactions is small (approx. 1 fm) compared to the wavelength of the neutron (approx. 0.1 - 2 nm, for thermal and cold neutrons). The scattering potential of a single spinless nucleus j at the position $\boldsymbol{R}_j$, with the scattering length b_j, is given by the *Fermi pseudopotential* [Lov, Squ]:

$$V_j\left(\boldsymbol{r}\right) = \frac{2\pi\hbar^2}{m} b_j \delta\left(\boldsymbol{r} - \boldsymbol{R}_j\right). \quad (2.5)$$

With the mass of the neutron m_n. By summing up over all individual nuclei j one obtains the scattering potential of the ensemble of the nuclei

$$V\left(\boldsymbol{r}\right) = \frac{2\pi\hbar^2}{m} \sum_j b_j \delta\left(\boldsymbol{r} - \boldsymbol{R}_j\right). \quad (2.6)$$

Due to the weak interactions the Born approximation can be considered as valid. In consequence, both the incoming and outgoing wave is considered as plane wave. The accuracy of the Born approximation, for s-wave scattering, has been proven by Nowak in 1982 [Now]. The matrix element is given as:

$$\left|\left\langle k_f, \lambda_f \left| V \right| k_i, \lambda_i \right\rangle\right|^2 = \left(\frac{2\pi\hbar^2}{m_n}\right)^2 \left| \sum_j b_j \left\langle \lambda_f \right| \exp\left(i\boldsymbol{Q}\cdot\boldsymbol{R}_j\right) \left|\lambda_i\right\rangle \right|^2. \quad (2.7)$$

With the scattering vector $\boldsymbol{Q}$. Using the time dependent Heisenberg operator $\boldsymbol{R}_j$

$$\boldsymbol{R}_j\,(t) = \exp(iHt/\hbar)\boldsymbol{R}_j \exp(-iHt/\hbar) \tag{2.8}$$

and the integral form of the δ-function

$$\delta(E_{\lambda_i} - E_{\lambda_f} + E - E') = \frac{1}{2\pi\hbar}\int_{-\infty}^{+\infty} \exp\left\{i\left(E_{\lambda_f} - E_{\lambda_i}\right)/\hbar\right\}\exp(-i\omega t)dt, \tag{2.9}$$

where ω is defined via $\hbar\omega = E - E'$. The final expression for the nuclear partial differential neutron scattering cross-section can be written as [Squ]:

$$\frac{d^2\sigma}{d\Omega dE_f} = \frac{k_f}{k_i}\frac{1}{2\pi\hbar}\sum_{j,j'} b_j b_{j'} \int_{-\infty}^{+\infty} \langle\exp\{-i\boldsymbol{Q}\cdot\boldsymbol{R}_{j'}(0)\}\exp\{i\boldsymbol{Q}\cdot\boldsymbol{R}_j(t)\}\rangle\exp(-i\omega t)dt. \tag{2.10}$$

Where $\langle A\rangle = \sum\limits_{\lambda} = p_\lambda \langle\lambda|A|\lambda\rangle$ is the thermal average over the operator A.

2.1.2 Coherent and incoherent scattering

The differential cross section is a sum of the *coherent* and *incoherent* scattering parts. The coherent part offers information about the correlations between the same nucleus at different times, and different nuclei at different times. For this reason, interference effects could appear. From the coherent part of the cross section one can gain information about the structure or excitations in condensed matter systems. The incoherent scattering depends only on the correlation between the position of the same nucleus at different times, therefore no interference effects take place. In a sample with unknown distribution of nuclei and isotopes it is necessary to average over all possible scattering lengths b_j [Squ]

$$\frac{d^2\sigma}{d\Omega dE_f} = \frac{k_f}{k_i}\frac{1}{2\pi\hbar}\sum_{j,j'} \overline{b_{j'} b_j} \int \langle\exp\{-i\boldsymbol{Q}\cdot\boldsymbol{R}_{j'}(0)\}\exp\{i\boldsymbol{Q}\cdot\boldsymbol{R}_j(t)\}\rangle\exp(-i\omega t)dt, \tag{2.11}$$

where $\overline{b_{j'} b_j}$ can be separated into the coherent and incoherent part

$$\left(\frac{d^2\sigma}{d\Omega dE_f}\right)_{coh} = \frac{\sigma_{coh}}{4\pi}\frac{k_f}{k_i}\frac{1}{2\pi\hbar}\sum_{j,j'}\int_{-\infty}^{+\infty} \langle\exp\{-i\boldsymbol{Q}\cdot\boldsymbol{R}_{j'}(0)\}\exp\{i\boldsymbol{Q}\cdot\boldsymbol{R}_j(t)\}\rangle\exp(-i\omega t)dt. \tag{2.12}$$

and

$$\left(\frac{d^2\sigma}{d\Omega dE_f}\right)_{inc} = \frac{\sigma_{inc}}{4\pi}\frac{k_f}{k_i}\frac{1}{2\pi\hbar}\sum_{j}\int_{-\infty}^{+\infty} \langle\exp\{-i\boldsymbol{Q}\cdot\boldsymbol{R}_{j}(0)\}\exp\{i\boldsymbol{Q}\cdot\boldsymbol{R}_j(t)\}\rangle\exp(-i\omega t)dt. \tag{2.13}$$

with $\sigma_{coh} = 4\pi \left(\overline{b}\right)^2$ and $\sigma_{inc} = 4\pi \left\{\overline{b^2} - \left(\overline{b}\right)^2\right\}$. The focus of this work is on the contributions from the coherent scattering only, while the isotropic incoherent contribution just add some intensity to the background. The coherent and incoherent cross sections for the elements considered within this dissertation are given in Tab.2.1.

Table 2.1: Neutron scattering cross sections for the elements used in this thesis (for a wavelength of 1.798 Å) [Sea].

Element	Z	σ_{coh} (barn)	σ_{inc} (barn)	σ_{abs} (barn)
Si	14	2.1633(10)	0.004(8)	0.171(3)
Mn	25	1.75(2)	0.40(2)	13.3(2)
Fe	26	11.22(5)	0.40(11)	2.56(3)
Co	27	0.779(13)	4.8(3)	37.18(6)
Ge	32	8.42(4)	0.18(7)	2.20(4)

2.1.3 Nuclear Bragg scattering from a crystal

In this thesis, single or polycrystalline samples are investigated exclusively. For this reason, Eq.2.10 will be evaluated for the case of single crystals. The detailed deviation can be found in [Squ]. For convenience a Bravais crystal (infinite array of discrete points) is considered, with one atom per unit cell. The sides of the unit cell are given by three independent basic vectors $\boldsymbol{a}_1$, $\boldsymbol{a}_2$ and $\boldsymbol{a}_3$. The lattice vector in this case is given by

$$\boldsymbol{l} = l_1\boldsymbol{a}_1 + l_2\boldsymbol{a}_2 + l_3\boldsymbol{a}_3 \tag{2.14}$$

and the corresponding volume

$$v_0 = \boldsymbol{a}_1 \left[\boldsymbol{a}_2 \times \boldsymbol{a}_3\right]. \tag{2.15}$$

The unit cell vectors $\boldsymbol{\tau}_j$ fulfil $\mathbf{a}_i\boldsymbol{\tau}_j = 2\pi\delta_{ij}$ and are defined as

$$\boldsymbol{\tau}_1 = \frac{2\pi}{v_0}\left[\boldsymbol{a}_2 \times \boldsymbol{a}_3\right] \qquad \boldsymbol{\tau}_2 = \frac{2\pi}{v_0}\left[\boldsymbol{a}_3 \times \boldsymbol{a}_1\right] \qquad \boldsymbol{\tau}_3 = \frac{2\pi}{v_0}\left[\boldsymbol{a}_1 \times \boldsymbol{a}_2\right] \tag{2.16}$$

the displacement of the the nucleus l due thermal motion is represented by $\boldsymbol{u}_l$ in the instantaneous position operator $\boldsymbol{R}_l(t) = \boldsymbol{l} + \boldsymbol{u}_l(t)$. In the considered case the correlation between two nuclei depends only on its distance, $\boldsymbol{l} - \boldsymbol{l}'$, and one can set l' = 0 and get

$$\begin{aligned} &\sum_{l,l'} \left\langle \exp\left\{-i\boldsymbol{Q}\cdot\boldsymbol{R}_{l'}(0)\right\} \exp\left\{i\boldsymbol{Q}\cdot\boldsymbol{R}_l(t)\right\}\right\rangle \\ &= N\sum_l \exp\left(i\boldsymbol{Q}\cdot\boldsymbol{l}\right) \left\langle \exp\left\{-i\boldsymbol{Q}\cdot\boldsymbol{u}_0(0)\right\} \exp\left\{i\boldsymbol{Q}\cdot\boldsymbol{u}_l(t)\right\}\right\rangle. \end{aligned} \tag{2.17}$$

N is the number of nuclei in the crystal, $U = -i\boldsymbol{Q} \cdot \boldsymbol{u}_0(0)$ and $V = i\boldsymbol{Q} \cdot \boldsymbol{u}_l(t)$. Assuming harmonic interatomic forces (i.e. linear forces) in the crystal the theory of normal mode can be applied to describe the motions of the atoms inside the crystal (see [Squ] for details). Resulting in $\langle \exp U \exp V \rangle = \exp \langle U^2 \rangle \exp \langle UV \rangle$, where: $\exp\left(2W\left(\boldsymbol{Q}\right)\right) = \exp\left(-\langle U^2 \rangle\right) = \exp\left(\left\langle \left\{\boldsymbol{Q} \cdot \boldsymbol{u}_0(0)\right\}^2 \right\rangle\right)$ is called *Debye-Waller factor* [Deb, Wal]. Expanding this expression gives

$$\exp \langle UV \rangle = 1 + \langle UV \rangle + \frac{1}{2!} \langle UV \rangle^2 + \ldots. \tag{2.18}$$

For the elastic scattering of zeroth order one obtain the cross-section [Squ]

$$\left(\frac{d\sigma}{d\Omega}\right)_{coh,el} = \frac{\sigma_{coh}}{4\pi} N \frac{(2\pi)^3}{v_0} \exp\left(-2W\left(\boldsymbol{Q}\right)\right) \sum_{\tau} \delta\left(\boldsymbol{Q} - \boldsymbol{\tau}\right) \tag{2.19}$$

Eq.2.19 reveals that scattering just appears for $\boldsymbol{Q} = \boldsymbol{k}_i - \boldsymbol{k}_f = \boldsymbol{\tau}$. As pointed out in Fig.2.2, this is equivalent to Braggs law in reciprocal space

$$\tau = 2k \sin\left(\frac{\theta}{2}\right) \tag{2.20}$$

Set $k = k_i = k_f = \frac{2\pi}{\lambda}$ and $\tau = n\frac{2\pi}{d}$ one obtain Bragg's law

$$n\lambda = 2d \sin\left(\frac{\theta}{2}\right) \tag{2.21}$$

where d is the lattice spacing and λ the wavelength of the neutrons. The expression above can be easily extended for non-Bravais lattice [Squ]:

$$\left(\frac{d\sigma}{d\Omega}\right)_{coh,el} = N \frac{(2\pi)^3}{v_0} \sum_{\tau} \delta\left(\boldsymbol{Q} - \boldsymbol{\tau}\right) \left|F_N\left(\boldsymbol{Q}\right)\right|^2 \tag{2.22}$$

due the extension of the cross-section with the so-called *nuclear unit-cell factor*:

$$F_N\left(\boldsymbol{Q}\right) = \sum_{d} \bar{b}_d \exp\left(i\boldsymbol{Q} \cdot \boldsymbol{d}\right) \exp\left(-W_d\right) \tag{2.23}$$

The vector $\boldsymbol{d}$ gives the position and $\exp\left(-W_d\right)$ the *Debye-Waller factor* of the dth atom in the unit cell.

2.2 Magnetic scattering

In the following chapter the interaction of the magnetic dipole moment of the neutron with the magnetic field produced by the unpaired electrons of the samples

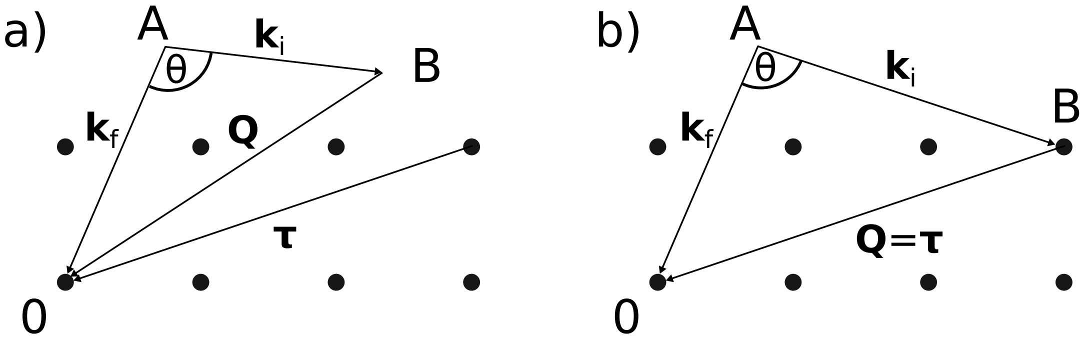

Figure 2.2: Bragg's law in reciprocal space (a) $\boldsymbol{Q} \neq \boldsymbol{\tau}$: no coherent elastic scattering appears, (b) $\boldsymbol{Q} = \boldsymbol{\tau}$: coherent elastic scattering appears (adapted from [Squ]).

will be described. The operator corresponding to the magnetic dipole moment of the neutron is given by

$$\boldsymbol{\mu}_n = -\gamma \mu_N \hat{\boldsymbol{\sigma}} \tag{2.24}$$

with the *nuclear magneton*

$$\mu_N = \frac{e\hbar}{2m_p}. \tag{2.25}$$

m_p is the mass of the proton, e the its charge, $\gamma = 1.913$ the *gyromagnetic ratio* and $\hat{\boldsymbol{\sigma}}$ the *Pauli-matrices*[1] . The unpaired electrons of the sample produce a magnetic field via the spin (magnetic dipole moment of the electron $\boldsymbol{\mu_e} = -2\mu_B \boldsymbol{s}$) of

$$\boldsymbol{B}_S = \frac{\mu_0}{4\pi} \nabla \times \frac{\boldsymbol{\mu}_e \times \hat{\boldsymbol{R}}}{R^2} \tag{2.27}$$

$\hat{\boldsymbol{R}}$ is the unit vector in the direction of $\boldsymbol{R}$, that is the distance from the electron, μ_B the *Bohr magneton*, m_e the mass of the electron and the index S marks the spin origin of the field. The second possibility is obtained from the Biot and Savard law (electronic current related to the orbital motion)

$$\boldsymbol{B}_L = -\frac{\mu_0}{4\pi} \frac{2\mu_B}{\hbar} \frac{\boldsymbol{p} \times \hat{\boldsymbol{R}}}{R^2} \tag{2.28}$$

---

[1]

$$\hat{\sigma}_1 = |\uparrow\rangle\langle\downarrow| + |\downarrow\rangle\langle\uparrow| \qquad \hat{\sigma}_2 = -i\,|\uparrow\rangle\langle\downarrow| + i\,|\downarrow\rangle\langle\uparrow| \qquad \hat{\sigma}_3 = |\uparrow\rangle\langle\uparrow| - |\downarrow\rangle\langle\downarrow| \tag{2.26}$$

with the *electron momentum* $\boldsymbol{p}$ at the point $\boldsymbol{R}$, where L marks the orbital origin of the field. Altogether the magnetic interaction potential of a neutron with the dipole momentum $\boldsymbol{\mu}_n$ in the field $\boldsymbol{B}$ is given by

$$V_m = -\boldsymbol{\mu}_n \cdot \boldsymbol{B} = -\frac{\mu_0}{4\pi}\gamma\mu_N 2\mu_B \hat{\boldsymbol{\sigma}} \cdot (\boldsymbol{W}_S + \boldsymbol{W}_L) \tag{2.29}$$

where $\boldsymbol{W}_S = \nabla \times \left(\frac{\boldsymbol{s}\times\hat{\boldsymbol{R}}}{R^2}\right)$ and $\boldsymbol{W}_L = \frac{1}{\hbar}\frac{\boldsymbol{p}\times\hat{\boldsymbol{R}}}{R^2}$. The evaluation of the matrix element $\langle \boldsymbol{k}_f | V_m | \boldsymbol{k}_i \rangle$ is carried out in detail in [Squ] and is just briefly outlined here. For the ith electron with spin $\boldsymbol{s}_i$, the position $\boldsymbol{r}_i$ and the momentum $\boldsymbol{p}_i$

$$\sum_i \langle \boldsymbol{k}_f | \boldsymbol{W}_{S_i} + \boldsymbol{W}_{L_i} | \boldsymbol{k}_i \rangle = 4\pi \boldsymbol{M}_{\boldsymbol{Q}\perp} \tag{2.30}$$

$$\boldsymbol{M}_{\boldsymbol{Q}_\perp} = \sum_i \exp\left(i\boldsymbol{Q}\cdot\boldsymbol{r}_i\right)\left\{\hat{\boldsymbol{Q}} \times \left(\boldsymbol{s}_i \times \hat{\boldsymbol{Q}}\right) + \frac{i}{\hbar Q}\left(\boldsymbol{p}_i \times \hat{\boldsymbol{Q}}\right)\right\} \tag{2.31}$$

$\hat{\boldsymbol{Q}}$ is the unit vector in the direction of $\boldsymbol{Q}$ and $\boldsymbol{M}_{\boldsymbol{Q}_\perp}$ is the so-called *magnetic interaction vector*, which could also be expressed as a function of the local magnetisation density $\boldsymbol{M}(\boldsymbol{r})$ at the point $\boldsymbol{r}$

$$\boldsymbol{M}_{\boldsymbol{Q}\perp} = \hat{\boldsymbol{Q}} \times \left(\boldsymbol{M}_{\boldsymbol{Q}} \times \hat{\boldsymbol{Q}}\right) \tag{2.32}$$

$$\boldsymbol{M}_{\boldsymbol{Q}} = -\frac{1}{2\mu_B}\int \boldsymbol{M}(\boldsymbol{r}) \exp\left(i\boldsymbol{Q}\cdot\boldsymbol{r}\right) d\boldsymbol{r}. \tag{2.33}$$

$\boldsymbol{M}_{\boldsymbol{Q}}$ is the *magnetic structure factor* and effectively the Fourier transformation of $\boldsymbol{M}(\boldsymbol{r})$. For this reason, information of the microscopic magnetisation of the sample can be obtained by measure the distribution of the magnetic neutron scattering. The final expression for the complete magnetic cross-section for an unpolarised neutron beam ($p_\sigma = 0.5$ for both polarisation states) is given by (see [Squ] for details)

$$\begin{aligned}\frac{d^2\sigma}{d\Omega dE_f} &= (\gamma r_0)^2 \frac{k_f}{k_i}\sum_{\alpha\beta}\left(\delta_{\alpha\beta} - \hat{Q}_\alpha \hat{Q}_\beta\right) \\ &\times \sum_{\lambda_i\lambda_f} p_\lambda \left\langle \lambda_i | M^*_{\boldsymbol{Q}\alpha} | \lambda_f \right\rangle \langle \lambda_f | M_{\boldsymbol{Q}\beta} | \lambda_i \rangle\, \delta\left(E_{\lambda_i} - E_{\lambda_f} + \hbar\omega\right)\end{aligned} \tag{2.34}$$

where r_0 is the *classical electron radius*, $\alpha, \beta = x, y, z$ and $\delta_{\alpha,\beta}$ the Kronecker delta function. According to Eq.2.32 only the component of the magnetisation which is perpendicular to the scattering vector contributes to the scattering cross section. Fig.2.3 (a) illustrates the decomposition of the magnetisation vector $\boldsymbol{M}_{\boldsymbol{Q}}$. $\boldsymbol{M}_{\boldsymbol{Q}\perp}$is

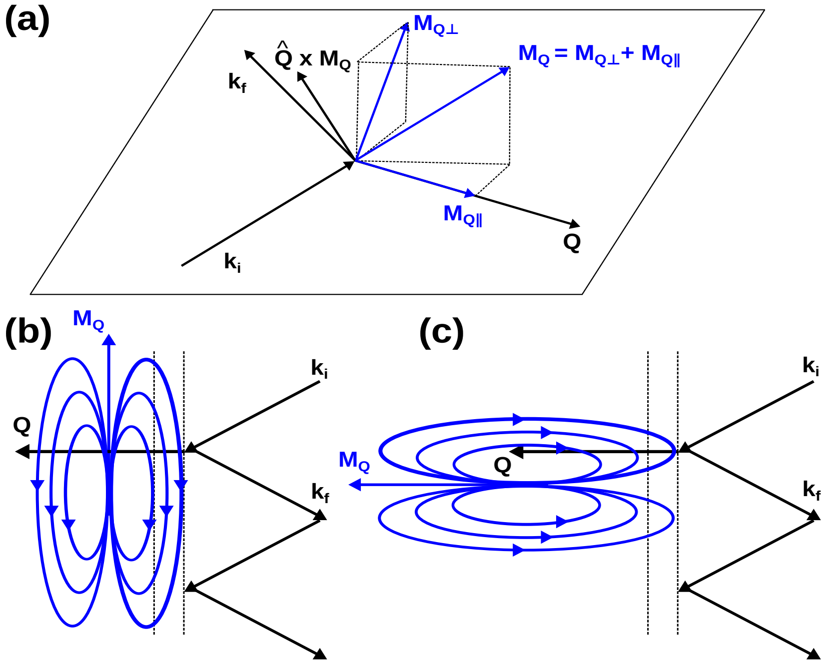

Figure 2.3: Decomposition of the magnetisation vector $\boldsymbol{M_Q}$ (a) and the magnetic field configuration for $\boldsymbol{M_Q}$ perpendicular (b) and parallel (c) to the scattering vector $\boldsymbol{Q}$ (adapted from [Her]).

the projection of the *magnetic structure factor* $\boldsymbol{M_Q}$ onto a plane perpendicular to the scattering vector $\boldsymbol{Q}$. Due the dipole nature of the magnetic interaction, only the component of $\boldsymbol{M_Q}$ perpendicular $\boldsymbol{Q}$ contributes to the scattering process. This could be illustrated with the help of Fig.2.3 (b/c): a magnetisation parallel to the scattering vector will be cancelled out due to destructive interference, thus the net magnetisation becomes zero. In the perpendicular case, on the other hand, constructive interference takes place and the net magnetisation is maximised.

2.2.1 Scattering due spin only

Considering firstly the *Heitler-London* model as valid, i.e. the unpaired electron are localised. Secondly *LS* coupling takes place, i.e. L and S are good quantum numbers. In addition, the considered crystal is a non-Bravis crystal with nucleus l and d at position $\boldsymbol{R}_{ld}$. If $\boldsymbol{r}_\nu$ is the position of the νth unpaired electron in the ion l, d relative to the nucleus, then

$$\boldsymbol{r}_i = \boldsymbol{R}_{ld} + \boldsymbol{r}_\nu \tag{2.35}$$

and for the *magnetic structure factor* [Squ]

$$\begin{aligned}\langle \lambda_f | \boldsymbol{M}_{\boldsymbol{Q}} | \lambda_i \rangle &= \left\langle \lambda_f | \exp\left(i\boldsymbol{Q}\cdot\boldsymbol{R}_{ld}\right) \sum_{\nu(d)} \exp\left(i\boldsymbol{Q}\cdot\boldsymbol{r}_{\nu}\right) \boldsymbol{s}_{\nu} | \lambda_i \right\rangle \\ &= F_d\left(\boldsymbol{Q}\right) \langle \lambda_f | \exp\left(i\boldsymbol{Q}\cdot\boldsymbol{R}_{ld}\right) \boldsymbol{S}_{ld} | \lambda_i \rangle \end{aligned} \tag{2.36}$$

with the *magnetic form factor*

$$F_d\left(\boldsymbol{Q}\right) = \int s_d\left(\boldsymbol{r}\right) \exp\left(i\boldsymbol{Q}\cdot\boldsymbol{r}\right) d\boldsymbol{r} \tag{2.37}$$

The scalar function $s_d\left(\boldsymbol{r}\right)$ is the normalised density of the unpaired electrons in the ion d. $\boldsymbol{S}_{ld}$ is the *total spin* of the considered ion.

2.2.2 Scattering by ions with spin and orbital angular momentum

For ions with both, spin and unquenched orbital angular moment [$L \neq 0$ (e.g. rare earth elements)] the *magnetic form factor* from Eq.2.37 can be replace by [Squ]

$$\frac{1}{2} g F\left(\boldsymbol{Q}\right) = \frac{1}{2} g_s \mathfrak{J}_0 + \frac{1}{2} g_L \left(\mathfrak{J}_0 + \mathfrak{J}_2\right) \tag{2.38}$$

with

$$g_s = 1 + \frac{S\left(S+1\right) - L\left(L+1\right)}{J\left(J+1\right)} \qquad g_L = \frac{1}{2} + \frac{L\left(L+1\right) - S\left(S+1\right)}{2J\left(J+1\right)} \tag{2.39}$$

$$\mathfrak{J}_n = 4\pi \int_0^{\infty} j_n\left(Qr\right) s\left(r\right) r^2 dr. \tag{2.40}$$

$g = g_s + g_L$ is the *Landé splitting factor*, $j_n\left(Qr\right)$ a *spherical Bessel function* of the order n, and $s\left(r\right)$ the normalised density of the unpaired electrons averaged of all direction in space. For partially quenched orbital angular momentum the operator $\boldsymbol{S}$ has to be considered as total angular momentum operator $\boldsymbol{J}$.

2.2.3 Magnetic Bragg scattering of helical order

In the following section the scattering from a magnetic crystal with a helical arrangement of spins (as it will be considered throughout this work) is considered. A detailed deviation of this and further spin arrangements (e.g. anti-, ferromagnetism) can be found in [Squ] for example. To develop the cross-section for a helical spin arrangement, the spins are assumed to be in the xy plane, perpendicular to the z-axis. For the magnetic ion on the side l, the total spin is given by

$$\begin{aligned} \langle S_l^x \rangle &= \langle S \rangle \cos\left(\boldsymbol{k}\cdot\boldsymbol{l}\right) \\ \langle S_l^y \rangle &= \langle S \rangle \sin\left(\boldsymbol{k}\cdot\boldsymbol{l}\right) \\ \langle S_l^z \rangle &= 0 \end{aligned} \tag{2.41}$$

with the *propagation vector* $\boldsymbol{k}$ and $k_s = \frac{2\pi}{d}$. d gives the periodicity of the magnetic structure in real space. The scattering cross-section is given by

$$\left(\frac{d\sigma}{d\Omega}\right)_{mag,el} = \left(\gamma r_0\right)^2 \left\{\frac{1}{2} g F\left(\boldsymbol{Q}\right)\right\}^2 \exp\left(-2W\right) I \tag{2.42}$$

where

$$I = \frac{N}{4}\frac{\left(2\pi\right)^3}{v_0} \langle S \rangle^2 \left(1+\hat{Q}_z^2\right) \sum_{\tau} \left\{\delta\left(\boldsymbol{Q}+\boldsymbol{k}-\boldsymbol{\tau}\right) + \delta\left(\boldsymbol{Q}-\boldsymbol{k}-\boldsymbol{\tau}\right)\right\}. \tag{2.43}$$

The scattering arising from the helical spin structure appears at the scattering positions $\boldsymbol{Q} = \boldsymbol{\tau} \pm \boldsymbol{k}$, relative to the nuclear peaks at $\boldsymbol{\tau}$ as it follows from the δ function in Eq.2.43. For a magnetic structure commensurate with the chemical lattice (e.g. ferromagnets, $k_s = 0$) the magnetic scattering appears at $\boldsymbol{Q} = \boldsymbol{\tau}$.

2.3 Polarised scattering

In the previous sections the spin of the incident and scattered neutron has been assumed as randomly oriented. In many cases it is useful to consider polarised neutrons to gain more detailed information about the scattering process. In this section the polarised beam, the *Blume-Maleev equation* [MBS, Blu] and polarised scattering on chiral magnets will be discussed. Additional a quick overview about experimental polarisation and flipping of neutrons will be given. All through this work use is made of the unique ability of polarised neutrons to distinguish between left- and right handed magnetic chirality.

2.3.1 Polarised beam

A neutron is a spin $\frac{1}{2}$ particle. For the individual neutron j in the beam the vector $\boldsymbol{p}_j$ gives the three expectations values of the three components of the Pauli matrices 2.26

$$\boldsymbol{p}_j = \langle \boldsymbol{\sigma} \rangle = \begin{pmatrix} \langle \sigma_x \rangle \\ \langle \sigma_y \rangle \\ \langle \sigma_z \rangle \end{pmatrix}. \tag{2.44}$$

In consequence, the polarisation of the whole beam can be expressed as average over the individual polarisations of all neutrons:

$$\boldsymbol{P} = \frac{1}{N}\sum_j \boldsymbol{p}_j \tag{2.45}$$

For an unpolarised beam $\boldsymbol{P} = 0$, on the other hand for a complete polarised beam $\boldsymbol{P} = 1$ and for a partial polarised beam $0 < \boldsymbol{P} < 1$. The component of polarisation of the beam P can be written as

$$P_\alpha = \frac{n^+ - n^-}{n^+ + n^-}, \tag{2.46}$$

with $n^\pm$ denoting the numbers of neutron in the $\pm\frac{1}{2}$ eigenstates.

2.3.2 Polarised neutron scattering

In the early 1960s the fundamental equation which describes the scattering of a polarised neutron beam was given, independently of each other, by Maleev and Blume [MBS,Blu]. In this subsection a brief overview about the polarisation of the scattered beam in the elastic case is presented according to [Brob]. The *Blume-Maleev equation* is given as:

$$\begin{aligned} P_f I = &\boldsymbol{P}_i \left(N_{\boldsymbol{Q}} N^*_{\boldsymbol{Q}} - \boldsymbol{M}_{\boldsymbol{Q}\perp} \cdot \boldsymbol{M}^*_{\boldsymbol{Q}\perp}\right) \\ &+ \boldsymbol{M}_{\boldsymbol{Q}\perp}\left(\boldsymbol{P}_i \cdot \boldsymbol{M}^*_{\boldsymbol{Q}\perp}\right) + \boldsymbol{M}^*_{\boldsymbol{Q}\perp}\left(\boldsymbol{P}_i \cdot \boldsymbol{M}_{\boldsymbol{Q}\perp}\right) + \boldsymbol{M}_{\boldsymbol{Q}\perp} N^*_{\boldsymbol{Q}} + \boldsymbol{M}^*_{\boldsymbol{Q}\perp} N^*_{\boldsymbol{Q}} \\ &- i\boldsymbol{P}_i \times \left(\boldsymbol{M}_{\boldsymbol{Q}\perp} N^*_{\boldsymbol{Q}} - \boldsymbol{M}^*_{\boldsymbol{Q}\perp} N_{\boldsymbol{Q}}\right) + i\left(\boldsymbol{M}_{\boldsymbol{Q}\perp} \times \boldsymbol{M}^*_{\boldsymbol{Q}\perp}\right) \end{aligned} \tag{2.47}$$

N_Q is the *nuclear structure factor* and $\boldsymbol{M}_{Q,\perp}$ the *magnetic interaction vector* of the chemical unit cell. $\boldsymbol{P}_i$ and $\boldsymbol{P}_f$ are the incident and scattered polarisation, respectively. The intensity (proportional to the differential cross section) of the scattered beam is given by:

$$\begin{aligned} I = &\underbrace{N_{\boldsymbol{Q}} N^*_{\boldsymbol{Q}}}_{\text{pure nuclear contribution}} + \underbrace{\boldsymbol{M}_{\boldsymbol{Q}\perp} \cdot \boldsymbol{M}^*_{\boldsymbol{Q}\perp}}_{\text{pure magnetic contribution}} \\ &+ \underbrace{\boldsymbol{P}_i \cdot \boldsymbol{M}_{\boldsymbol{Q}\perp} N^*_{\boldsymbol{Q}} + \boldsymbol{P}_i \cdot \boldsymbol{M}^*_{\boldsymbol{Q}\perp} N_{\boldsymbol{Q}}}_{\text{nuclear magnetic interference}} - \underbrace{i\boldsymbol{P}_i \cdot \left(\boldsymbol{M}_{\boldsymbol{Q}\perp} \times \boldsymbol{M}^*_{\boldsymbol{Q}\perp}\right)}_{\text{chiral magnetic contribution}} \end{aligned} \tag{2.48}$$

The pure nuclear as well as the pure magnetic contribution are independent of the initial polarisation. The nuclear-magnetic interference term appears if the nuclear and magnetic scattering take place at the same position in the $(\boldsymbol{Q}, \omega)$-space, and the chiral contribution depends on the initial polarisation. The relation between the incident polarisation $\boldsymbol{P}_i$ and the scattered polarisation $\boldsymbol{P}_f$ can be described by the tensor equation [Broa]

$$\boldsymbol{P}_f = \widetilde{\boldsymbol{P}}\boldsymbol{P}_i + \boldsymbol{P}^{'} \tag{2.49}$$

where $\widetilde{\boldsymbol{P}}$ is the polarisation tensor and $\boldsymbol{P}^{'}$ the polarisation created in the scattering process. Define a set of polarisation axis with x parallel to the scattering vector, z perpendicular to the plane of the incident and scattered beams and y completing the right-handed orthogonal set. In this configuration there is no component of $\boldsymbol{M}_{\boldsymbol{Q}\perp}$ perpendicular to x. The components of $\widetilde{\boldsymbol{P}}$ and $\boldsymbol{P}^{'}$ are given as:

$$\begin{aligned}\widetilde{\boldsymbol{P}}I &= \begin{bmatrix} N^2 - M^2 & J_{nz} & J_{ny} \\ -J_{nz} & N^2 - M^2 + R_{yy} & R_{yz} \\ -J_{ny} & R_{zy} & N^2 - M^2 + R_{zz} \end{bmatrix} \\ \boldsymbol{P}^{'}I &= \begin{pmatrix} -J_{yz} \\ R_{ny} \\ R_{nz} \end{pmatrix}\end{aligned} \tag{2.50}$$

with:

$$\begin{aligned} I_x &= M^2 + N^2 + P_x J_{yz} \\ I_y &= M^2 + N^2 + P_y R_{ny} \\ I_z &= M^2 + N^2 + P_z R_{nz} \\ I &= M^2 + N^2 + P_x J_{yz} + P_y R_{ny} + P_z R_{nz} \end{aligned} \tag{2.51}$$

where N denotes the nuclear structure factor with $N^2 = NN^*$, M is the magnetic interaction vector with $M^2 = \boldsymbol{M}_{\boldsymbol{Q}\perp} \cdot \boldsymbol{M}^*_{\boldsymbol{Q}\perp}$, $R_{ni} = 2\mathfrak{R}(NM^*_{\boldsymbol{Q}\perp i})$, $R_{ij} = 2\mathfrak{R}(M_{\perp i}M^*_{\perp j})$, $J_{ni} = 2\mathfrak{I}(NM^*_{\perp i})$ and $J_{ij} = 2\mathfrak{I}(M_{\perp i}M^*_{\perp j})$ with $M_{\perp i}$ denoting the ith component $(i = y, z)$ of $\boldsymbol{M}_{\boldsymbol{Q}\perp}$ and $\mathfrak{I}$ and $\mathfrak{R}$ the imaginary and real part, respectively. The off-diagonal components of $\widetilde{\boldsymbol{P}}$ represent the components of the scattered polarisation that are non-parallel to the incident direction and describe the rotation of the polarisation during the scattering process. The *polarisation analysis* is used to describe the experiments where the scattered polarisation is measured. A distinction is drawn between *classical polarisation analysis* [MRK], which measure only one component parallel to the applied field ($i = j = z$ and z parallel to the applied field), and the *3d polarisation analysis* [Sch], with $I^{\pm i \pm i}, i = x, y, z$. For both methods a magnetic field or magnetisation is present at the sample, therefore components perpendicular to the field cannot be measured. The off-diagonal components of $\widetilde{\boldsymbol{P}}$ can be detected by the so-called *spherical polarimetry* [TBLB+]. This work will be restricted to classical polarisation analyses, with the goal to investigate the polarised scattering on chiral magnets, which is described in more detail in the next section.

2.3.3 Chiral scattering

Throughout this work polarised neutron scattering is used to determine the handedness of magnetic spirals. As the unpolarised scattering from a spiral magnetic structure is already discussed in (2.2.3), the polarised case will be introduced in the following, and in particular, the resulting expressions for polarised elastic scattering from spiral magnetic structures. The average spin $\boldsymbol{S}_l$ and the vector $\boldsymbol{M}_{\boldsymbol{Q}}$ are given by:

$$\begin{aligned} \boldsymbol{S}_l &= \frac{1}{2}\left[\boldsymbol{S}\exp\left(-i\boldsymbol{k}\cdot\boldsymbol{l}\right)\boldsymbol{S}^{*}\exp\left(i\boldsymbol{k}\cdot\boldsymbol{l}\right)\right] \\ &= \boldsymbol{S}_1\cos\left(\boldsymbol{k}\cdot\boldsymbol{l}\right)+\boldsymbol{S}_2\sin\left(\boldsymbol{k}\cdot\boldsymbol{l}\right) \qquad (2.52) \\ \boldsymbol{M}_{\boldsymbol{Q}} &= \frac{r}{2N}F\left(\boldsymbol{Q}\right)\sum_{\tau}\left(\boldsymbol{S}\delta_{\boldsymbol{Q}-\boldsymbol{k},\boldsymbol{\tau}}+\boldsymbol{S}^{*}\delta_{\boldsymbol{Q}+\boldsymbol{k},\boldsymbol{\tau}}\right) \qquad (2.53) \end{aligned}$$

$\boldsymbol{l}$ is the coordinate of the site l and $\boldsymbol{\tau}$ is the reciprocal lattice vector. According to [Mala], the expression for the elastic scattering cross section of a magnetic spiral [MBS, Blu] can be derived as:

$$\begin{aligned} \sigma_{el} = \left[\frac{r}{2}F\left(\boldsymbol{Q}\right)\right]^2 &\left\{\left[\boldsymbol{S}_1^2-\left(\boldsymbol{S}_1,\hat{\boldsymbol{Q}}\right)^2+\boldsymbol{S}_2^2-\left(\boldsymbol{S}_2,\hat{\boldsymbol{Q}}\right)^2\right]\right. \\ &\left.\times\left(\Delta_{\boldsymbol{Q}+\boldsymbol{k}}+\Delta_{\boldsymbol{Q}-\boldsymbol{k}}\right)+2\left(\boldsymbol{P}_i\cdot\hat{\boldsymbol{Q}}\right)\left(\left[\boldsymbol{S}_1\times\boldsymbol{S}_2\right]\hat{\boldsymbol{Q}}\right)\left(\Delta_{\boldsymbol{Q}+\boldsymbol{k}}+\Delta_{\boldsymbol{Q}-\boldsymbol{k}}\right)\right\} \qquad (2.54) \end{aligned}$$

with

$$\Delta_{\boldsymbol{Q}\pm\boldsymbol{k}} = \frac{\left(2\pi\right)^3}{V_0}\sum_{\tau}\delta\left(\boldsymbol{Q}\pm\boldsymbol{k}-\boldsymbol{\tau}\right). \qquad (2.55)$$

Here V_0 is the unit cell volume. The superstructural peaks occur as for the unpolarised case at the positions $\boldsymbol{Q}=\pm\boldsymbol{k}+\boldsymbol{\tau}$. Using the identity [LB] $\boldsymbol{A}_\perp\times\boldsymbol{B}_\perp=\hat{\boldsymbol{Q}}\left(\left[\boldsymbol{A}\times\boldsymbol{B}\right]\hat{\boldsymbol{Q}}\right)$ and considering a simple spiral with $|\boldsymbol{S}_1|=|\boldsymbol{S}_2|$ and all vectors mutual perpendicular Eq.2.54 can be simplified to:

$$\begin{aligned} \sigma_{el} = \left[\frac{rS}{2}F\left(\boldsymbol{Q}\right)\right]^2 &\left\{\left[1+\left(\hat{\boldsymbol{Q}}\cdot\hat{\boldsymbol{m}}\right)^2+2\left(\boldsymbol{P}_i\cdot\hat{\boldsymbol{Q}}\right)\left(\hat{\boldsymbol{Q}}\cdot\hat{\boldsymbol{m}}\right)\right]\Delta_{\boldsymbol{Q}+\boldsymbol{k}}\right. \\ &\left.+\left[1+\left(\hat{\boldsymbol{Q}}\cdot\hat{\boldsymbol{m}}\right)^2-2\left(\boldsymbol{P}_i\cdot\hat{\boldsymbol{Q}}\right)\left(\hat{\boldsymbol{Q}}\cdot\hat{\boldsymbol{m}}\right)\right]\Delta_{\boldsymbol{Q}-\boldsymbol{k}}\right\} \qquad (2.56) \end{aligned}$$

For a right- and left-handed spiral, $\hat{\boldsymbol{m}}=\left[\boldsymbol{S}_1\times\boldsymbol{S}_2\right]/S^2$ and $\boldsymbol{k}$ are parallel and antiparallel, respectively. From Eq.2.53 and Eq.2.55 it follows that the scattering of polarised neutrons offers the possibility to determine the direction of the spirals rotation. The chirality can be identified by measuring the difference between the scattering intensities taken from the incident neutron beam with the polarisation along ($+P_i = \boldsymbol{P}_i \upuparrows \boldsymbol{H}$) and opposite ($-P_i = \boldsymbol{P}_i \uparrow\downarrow \boldsymbol{H}$) at a fixed $\boldsymbol{Q} = \boldsymbol{k}$. The value P_s, the difference between two intensities taken at the same $\boldsymbol{Q}$ normalised to their sum, allows to quantify the helix chirality. The helix chirality γ_m is connected with the individual measured scattered intensities and the incident polarisation by the relation [GMO+]

$$P_s(\boldsymbol{Q}) = \frac{I(+\boldsymbol{P}_i) - I(-\boldsymbol{P}_i)}{I(+\boldsymbol{P}_i) + I(-\boldsymbol{P}_i)} = \gamma_m \left(\boldsymbol{P}_i \cdot \hat{\boldsymbol{Q}}\right) = \gamma_m P_i \cos(\psi)\,. \tag{2.57}$$

ψ is the angle between the polarisation vector $\boldsymbol{P}_i$ and the unit scattering vector $\hat{\boldsymbol{Q}}$.

2.3.4 Experimental methods for neutron polarisation

The neutron beams from neutron sources are in general unpolarised. Currently, there are three methods to produce a polarised beam and analyse its polarisation after the scattering process, which will be shortly introduced here:

- **Bragg scattering from ferromagnetic crystals** The polarisation effect due ferromagnetic Bragg scattering is the first example of nuclear - magnetic interference [Shu]. The scattering amplitude for neutrons with spin parallel and antiparallel (±) is defined as [Mala]

  $$f_\pm = -\left\{b \pm rF(\boldsymbol{Q})\,\boldsymbol{S}\left[1 - \left(\hat{\boldsymbol{Q}} \cdot \hat{\boldsymbol{m}}\right)^2\right]\right\} \tag{2.58}$$

  The right choice of $\boldsymbol{Q}$ and $\boldsymbol{S}$ can set the amplitude f_- to zero, that only the neutrons with the polarisation along the field are Bragg scattered. Two possible materials that can be used for polarising the beam are the (111) reflection of the Heusler alloy Cu_2MnAl with a polarisation antiparallel to the field [SAMM] or (200) reflection of $Co_{92}Fe_8$.

- **Reflection from magnetised mirrors** The square of the refraction index for a neutron beam entering a material is given in [Mala] as

  $$n_0^2 = 1 - 2\pi\frac{N_0 b}{ME} \tag{2.59}$$

  N_0 is the density of the material, M is the mass and E the energy of the neutron. For a magnetised material the interaction between the neutron spin and the magnetic field in the sample becomes dependent on their relative orientation. At a proper glancing angle (often in the order of less than

1°) neutrons of one spin state are completely reflected, while the other state mainly penetrates the sample. Particularly tailored multilayer samples allow one to increase the incident angle. Typical materials for this kind of magnetised mirrors are Fe/Si, Co/Si or $Fe_{50}Co_{48}V_x/TiNi_x$ multilayers.

- **Using polarised nuclei of the isotope ^{3}He as filters** The neutron absorption of ^{3}He is strongly dependent of the relative orientation between the neutron spin and the one of the nuclei [PS, TR, HDH$^+$]. A ^{3}He filter strongly absorbs neutrons with a spin antiparallel to the nuclei spin but transmits the ones with the opposite spin.

Moreover, it is sometimes necessary to change the direction of the polarisation vector $\boldsymbol{P}$ during the experiment. This could be achieved by a specially designed magnetic field structure set along the path of the neutron. In a constant magnetic field the neutron polarisation vector rotates. This rotation is called *Larmor-precession*:

$$\frac{d\boldsymbol{P}}{dt} = -2\mu_n \left[\boldsymbol{B}\left(\boldsymbol{r}\right) \times \boldsymbol{P}\right] \tag{2.60}$$

The *Lamor frequency* is given by $\omega_L = 2\frac{|\mu_n|}{\hbar}|\boldsymbol{B}|$. One can distinguish different cases [Rob]. In the *adiabatic* case the field variation is slow compared to the *Larmor frequency* and the polarisation vector $\boldsymbol{P}$ follows the direction of the field. In the *non-adiabatic* case, on the other hand, the polarisation of the beam will not re-orient and instead the beam will keep processing along the initial orientation. The different experimental realisation of polarisation-rotation systems, are called *flipper*. In this work an *adiabatic fast passage (AFP) flipper* has been used (see [GGb, GGa, GGK] for details).

2.4 Small angle neutron scattering

Small Angle Neutron Scattering (SANS) is an elastic scattering method, which allows to probe large scale structures. Wide angle scattering experiments, on the contrary, applied for the investigation of inter-atomic distances. Typical diffraction experiments aims on the Q-range of approximately 10 Å^{-1} to 0.5 Å^{-1} or structural sizes of 1 nm to 0.1 nm, while small angle scattering (SAS) is aiming on large length scale properties. SANS is often applied to investigate soft condensed matter (e.g. colloidal particles, polymers, gels, liquid crystals), biology (e.g. proteins, biomembrans), material science (e.g. phase separation in alloys and glasses, morphology of superalloys), but also hard condensed matter (e.g. flux lines in superconductors, magnetic correlations). The typically covered Q-range is approximately between 0.0005 Å^{-1} and 0.5 Å^{-1} addressing length scales between 10 Å and 10000 Å. In this work spiral magnetic spin arrangements with a long periods between 30 Å for MnGe [KOA+,MTA+,KKI+] and 700 Å for FeGe [LBF] are investigated. For this reason, small angle neutron scattering is the perfect tool to probe the chiral, magnetic scattering arising from these phenomena. The SANS experiments in this work have been carried out at the SANS-1 [GOS+] instrument, which is located at the Heinz Maier Leibnitz Zentrum (MLZ), Garching, Germany and at D22 [d22] located at the Institute Laue Langevn (ILL), Grenoble, France. An overview about the specific characteristics of both instruments is given in Appendix A. SANS measures the scattering function $S(\boldsymbol{Q})$ in reciprocal space,

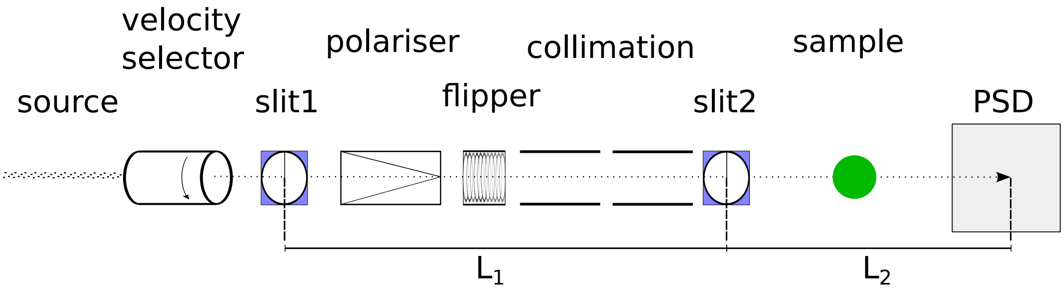

Figure 2.4: Schema of a small angle neutron scattering set-up.

transformed to the scattering length function $G(\boldsymbol{r})$ in real space, for the scattering vector $\boldsymbol{Q}$:

$$|\boldsymbol{Q}| = \frac{4\pi}{\lambda}\sin(\theta) \tag{2.61}$$

with the scattering angle 2θ. The schematic set-up of a monochromatic small angle neutron scattering instrument is presented in Fig.2.4. The wavelength of the neutrons λ is given by the tunable rotation speed of the velocity selector. After they passed the velocity selector an adaptable collimation and slit system generates a parallel flight path of the neutrons ('collimated' neutrons). In a typical pinhole like machine, there is one slit (R_1) located behind the velocity selector and a second one in front of the sample (R_2), with a typical distance between both slits of $L_1 = 10$ - 30 m. The scattered neutrons will be detected using a 2 dimensional position sensitive detector (PSD). To cover a broad Q-range the detector is movable to vary the sample-detector distance between 1 - 40 m. The collimation- and detector tubes are evacuated to prevent scattering by air, a polariser and a flipper are installed within the collimation tube. The experimental resolution is in general determined by the finite size of the incident beam, the wavelength resolution, the pixel size of the detector and the gravity effects [PPM]. The effect of the pixel sizes of the used detectors is between 8 × 8 mm^2 and 5 × 5 mm^2 and for this reason neglectable, the same is valid for the effect due to the gravity. For both SANS instruments, used within this work, the wavelength contribution given by

$\Delta\lambda/\lambda \approx 10$ %, dominates the instrument resolution and determines the width of the measured peaks. For a given Q the Q-resolution can be written (according to a Taylor series expansion) [Gri]:

$$\Delta Q = -Q\left(\frac{\delta\lambda}{\lambda}\right) + \left(\frac{4\pi}{\lambda}\right)\cos\left(\theta\right)\Delta\theta \tag{2.62}$$

and so:

$$\begin{aligned}\Delta Q^2 &= Q^2\left(\frac{\delta\lambda}{\lambda}\right)^2 + \left(\frac{4\pi}{\lambda}\right)^2\cos^2\left(\theta\right)\Delta\theta^2 = \Delta Q^2\left(\lambda\right) + \Delta Q^2\left(\theta\right) \\ &= Q^2\left[\left(\frac{1}{2\sqrt{2ln2}}\frac{\Delta\lambda}{\lambda}\right)^2\right] + \left[\left(\frac{4\pi}{\lambda}\right)^2 - Q^2\right]\Delta\theta^2 \end{aligned} \tag{2.63}$$

here the triangular function of the wavelength distribution is given by FWHM $= \lambda_0\left(\Delta\lambda/\lambda\right)$. θ is related to the width of the direct beam (see [Gri] for details). For the measurements presented in this work the solid solutions have been put inside the beam with the magnetic field perpendicular to the incident neutron beam. The optional polarisation $\boldsymbol{P}_0$ was applied parallel to the magnetic field $\boldsymbol{H}$.

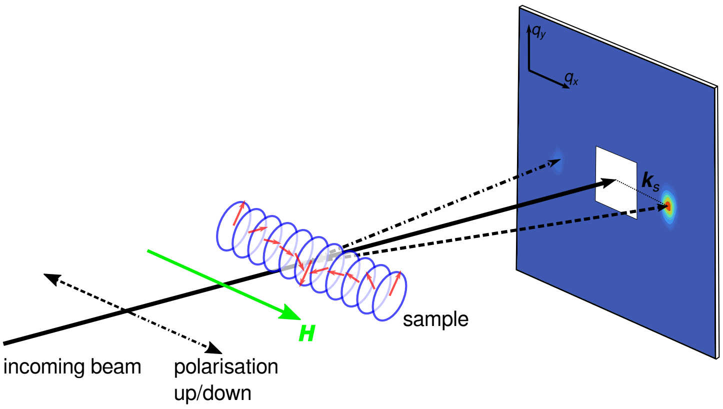

Figure 2.5: The schematic outline of a SA(P)NS experiment.

Chapter 3

Crystal structure and sample preparation

In the first section of this chapter the crystal structure of the investigated monosilicide and monogermanide samples will be introduced. The second section describes the synthesising methods used in this thesis: the monosilicides have been fabricated using the Czochralski method, while the monogermanides could only be produced under high pressure condition. In the last part the results from the x-ray characterisation are presented.

3.1 Crystal structure

The transition-metal monosilicides and -germanides MnSi, FeSi, CoSi, MnGe, FeGe, CoGe and their solid solutions crystallise in the chiral space group P$2_1$3 (B20 structure) [TTIE, TSES, LBF, DGO+]. They can be grown in a left-handed and right-handed crystalline chirality. Four transition metal atoms (Mn, Fe, Co) and four Si/Ge atoms occupying the Wyckoff positions [Hah]

$$\begin{aligned} 4(a): R_1\,(u,u,u)\,; &\qquad R_2\left(\tfrac{1}{2}+u,\tfrac{1}{2}-u,-u\right) \\ R_3\left(-u,\tfrac{1}{2}+u,\tfrac{1}{2}-u\right); &\qquad R_4\left(\tfrac{1}{2}-u,-u,\tfrac{1}{2}+u\right) \end{aligned} \tag{3.1}$$

For a right-handed crystalline chirality the positions for the atoms in the unit cells are $u_{Si/Ge} = 0.154$ and $u_{Me} = 0.865$ (where Me is the transition-metal) [IEM+, TTIE]. Consequential for the left-handed structure it must be $u^L_{Si/Ge} = 1$ - $u_{Si/Ge}$ and $u^L_{Me} = 1$ - u_{Me}. Using the same $u_{Si/Ge}$ and u_{Me} one get for the left-handed Wyckoff positions

$$\begin{aligned} 4(a): R_1\,(1-u,1-u,1-u)\,; &\qquad R_2\left(\tfrac{1}{2}-u,\tfrac{1}{2}+u,u\right) \\ R_3\left(u,\tfrac{1}{2}-u,\tfrac{1}{2}+u\right); &\qquad R_4\left(\tfrac{1}{2}+u,u,\tfrac{1}{2}-u\right) \end{aligned} \tag{3.2}$$

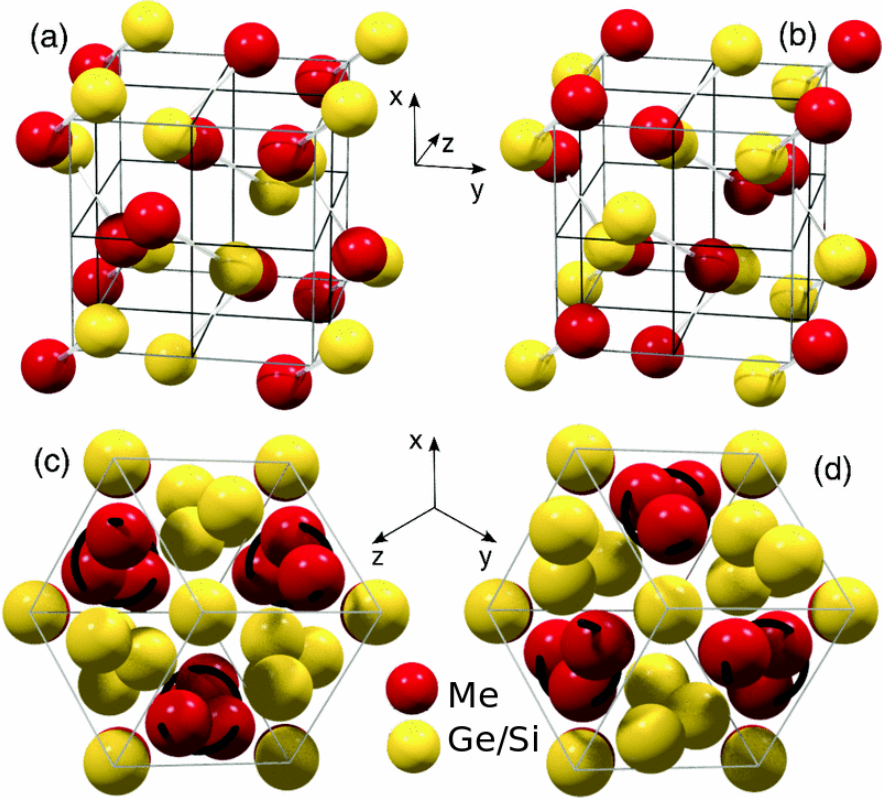

Figure 3.1: View of B20 cubic crystals along ⟨001⟩ (a), (b) and ⟨111⟩ (c), (d) for right-handed ((a) + (c)) and left-handed ((b) + (d)) configuration. The black spirals help to depict the sense of the spiral skewing (Reprinted figure with permission from [DGM+]. Copyright (2011) by the American Physical Society).

This is equal to the inversion operation (x, y, z) → (-x, -y, -z). To image the unit cells one can set the Me-Si/Ge pairs into the fcc lattice sites with the orientation along the ⟨111⟩ direction, at the four different sides [0, 0, 0], [0.5, 0.5, 0], [0, 0.5, 0.5] and [0.5, 0. 0.5]. The Me and Si/Ge atoms building helices with opposite sense skewing around ⟨111⟩. Fig.3.1 demonstrate a dextral- (right) and sinistral- (left)handed structures along the ⟨001⟩ direction (a), (b) and along the ⟨111⟩ direction (c), (d), respectively. Following the definition given by the authors of Refs. [IEM+,TTIE] the chirality of the whole structure coincides with the structure of the Si-sublattice. The Me-sublattice has the opposite chirality sense.

3.2 Sample preparation

For the monosilicide and monogermanide based compounds two different synthesis processes have been used. The $Fe_{1-z}Co_zSi$ samples with $z = 0.5, 0.6, 0.65, 0.75$ and 0.8 have been produced using the Tri-Arc-Czochralski device located at the Technische Universität Braunschweig [see Fig.3.2 (a)]. As it is proven in Ref. [DGM+] this method give almost 100 % control of the structural chirality. For the germanide based compounds, samples with a sufficient large size for the neutron scattering experiments can only be produced in powder form. The samples of $Fe_{1-y}Co_yGe$ (y running from 0.0 to 0.8) and $Mn_{1-x}Fe_xGe$ (x running from 0.0 to 1.0) have been synthesised as B20 structure using the high pressure method at the Institute for High Pressure Physics in Troisk [Tsv]. An exception is the pure FeGe, that can be produced using chemical vapour transport as single crystal sufficient large for neutron experiments as described in detail in Ref. [WSCG+].

3.2.1 Czochralski-method

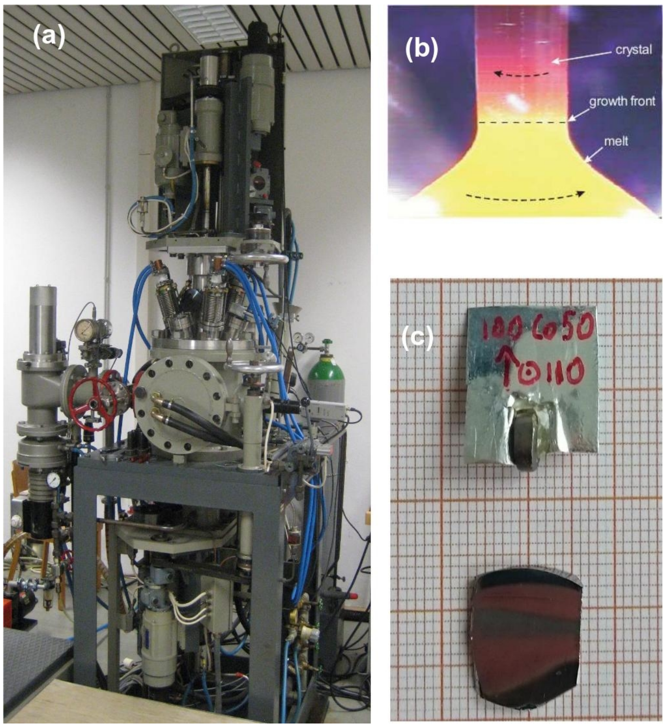

Figure 3.2: (a) the Tric-Arc Czochralski device, (b) view of the crystal growth process, (c) $Fe_{0.5}Co_{0.5}Si$ (top) and the MnSi reference sample (bottom).

To study the crystalline Γ_c as well as the magnetic chirality γ_m the availability of high-quality single crystalline sample is essential. The single crystals of MnSi as well as the $Fe_{1-z}Co_zSi$ compounds are grown using the Tri-Arc-Czochralski method [Czo]. This method is well established due to its intensive use in the semiconductor industry. For the Tri-Arc Czochralski method high purity components [99.98 % Fe (Alfar Aesar), 99.9 % Co (Alfa Aesar), Si (Preussag AG)] are mixed stoichiometrically and pre-molten in a water-cooled copper crucible under Argon atmosphere with a pressure of 0.6 bar for $Fe_{1-z}Co_zSi$ and 2.5 bar for MnSi. The pre-molten mixture is melted again in the Czochralski equipment under the same Argon atmospheres. Three electric arcs arranged in a 120 degree geometry provide a homogeneously heat contribution. The clockwise revolving seed crystal is submerged into the reversely rotating melt (see Fig.3.2 (b)). Subsequently the crystal is drawn out of the melt with a speed of 12 mm/h and the material starts to crystallise at the bottom of the seed. The crystal growth conditions are nearly identical for all samples, but due to their different vapour pressures the argon pressure has to be adapted for the samples containing Mn, Fe and Co. At the beginning of the growth process the crystal diameter is reduced to a few millimetres, the so called 'necking' (performed due a temperature change), which is a well established method to eliminate dislocations. It turned out that a reduction of the growth velocity during the necking to 2-3 mm/h reduces the probability that liquid melts tears of the crystal. Beside the ability to gain high-quality single crystalline samples, this method offers almost 100 % control of the crystalline chirality as revealed by Dyadkin and co-workers [DGM+]. Using a left-/right-handed seed crystal (necessarily with a similar crystal structure and similar cubic lattice parameters) it is possible to grow crystals with the same handedness as the seed crystal. In consequence, one gains the ability to control the handedness of the resulting crystal.

3.2.2 High pressure method

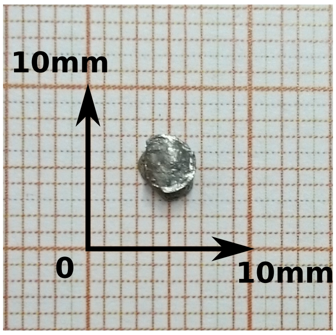

Figure 3.3: $Fe_{0.25}Co_{0.75}Ge$ produced via high pressure method.

Sufficient large samples for neutron scattering experiments of the transition metal monogermanides CoGe, MnGe and their composition (beside the pure FeGe) can only be produced in B20 structure under high temperature and high pressure condition. Consequently, most of the germanide based samples considered in this work exist only as polycrystalline powder with crystallite sizes in the order of a few microns. Here a short summary of the used method described in more details in Ref. [Tsv] will be given. The syntheses were carried out in a high pressure chamber constructed by Khvostantsev and co-workers [KVN]. A stoichiometric mixture of the elements has been pressed and placed in a rock salt pipe ampoule. The Mn purity was 99.0 % and that of Ge 99.999 %. This mixture has been placed in the high pressure chamber with a constant pressure of about 8 GPa and heated above the melting temperature of the mixture to 1600° C. Afterwards, the systems has been rapidly quenched to room temperature, whereupon the pressure has been released. The melting temperature could be controlled by the voltage-current plot. Subsequently, the crystalline structure has been checked by x-ray powder diffraction. The procedure has been repeated with slightly adapted temperatures and pressure values till the favoured B20 structure of the mixed compounds has been obtained.

3.3 X-ray characterisation

The structural chirality of $3d$ metals is nearly 100 % controlled by the chirality of the used seed crystal during the Czochralski growing [DGM+]. The Dzyaloshinskii-Moriya interaction offers a link between the structural and magnetic chirality that has been experimental proven for plenty of different $3d$ metals as pointed our above. It is absolutely essential to know the crystal structure and the structural chirality of the investigated samples. As all monogermanide based samples, besides MnGe[2] and FeGe, can be produced just in powder form one is limited to x-ray powder diffraction, whereas the single crystalline MnGe, FeGe and $\mathrm{Fe}_{1-z}\mathrm{Co}_z\mathrm{Si}$ sample can be investigated via single crystal diffraction. Following in this section the results from the powder diffraction experiments are presented in subsection 3.3.1 and the single crystal diffraction in subsection 3.3.2.

---

[2] It should be noted that the MnGe single crystals are sufficient large for the synchrotron single crystal diffraction but not for neutron experiments.

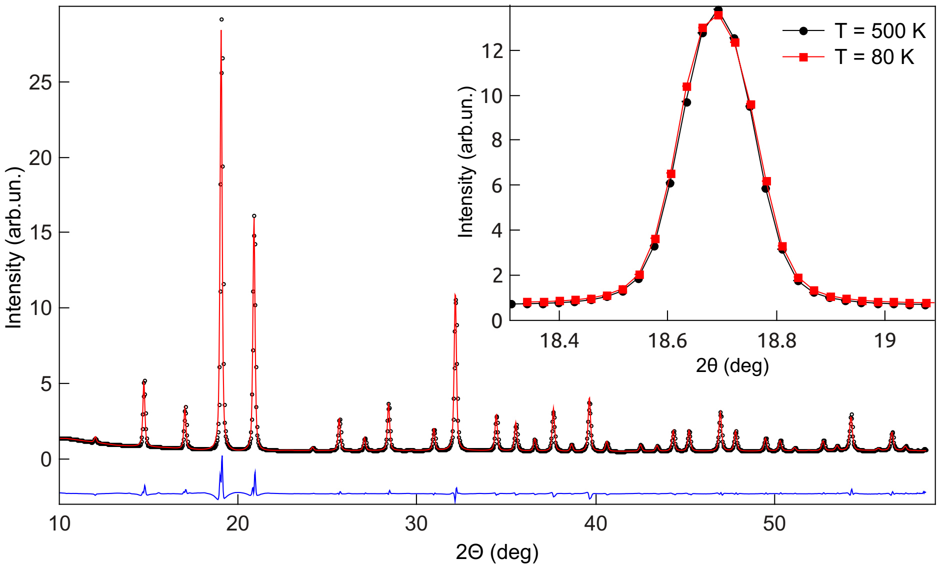

Figure 3.4: An example of a typical powder diffraction pattern taken for $Mn_{0.5}Fe_{0.5}$ Ge at $T = 200$ K. The inset shows the (120) peak for MnGe at $T = 80$ K (squares) and 500 K (circles), which is referred to have a maximal broadening due to the phase transition (proposed in Ref. [MTA+]). For comparison the peak at $T = 80$ K is shifted to the left by -0.1454° and scaled by a factor of 1.0874. It is clearly seen that there is no phase transition between these two temperatures (Reproduced with permission of the International Union of Crystallography from [DGO+]. Copyright (2014) International Union of Crystallography).

3.3.1 Powder diffraction

The $Mn_{1-x}Fe_xGe$ as well as the $Fe_{1-y}Co_yGe$ used in this thesis are in a polycrystalline powder form with a crystalline size not less than a micron [GPS+b, GSA+]. X-ray powder diffraction were performed at the PILATUS@SNBL [DPDC] diffractometer at the BM01A end station of the Swiss-Norwegian Beam Lines at the ESRF (Grenoble, France) (more details about the beamline parameters and performance can be found in Appendix A). In this sub-section the pre-characterisation on the powder samples will be introduced, exemplarily for $Mn_{1-x}Fe_xGe$, based on the work of Dyadkin and co-workers. [DGO+]. For the measurements a wavelength of 0.68239 Å have been used. The data have been collected using a single ϕ scan with an angular step of 0.1 ° in a shutter free mode using a Pilatus2M pixel area detector. To improve the powder averaging the 0.2 mm capillary was repeatedly oscillated over a 10° range. The temperature range between 80 K and 500 K was measured in 1 K steps. The SNBL Toolbox [Dya] has been used to reprocess the data, afterwards the azimuthally integration has been performed with Fit2D [Ham]

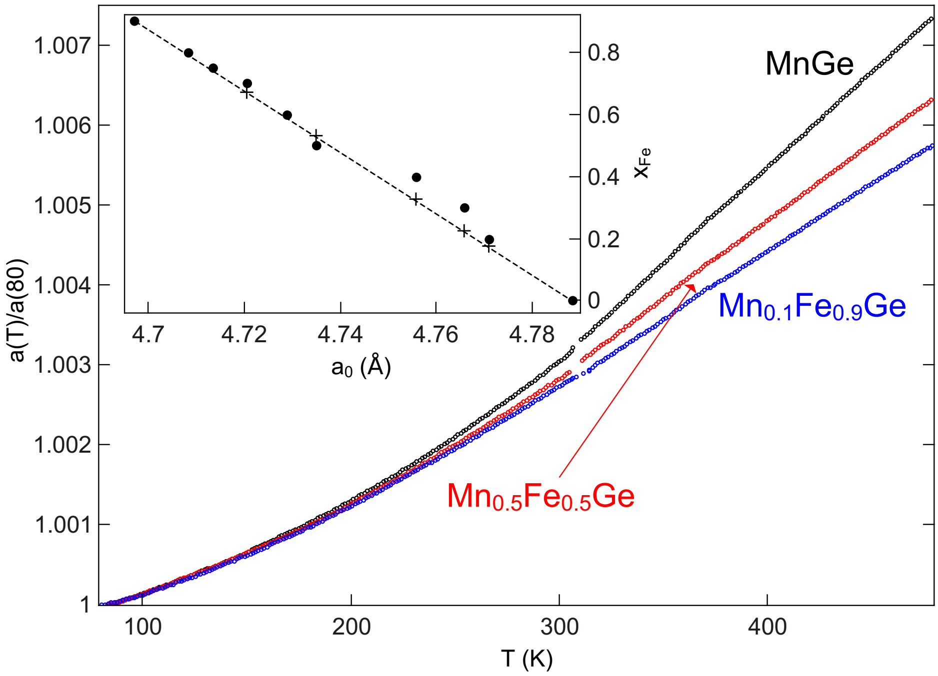

Figure 3.5: The temperature evolution of the unit-cell parameters normalised to the value of T = 80 K. Within the inset the Fe concentration x versus the low-temperature lattice parameter a_0 at T = 0 K, obtained from equation Eq.3.3 with crosses indicating values expected from Vegards law is plotted (Reproduced with permission of the International Union of Crystallography from [DGO+]. Copyright (2014) International Union of Crystallography).

and the final Rietvield refinement was carried out with FULLPROF [RC]. An example data set is illustrated in Fig.3.4. In contrast to the single crystalline samples the powder samples contain crystalline phases of unknown compositions with a varying number of contaminating phases from sample to sample. Fig.3.5 demonstrates the temperature evolution of the unit cell parameter in the range between 80 K and 500 K. The unit cell dimension decreases linearly as function of the concentration x (with a slope of -0.01), this behaviour is in a good agreement with the expected decrease of the average covalent radius of the 3d metal atoms. Dyadkin and co-workers assumed that the Vegards law is fulfilled. Some minor corrections have to be applied, which do not have any significant effect on the obtained results. For all compositions the thermal expansion fits to the Debye model (for each individual composition)

$$a\left(T\right) = a_0 + a_0\alpha\Theta_D f_D\left(\Theta_D/T\right) \tag{3.3}$$

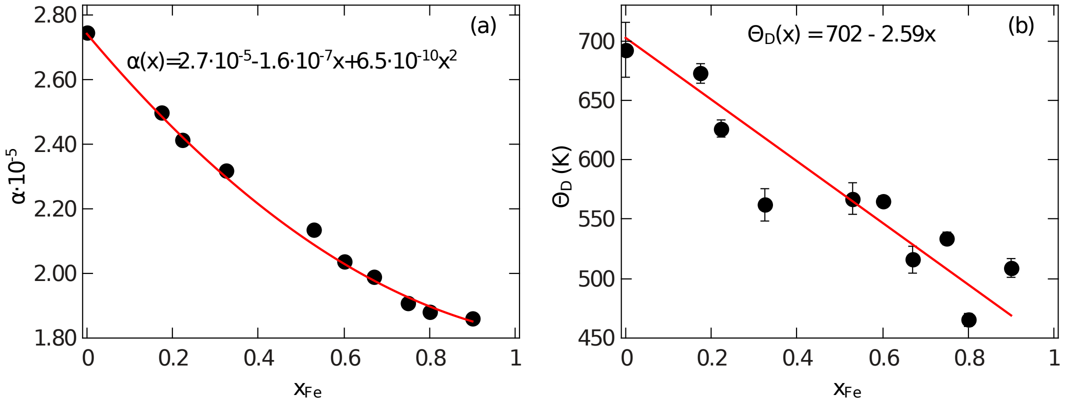

Figure 3.6: The concentration dependence of the thermal expansion coefficient α (a) and the Debye temperature Θ_D (b) from Eq.3.3 (Reproduced with permission of the International Union of Crystallography from [DGO$^+$]. Copyright (2014) International Union of Crystallography).

with

$$f(x) = 3\int_0^1 \frac{t^3}{\exp(tx)-1}dt \tag{3.4}$$

In Fig.3.6 the concentration dependence of the thermal expansion coefficient α and the Debye temperature Θ_D (including the minor corrections for the composition) is presented. The Debye temperature also decays with the increasing Fe concentration with a dispersion larger than for a_0. The thermal expansion α deviates clearly from linearity with the change of the $3d$ metal concentration. Neither from the powder patterns nor from the thermal expansion any indications for a phase transition around 170 K in pure MnGe could be observed (as proposed by Makarova and co-workers [MTA$^+$]).
The cubic B20 structure of the $Fe_{1-y}Co_yGe$ samples used within this thesis has been confirmed by laboratory x-ray diffraction. A detailed temperature dependent diffraction study using synchrotron radiation (analogous to the $Mn_{1-x}Fe_xGe$ presented here) is planned and will be performed in the nearest future.

3.3.2 Single-crystal diffraction

For the single crystal Bragg diffraction measurements a similar set-up has been used as for the powder diffraction measurements. The Bragg raw data have been processed with the SNBL Tool Box [Dya], the integral intensities have been extracted from frames with CRYSALISPRO [Tec], the crystal structure has been solved by SHELXS and refined by SHELXL [She]. The results for MnGe, FeGe and $Fe_{1-z}Co_zSi$ are given in Tab.3.1. For all single crystalline samples considered in this work the resonant scattering contribution to the x-ray scattering amplitude was sufficient to refine the so-called Flack parameter [Fla, FB, SSF].This analysis is based on the difference between the Friedel pairs $\left[I\left(hkl\right)-I\left(\bar{h}\bar{k}\bar{l}\right)\right]$. The measured difference provides a direct proof about the ratio between the two opposite-handed structural domains for chiral space groups. The value of the Flack parameter equal to zero corresponds to an enantiopure, i.e. only domains of the same chirality are present in the sample. Together with the atomic coordinates determined during the carried out refinement the absolute structure could be determined. In agreement with the previous works [GCD+a], the chirality Γ_c of a structure with $\mathrm{u}_{Me} \approx 0.86$ is right-handed ($\Gamma_c = +1$), whereas $\mathrm{u}_{Me} \approx 0.15$ is defined as left handed (Γ_c = -1). The single crystalline $Fe_{1-z}Co_zSi$ and the MnGe sample possess an $u_{Me} \approx 0.86$ and are therefore right-handed ($\Gamma_c = +1$), only the FeGe has an atomic position of $u_{Me} \approx 0.13$ and exist ergo in a left-handed structural chirality (Γ_c = -1). Together with the low Flack-parameter (Abs. structure parameter in Tab.3.1), one can assume that all single crystalline samples considered in this thesis are enantiopure. The Flack-parameter determined for all six samples is close to zero for each of them (see Tab.3.1). These results together with different single crystal diffraction experiments in the past [DGM+, GCD+a, GCD+b, GPS+b, WSCG+, DPG+], indicate that the energy barrier separating the two enantiopure domains is rather high implying that large domains with the same chirality are energetically favoured.

Table 3.1: Diffraction data for single-crystal refinement for MnGe, FeGe and $Fe_{1-z}Co_zSi$ with $z = 0.6, 0.65, 0.7, 0.8$.

		MnGe [DGO+]	MnGe [DGO+]	FeGe	$Fe_{0.4}Co_{0.6}Si$	$Fe_{0.35}Co_{0.65}Si$	$Fe_{0.3}Co_{0.7}Si$	$Fe_{0.2}Co_{0.8}Si$
Temperature (K)		90	250	293(2)	293(2)	293(2)	293(2)	293(2)
Crystal system		Cubic, B20	Cubic, B20	Cubic, B20	Cubic, B20	Cubic, B20	Cubic, B20	Cubic, B20
Space group		$P2_13$	$P2_13$	$P2_13$	$P2_13$	$P2_13$	$P2_13$	$P2_13$
Wavelength λ (Å)		0.68239	0.68239	0.71073	0.70800	0.70135	0.70814	0.70814
Unit-cell dimension a (Å)		4.7896(12)	4.7983(11)	4.70120(10)	4.468	4.46080(10)	4.454	4.455
θ range for data	θ_{min}	5.78	5.77	6.137	6.43	6.383	6.46	6.454
collection (°)	θ_{max}	24.93	24.88	26.153	32.11	23.631	31.83	23.909
Limiting indices		$-5 \leq h \leq 5$	$-5 \leq h \leq 5$	$-5 \leq h \leq 5$	$-5 \leq h \leq 5$	$-4 \leq h \leq 4$	$-6 \leq h \leq 6$	$-5 \leq h \leq 5$
		$-5 \leq k \leq 5$	$-5 \leq k \leq 5$	$-5 \leq k \leq 5$	$-6 \leq k \leq 6$	$-5 \leq k \leq 5$	$-5 \leq k \leq 5$	$-5 \leq k \leq 5$
		$-5 \leq l \leq 5$	$-5 \leq l \leq 5$	$-5 \leq l \leq 5$	$-6 \leq l \leq 6$	$-5 \leq l \leq 5$	$-6 \leq l \leq 6$	$-5 \leq l \leq 5$
Reflections collected/unique		505/78	522/78	434/69	717/107	396/50	712/107	370/49
R_{int}		0.0389	0.0308	0.0602	0.0304	0.0166	0.0217	0.0491
Completeness θ_{max} (%)		100	100	100	100	100	100	100
Final R indices $[I > 2\sigma(I)]$	R_1	0.0243	0.0220	0.0505	0.0122	0.0106	0.0093	0.0193
	wR_2	0.0539	0.0492	0.1434	0.0345	0.0287	0.0229	0.0424
Atomic positions	u_{Me}	0.8624(2)	0.8627(2)	0.1350(8)	0.86045(4)	0.85989(9)	0.85981(3)	0.85882(13)
	$u_{Si/Ge}$	0.15643(16)	0.15652(16)	0.8409(6)	0.15740(9)	0.1572(2)	0.15733(7)	0.1571(3)
Abs. structure parameter		0.01(11)	0.07(11)	0.02(5)	0.050(17)	0.01(4)	0.029(16)	-0.01(7)
Lattice chirality Γ_c		+1	+1	-1	+1	+1	+1	+1
Largest difference peak and hole (e Å^{-3})		0.542, -0.619	0.343, -0.679	1.246, -1.633	0.428, -0.340	0.202, -0.257	0.412,-0.280	0.349, -0.385

Chapter 4

Magnetic measurements

4.1 Motivation

$Mn_{1-x}Fe_xGe$, $Fe_{1-y}Co_yGe$ and $Fe_{1-z}Co_zSi$ are highly interesting magnetic ordered systems due to the broad range of new phenomena that are observed within this class of material. All of them are cubic B20 compounds with a non-centrosymmetric crystallographic structure described by the $P2_13$ space group with a helimagnetic spin ordering, but strongly different magnetic properties. These cubic helimagnetic B20 compounds attracted much attention during the last years due to the promising physical properties of the magnetic structure in the *A-phase*, which is the host of the so-called *skyrmion*-lattice. This topological protected structures are promising candidates for future high effective spintronic applications [MYS+,RHM+]. On the other hand, the 'simpler' helical phase of the systems that is the base of the *A-phase* is still not understood. The monogermanide compounds, which are less investigated due to their difficult synthesis, exhibit magnetic characteristics which differs clearly from the monosilicide based ones. The pure MnGe has a short helix pitch of 3 nm [TSES, KOA+, MTA+], a magnetic moment of 1.9 μ_B at 2.5 K [approximately 5 times larger than that of MnSi (0.4 μ_B)], and undergoes an intrinsic instability of the helix along with a complex order-disorder phase transition [ASD+]. In addition, a stress induced magnetic texture and fluctuation chiral phase [DBT+], as well as a pressure induced collapse of the magnetic order [DMH+] have been observed recently. While the pure FeGe, which is in principal a similar helimagnetic system, manifests strongly different magnetic properties. Its helix pitch of about 70 nm [LBF, WSCG+] is more than 20 times larger as for MnGe and goes along with a segmented *A-phase* [MGD+]. In all these compounds the major ferromagnetic exchange interaction together with the chiral Dzyaloshinskii-Moriya interaction stabilise the spiral magnetic structure below T_c [BJ, NYHK], while the weak anisotropic exchange fixes the spiral along the principal axis of the cubic system. As it is pointed out in the subsections 1.2.2, 1.2.3 and experimentally in Refs. [TTIE, IEM$^+$, GCD$^+$a, GCD$^+$b, DGM$^+$], the sign of the DM interaction determines the sense of the magnetic spiral. For various Mn-based monosilicide B20 compounds ($Mn_{1-x}Fe_xSi$ and $Mn_{1-x}Co_xSi$) the crystalline and magnetic chirality have the same sense, while for the Fe-based ones ($Fe_{1-z}Co_zSi$) the opposite behaviour seems to be the case. [TTIE, IEM$^+$, GCD$^+$a, GCD$^+$b, DGM$^+$]. This is a strong indication that the different types of compounds, Mn-/Co-based on the one hand, and Fe-based on the other hand, possess different signs of the DM interaction. It is of great interest to follow the change of the sign of the D constant by substituting more Fe/Co into the $Mn_{1-x}Fe_xSi$/$Mn_{1-x}Co_xSi$. Unfortunately $Mn_{1-x}Co/Fe_xSi$ are magnetically ordered just in a narrow range of doping and become non-magnetic with further Fe/Co doping. In contrast, the monogermanide systems, are due to their broader magnetic ordering range, more promising candidates to observe the magnetic structure development with doping of Fe/Co. In this work the evolution of the magnetic structure from pure MnGe to pure FeGe by continually substituting Mn by Fe and furthermore with Co doping to $Fe_{0.2}Co_{0.8}Ge$ (where the magnetic order disappears) has been investigated. Analogous to the germanide based compound the evolution of the chiral link with the tuning of the $3d$ electrons configuration by Fe/Co doping in $Fe_{1-z}Co_zSi$ compounds has been probed. The following chapter presents the results for the investigation of the microscopic and macroscopic magnetic structure in $Mn_{1-x}Fe_xGe$, $Fe_{1-y}Co_yGe$ and $Fe_{1-z}Co_zSi$ compounds using superconducting quantum interference device (SQUID) and small angle neutron scattering (SANS).

4.2 $\mathrm{Mn}_{1-x}\mathrm{Fe}_x\mathrm{Ge}$

The alloys of $\mathrm{Mn}_{1-x}\mathrm{Fe}_x\mathrm{Ge}$ offer the possibility to follow the changes of the magnetic properties from pure MnGe with Fe doping to pure FeGe and thereby observe the evolution of the link between structural and magnetic chirality within this compound sequence. In this chapter the results for the investigation of the magnetic structure of $\mathrm{Mn}_{1-x}\mathrm{Fe}_x\mathrm{Ge}$ via SQUID magnetisation (section 4.2.1), unpolarised (section 4.2.2) and polarised (4.2.3) SANS are presented. In addition, a short overview of the recent theory is given in section 4.2.4.

4.2.1 Magnetisation measurements: SQUID

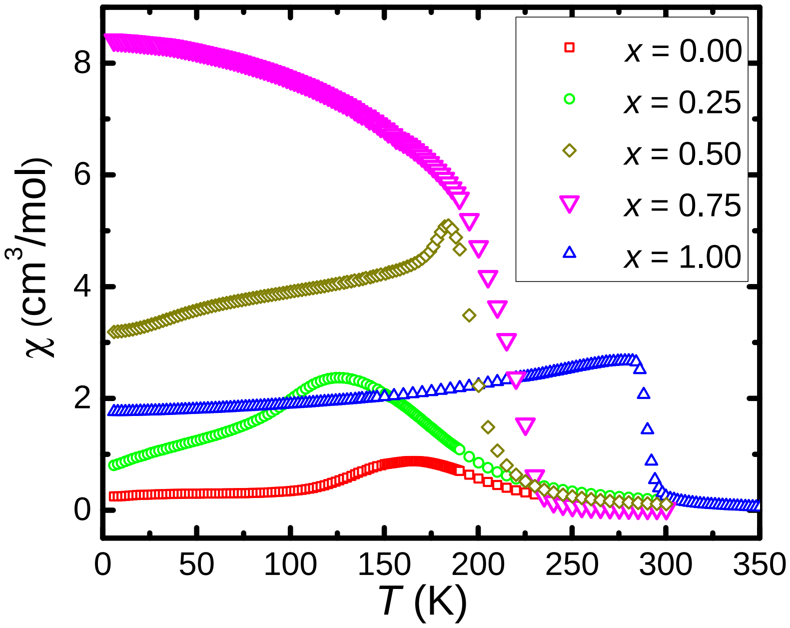

Figure 4.1: Temperature dependence of the susceptibility χ at an applied magnetic field of 50 mT for the compounds with $x = 0, 0.25, 0.5, 0.75, 1.0$. For better visibility the susceptibility of the compounds with $x = 0$ and $x = 0.25$ are multiplied by factor of 10 and that of the compound with $x = 0.5$ is multiplied by factor of 5 (figure taken from [GPS⁺b]).

The macroscopic magnetic properties of all samples with x running from 0.0 to 1.0 have been investigated by using a SQUID magnetometer (see Appendix A.2 for details). The temperature dependent dc-susceptibility curves have been measured between 5 and 350 K after zero-field cooling to 5 K and heating up in an external

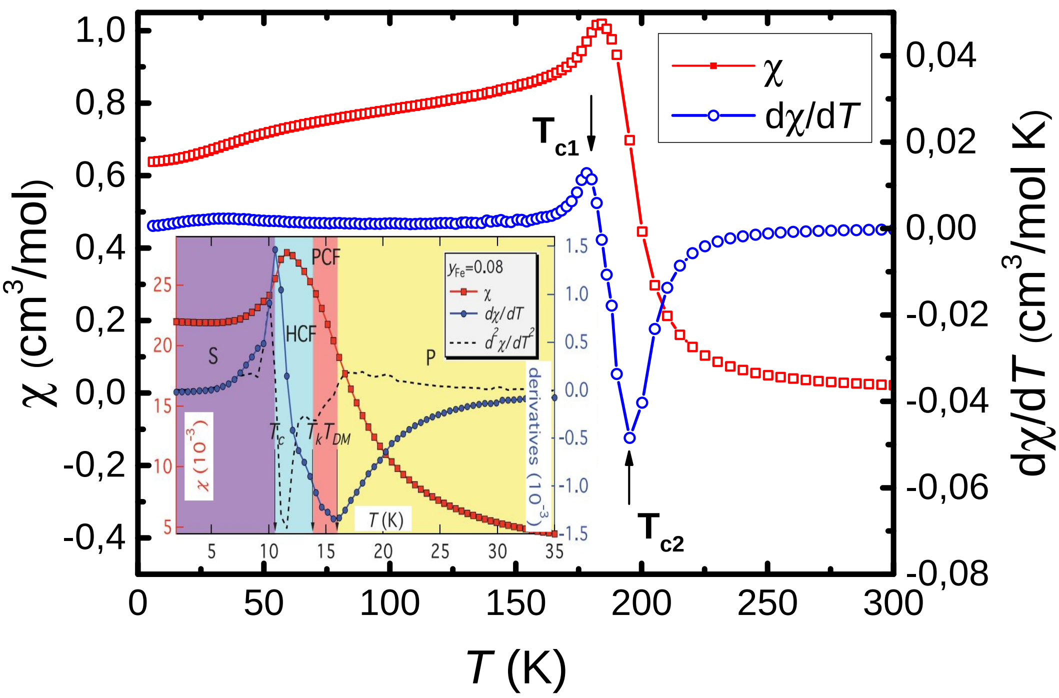

Figure 4.2: Temperature dependence of the magnetic susceptibility $\chi(T)$ of $Mn_{0.5}Fe_{0.5}Ge$ at $H = 50$ mT and the temperature derivative $d\chi/dT$. The critical temperature is taken from the lower maximum (T_{c1} at the maximum of the first deviation). The insert demonstrates the determination of the critical temperature in the similar DM helimagnet $Mn_{0.92}Fe_{0.08}Si$ (Reprinted figure with permission from [GMD$^+$b], Copyright (2011) by the American Physical Society).

field of 50 mT. In Figure 4.1 the susceptibility χ for $x = 0.0$, 0.25, 0.5, 0.75 and 1.0 are presented. As it was revealed for the similar helimagnetic system MnSi (find details in Ref. [GMD$^+$b]) the temperature driven transition from the paramagnetic to the helical phase could be accompanied by a chiral fluctuating state associated with a maximum in the susceptibility χ. The curves with $x = 0.0$, 0.25, 0.50 and 1.0 plotted in Fig.4.1 have the typical shape with a maximum as it is expected for a helical system. The critical temperature is determined as the low-temperature inflection point in the T dependence, corresponding to the maximum of the first derivative of the susceptibility on the temperature dχ/dT. In Fig.4.2 is exemplified for $Mn_{0.5}Fe_{0.5}Ge$. On the contrary, the curve with the critical concentration $x = 0.75$ shows a Curie-Weiss-like shape without any maximum, indicating a ferromagnetic spin structure. For all considered samples, the critical temperature is plotted versus the concentration x in Fig.4.3. It decreases slightly with increasing

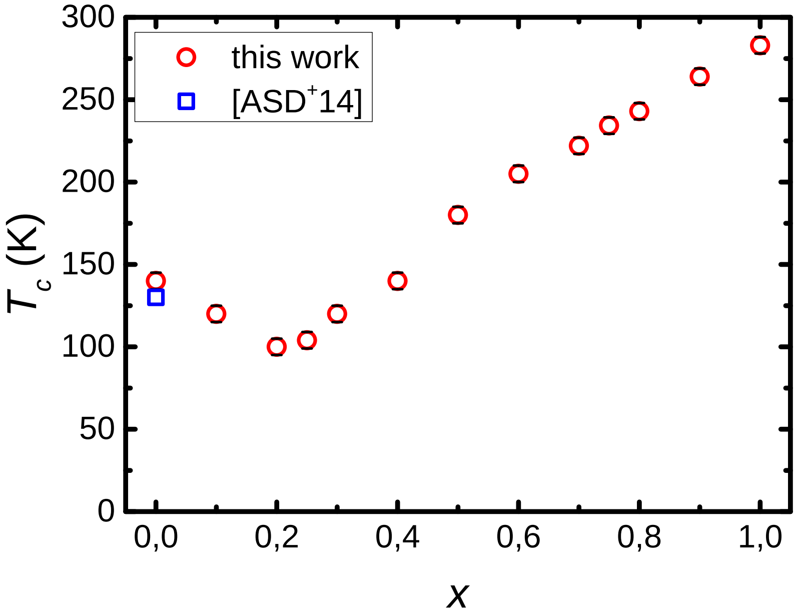

Figure 4.3: Dependence of the critical temperature T_c on the concentration x of $Mn_{1-x}Fe_xGe$ compounds. The red circles represent the critical temperatures determined by the maximum of the first derivation of the magnetic susceptibility measurements $d\chi/dT$ (as illustrated in [GMD+b]), the blue square is the lower critical temperature at which the stable helix transforms into a fluctuating helix (value taken from [ASD+])(figure taken from [GPS+b]).

x from approximately 140 K for MnGe to a minimum of 100 K for $x = 0.2$. With the further increase of the Fe-concentration, T_c increases monotonically again with a maximum of approximately 278 K for pure FeGe.

Recent small angle neutron scattering experiments carried out on pure MnGe revealed a more complex temperature driven order-disorder phase transition covering a temperature range of more than 100 K in pure MnGe [ASD+]. The stable helical spiral structure disappears at $T_c \approx 130$ K, and so 10 K below the critical temperature of $T_c \approx 140$ K as it was determined before in [GPS+b]. Further experiments will investigate also the compounds with increasing Fe-concentration if similar transitions exist in the nearest future.

4.2.2 Investigation of the helical phase: unpolarised SANS

The macroscopic measurements of the magnetic structure of the $Mn_{1-x}Fe_xGe$ compounds via SQUID are presented in the last section. As discovered in previous investigations the magnetic ground state of pure MnGe ([KOA$^+$]) as well as pure FeGe ([LBA$^+$]) is a proper spin helix with a helix length of $2\pi/|\boldsymbol{k}_s| \approx 3$ nm and 700 nm, respectively. As it is explained in section 2.2.3, the value of the wavevector k_s can be determined by neutron diffraction, the corresponding magnetic Bragg peaks are well accessible by small angle neutron scattering. The SANS measurements were carried out at the instrument D22 at the Institute Laue Langevin, Grenoble, France (see Appendix A.4 for details). The scattering intensities have been measured at the lowest reachable temperature ($T = 5$ K) after zero-field cooling. The schematic outline of all performed SANS experiment in this work is shown in Fig.2.5. All samples used for the experiment described in this chapter are powder samples, i.e. exist of randomly oriented grains and therefore it is not possible to align the sample in the beam along the principal axis. For a single crystalline sample, with one domain of magnetic spirals, pointing in the same direction one would expect superstructural peaks occurring at positions $\boldsymbol{Q} = \boldsymbol{\tau} \pm \boldsymbol{k}_s$ (as derived in subsection 2.2.3). Due the powder nature of the compounds the

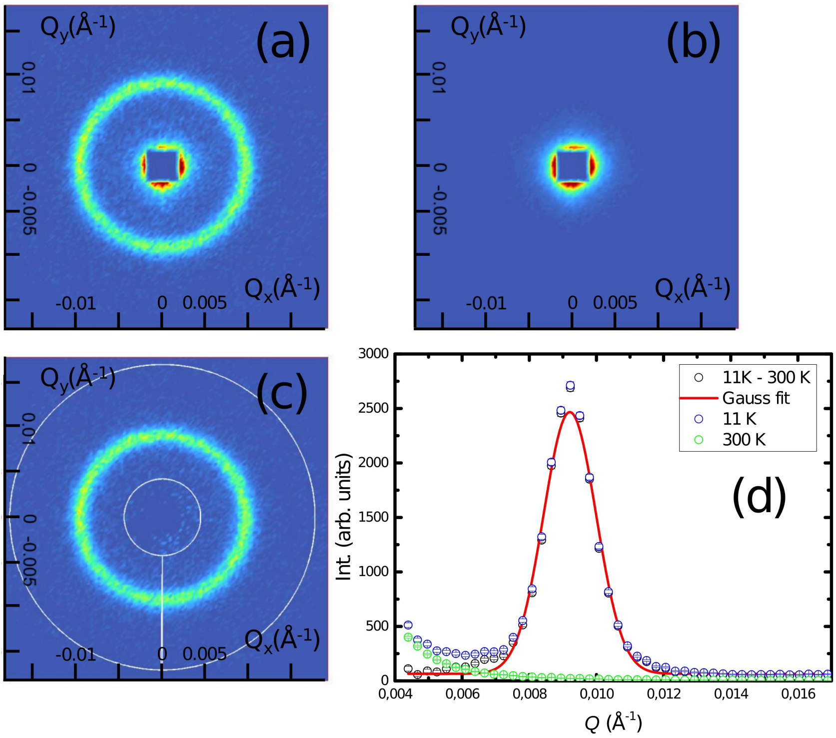

Figure 4.4: Maps of the SANS intensity for FeGe at 11 K (a) and 300 K (b). In (c) the map of 300 K is subtracted as background from the 11 K measurement. In (d) the momentum transfer dependence of the scattering intensities extracted from the maps (a) - (c) is presented (for the marked Q-range).

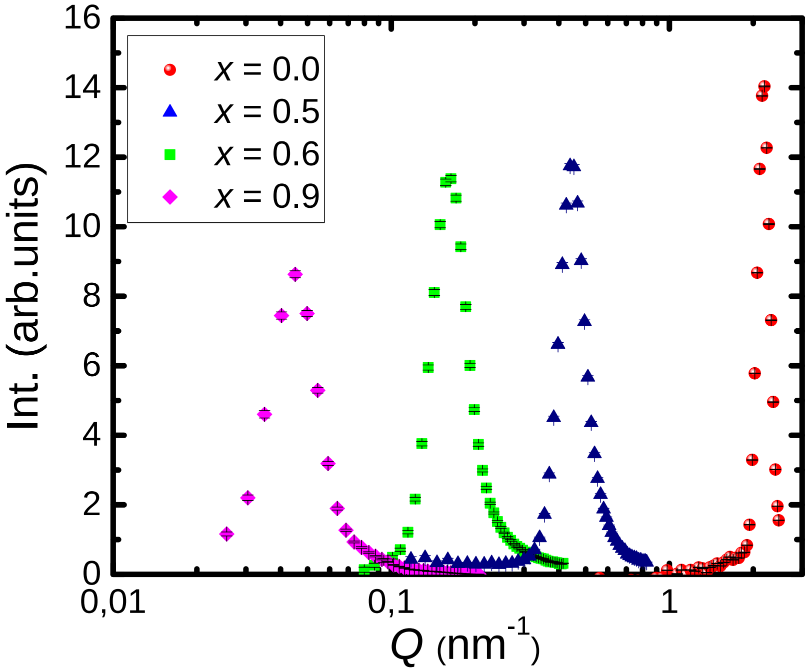

Figure 4.5: Momentum transfer dependence of the SANS intensity at $T \approx 20$ K for compounds with $x = 0, 0.5, 0.6, 0.9$. For a better visualisation of the remarkable change of the diffraction peak position $|\boldsymbol{k}_s|$ of 2 orders magnitude, the argument Q is plotted in a logarithmic scale. (figure taken from [GPS$^+$b]).

scattering maps exhibit a ring corresponding to the scattering from randomly oriented spiral domains with the same helix wavevector $|\boldsymbol{k}_s|$. The data treatment has been performed using the Graphical Reduction and Analysis SANS Program (GRASP) [Dew]. A typical example for a neutron scattering map is presented in Fig.4.4 (a) for pure FeGe recorded at 11 K, with the proper background measurement in (b) taken at 300 K and the corresponding subtracted map in (c). For more quantitative evaluation, the intensity is integrated azimuthally between the radii indicated by the two white circle in (c), as shown in (d). Afterwards, the Bragg peak is fitted by a single Gaussian curve and $|\boldsymbol{k}_s|$ is calculated from its centre position in Q. For all measurements the width of the peak is mainly determined by the particular resolution of the SANS instrument that is dominated by the $\frac{\delta\lambda}{\lambda} \approx 10\%$ wavelength resolution (see 2.4 for details of the SANS resolution). Since the width of the peaks is mainly due to the wavelength resolution, one can only determine a value for a minimal correlation length of ≈ 600 nm, however, it may be expected that the magnetic domains are far larger. The momentum transfer dependence of the scattering intensities $I(Q)$ are illustrated for different

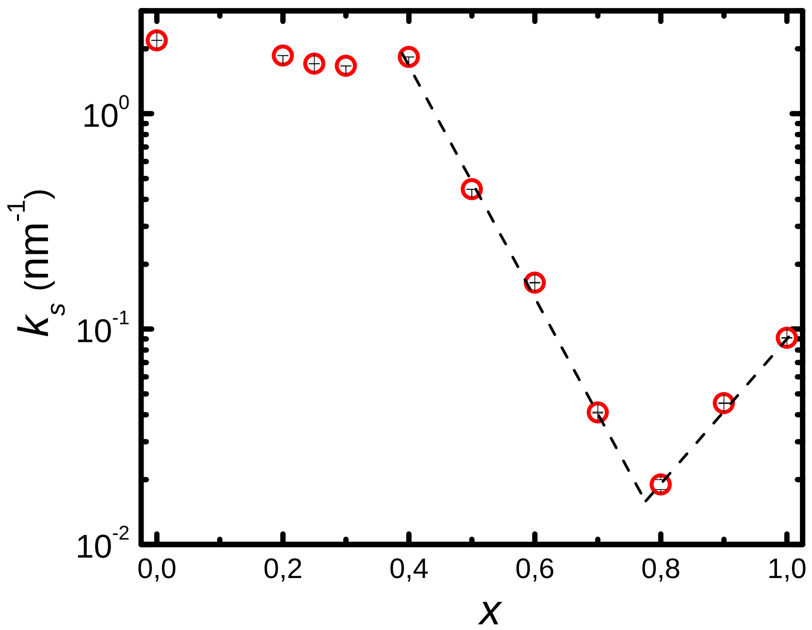

Figure 4.6: Dependence of the helix wavevector k_s on the concentration x (the lines are guides for the eyes) (figure taken from [GPS+b]).

compounds in Fig.4.5[3]. Analogous to FeGe the values of $|\boldsymbol{k}_s|$ have been extracted by the centre of the Gaussian fits. The intensities of the curves are not comparable due to the different ordered moment of each sample, the different samples masses, as well as the different neutron fluxes due to the different chosen collimations for each sample-detector position. The absolute scattering intensities, however, are not required for the extraction of $|\boldsymbol{k}_s|$. Figure 4.6 shows the x dependence of the helical wavevector $|\boldsymbol{k}_s|$, which gives the length of the helix pitch d via $d = 2\pi/|\boldsymbol{k}_s|$. The behaviour of k_s can be separated into three different regions. In the first Mn-rich region for $x \in [0.0 - 0.4]$, $|\boldsymbol{k}_s|$ stays roughly constant at 2.2 nm^{-1} corresponding to a helix pitch of approximate $d = 3$ nm. With increasing Fe concentration x, $|\boldsymbol{k}_s|$ decays to approximately zero at $x_c \approx 0.75$ while it increases again for higher concentrations up to a value of $|\boldsymbol{k}_s| = 0.09$ nm^{-1} ($d \approx 70$ nm for FeGe). Since the measurements were performed far below the ordering temperature, the vanishing helix wavevector for the sample with the concentration $x_c = 0.75$ can be interpreted as a ferromagnetic phase in full accordance to the results obtained by the macroscopic SQUID measurements (determined $T_c \approx 234$ K).

---

[3] It should be noted that due to the logarithmical scale the approximately equal width of the curves in Fig.4.5 appears to be different.

4.2.3 Investigation of the helical phase: polarised SANS

Using polarised small angle neutron diffraction, one can estimate the spin chirality of a magnetic system with spiral spin structure. The helix chirality γ_m can be quantified with the help of the polarisation of the scattered neutron P_s at a fixed point in the momentum space $\boldsymbol{Q} = \boldsymbol{k}_s$ via Eq.2.57:

$$P_s(\boldsymbol{Q}) = \frac{I(+\boldsymbol{P}_i) - I(-\boldsymbol{P}_i)}{I(+\boldsymbol{P}_i) + I(-\boldsymbol{P}_i)} = \gamma_m \left(\boldsymbol{P}_i \cdot \hat{\boldsymbol{Q}}\right) = \gamma_m P_i \cos(\psi)$$

where ψ is the angle between the polarisation vector $\boldsymbol{P}_i$, the unit scattering vector $\hat{\boldsymbol{Q}}$ and $I(+\boldsymbol{P}_i)$ and $I(-\boldsymbol{P}_i)$ are the integrated scattering intensities measured at the same point of reciprocal space, but for opposite initial polarisations. In this chapter the experimental results for the investigation of the chiral link between MnSi and FeGe are introduced. In a cubic B20 helimagnet the ferromagnetic

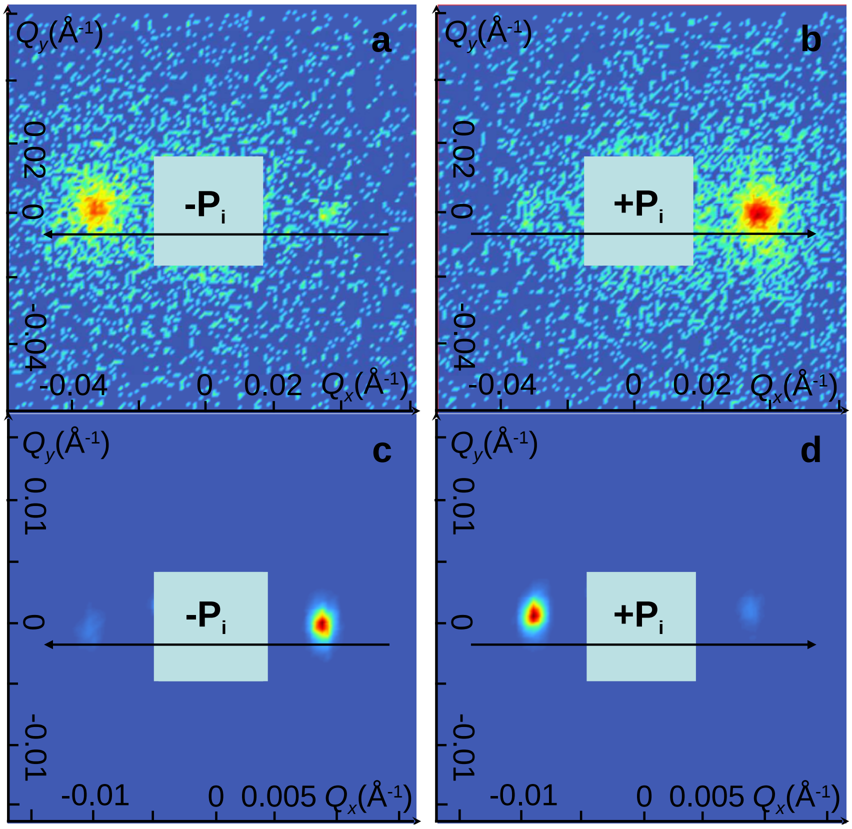

Figure 4.7: Maps of the SANS intensities of an MnSi sample (standard crystal) at $T = 25$ K and the FeGe crystal under study at $T = 260$ K for the polarisation $\boldsymbol{P}_i$ opposite to the guide field (a,c) and along it (b,d) (figure taken from [GPS+b]).

exchange interaction J and the Dzyaloshinskii-Moriya interaction with its constant D are balanced via $k_s = D/J$. The spin wave stiffness is defined as $A = S \cdot J \cdot a^2$, where S is the average spin moment and a the lattice constant. Consequently, as one can see by linking these two equations, the helix wave vector k_s is linked to the Dzyaloshinskii constant D via the equation given by Maleyev [Malb]:

$$k_s = \frac{SD}{A}. \tag{4.1}$$

The spin wave stiffness and the value of the spin moment can be assumed to be monotonic function of the Fe content, ergo, $|\boldsymbol{k}_s|$ going to zero implies that $|D|$ follows and also goes to zero. The sign of the wavevector $\boldsymbol{k}_s$, on the other hand, describes the chirality of the helical structure and is directly determined by the sign of the Dzyaloshinskii constant D. The transformation of the helix structure to a ferromagnetic arrangement at $x \to x_c$ could be the result of different signs of the Dzyaloshinskii-Moriya interaction. At x_c the different signs of D due to the different magnetic atoms involved just add up to a net constant D that becomes zero. To prove this hypothesis and explore the chiral link between the structural chirality Γ_c and the magnetic chirality γ_m above and below the critical concentration a study combining x-ray diffraction (see subsection 3.3.2 for details) and polarised neutron scattering (as described in section 2.3.3) have been applied. As introduced in section 2.3.2, Maleyev and co-workers as well as Blume [MBS,Blu] discovered that the spin chirality of a magnetic system can be estimated with the help of polarised neutron scattering. A measure for the different population of left- and right-handed domains is given by $|\gamma_m|$. $|\gamma_m| = 1$ corresponds to a single domain enantiomorph, while $|\gamma_m| = 0$ represents equal distributed left- and right-handed domains. Unfortunately, no single crystal of MnGe exists so far that is sufficient large to perform polarised neutron scattering. Though assumed that the magnetic chirality is determined by the equivalent transition metal (Mn or Fe), one may nevertheless gain indirectly insight in the sense of magnetic chirality in the system by comparing the chiral link between MnSi and FeGe. The link between structural and magnetic chirality is supposed to be identical for MnSi and MnGe. According to the definition [DCGD] the FeGe sample is left-handed (Γ_c = -1) [GPS+b] similar to the MnSi considered in this work [GCD+a]. The polarised small angle neutron scattering measurements were performed at the D22 instrument at the Institute Laue Langevin with an initial neutron beam polarisation of $P_i = 0.93$ and a mean wavelength of $\lambda = 0.60$ nm. A guide field of 1 mT was set along the $\boldsymbol{Q}_x$ direction. The typical SANS pattern from the MnSi sample below T_c with the initial polarisation opposite to (-$\boldsymbol{P}_i$) and along (+$\boldsymbol{P}_i$) the magnetic field are shown in Fig.4.7 (a) and (b), respectively. From earlier studies it is well know that for MnSi the left-handed structural chirality goes along with a left-handed magnetic chirality [GCD+a]. In consequence, the product of the crystallographic configuration times the magnetic chirality is $\Gamma_c \times \gamma_m$ = -1 × -1 = +1. For MnSi the magnetic chirality, γ_m, was obtained to be equal to -1 in the whole temperature range below T_c. SANS measurements on the FeGe sample were carried out using an equivalent set-up below T_c as shown in Fig.4.7 (c) for the polarisation opposite (-$\boldsymbol{P}_i$) and in Fig.4.7 (d) along ($\boldsymbol{P}_i$) the magnetic field[4]. The side of the peak is reversed for both systems, in consequence, it follows that they have a reversed magnetic chirality. For this reason, the product of both chiralities is $\Gamma_c \times \gamma_m = -1 \times -1 = +1$ for MnSi and the opposite case $\Gamma_c \times \gamma_m = -1 \times +1 = -1$ is valid for FeGe.

---

[4] It should be noted that due to the different instrument settings and samples the measurements of MnSi and FeGe shown in Fig.4.7 show different noise.

4.2.4 Theoretical interpretation

In this section an overview about the theoretical approaches to reproduce the sign change of the DM constant D at the critical concentration x_c will be given. The sign of the Dzyaloshinskii-Moriya constant caused by different helix chiralities related to the different electron configuration of the magnetic atoms (Fe and Mn) above and below x_c. Complementary to the polarised neutron scattering experiments Shibata and co-workers discovered a similar flip of the chiral link between the structural and magnetic chirality for $\mathrm{Mn}_{1-x}\mathrm{Fe}_x\mathrm{Ge}$ within the *A-phase* in the so-called *skyrmion* structure [SYH+]. At the moment three theoretical approaches exist to reproduce the experimental results (an overview about all of them is given in Appendix B): a Monte Carlo simulation by Chen and co-workers [CXYL] as well as the ab initio density-functional theory (DFT) calculation by Gayles and co-workers [GFS+] and Koretsune and co-workers [KNA]. The calculated strength

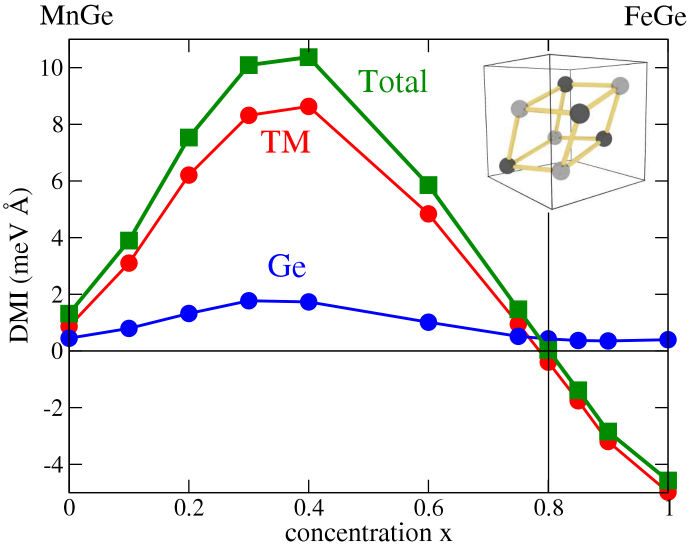

Figure 4.8: Strength of the DM as function of the Fe concentration. The total value is the sum of the contribution coming from the transition metal and the Ge (Reprinted figure with permission from [GFS+], Copyright (2015) by the American Physical Society).

of the DM as function of the Fe concentration as it is calculated by Gayles and co-workers is given in Fig.4.8, which is in good agreement with the experimental results given here and by Shibata an co-workers [SYH+]. The value determined in this thesis of $x_c = 0.75$ is slightly different from the theoretical determined value by Chen and co-workers $x_{c,Chen} = 0.7$ and Gayles and co-workers of of $x_{c,Gayles} = 0.8$. This could be due to a small derivation of the real concentration of the investigated sample, or the existence of a certain critical range $0.7 \lesssim x_c \lesssim 0.8$. A more detailed sampling around x_c is necessary to verify this idea. Koretsune and coworkers were able to qualitatively reproduce the experimental results $D < 0$ in the Mn-like region and $D > 0$ in the Fe-like one, however, the calculated critical value of $x_{c,Koretsune} = 0.45$ deviates clearly from the experimental values. The transformation of the spiral to the ferromagnetic structure will be discussed in respect to the competition between the Dzyaloshinskii-Moriya interaction and the cubic anisotropy in section 4.3.3.

4.2.5 Discussion

The three main findings concerning the $Mn_{1-x}Fe_xGe$ compounds are the following:

- the possibility to control the size of the helimagnetic structure in a range of two magnitudes
- the transformation of the spiral spin structure to a ferromagnetic-like at the critical concentration $x_c \approx 0.75$
- different signs of the link between structural and magnetic chirality for $x < x_c$ and $x > x_c$

The ability to continuously tune the size of the helical structure by a factor of 25 between pure MnGe and FeGe and even by two orders of magnitudes between MnGe and $Mn_{0.2}Fe_{0.8}Ge$ may be of great importance for the development of future spintronic devices. Moreover, the transformation from the spiral to a ferromagnetic spin structure within a cubic B20 helimagnetic system with Dzyaloshinskii-Moriya interaction has been demonstrated. The results presented in the previous sections give strong evidence for the hypothesis that different signs of the Dzyaloshinskii-Moriya interaction and the different helix chiralities related to the different magnetic atoms (Fe and Mn) are the reason for the transformation of the helix structure. The findings concerning $Mn_{1-x}Fe_xGe$ are summarised in Tab.4.1 with the results similar to the monosilicide based transition metals. It has to be mentioned

Table 4.1: Crystal chirality Γ_c and magnetic chirality γ_m of the compounds with $P2_13$ structure. (+1) and (-1) corresponds to the right and left chirality, respectively [GPS+b, GCD+a, GCD+b, DGM+].

Compound	$\Gamma_c \rightarrow \gamma_m$	$\Gamma_c \times \gamma_m$
MnSi	$+1(-1) \rightarrow +1(-1)$	$+1$
MnGe	$+1(-1) \rightarrow +1(-1)$	$+1$
FeSi	$+1(-1) \rightarrow -1(+1)$	-1
FeGe	$+1(-1) \rightarrow -1(+1)$	-1

that the magnetic chirality could not be directly measured for MnGe because of the powder crystalline form of the sample. But due to the dominating role of the $3d$ occupying element and the negligible role of the silicide/germanide, the magnetic chirality of MnSi is expected to be identical to MnGe. The properness of this assumption have been reproduced experimentally by Lorentz microscopy [SYH$^+$] as well as by simulations [CXYL, GFS$^+$, KNA].

4.3 $\mathbf{Fe_{1-y}Co_yGe}$

In the previous section, experimental evidences were presented for the alternation of the link between the crystalline and magnetic chirality by mixing two types of magnetic sites, here Fe and Mn. Grigoriev and co-workers formulated the hypothesis that the Mn and Co based monosilicides/-germanides should have the same chiral link, while it is opposite for Fe based compounds [GPS+b]. Apparently it is interesting to verify this hypothesis by following the evolution of the magnetic structure starting from pure FeGe with subsequently replacing the Fe sites by Co atoms. In this section the experimental results for the compound series $Fe_{1-y}Co_yGe$ are presented.
As discussed above the non-centrosymmetric space group of these compounds produces a chiral spin-spin DM interaction. According to the model of Bak and Jensen [BJ], and also independently shown by Kataoka and co-workers [NYHK], the helical (homochiral) structure is stabilised by the ferromagnetic exchange interaction J together with the DM interaction D below T_c. These two interactions are balanced via the helical wavevector k_s:

$$k_s = \frac{D}{J}. \tag{4.2}$$

Bak and Jensen did not introduce any limits for the critical field strength as well as for the size of the wavevector $|\boldsymbol{k}_s|$, both can become arbitrarily small. Kataoka and co-workers, on the other hand, took the cubic anisotropy into account [NYHK]. At small $|\boldsymbol{k}_s|$, it becomes comparable to the DM interaction and destabilises the helical structure in favour for a ferromagnetic spin structure. When a magnetic field is applied above a first critical field H_{c1}, the helical spin structure starts canting and transforms to a single conical domain, accompanied by the rotation of the corresponding wavevector $\boldsymbol{k}_s$ towards the direction of the applied field. Finally above a second critical field, H_{c2}, the spins align parallel in a collinear ferromagnetic spin state. As it was demonstrated in previous works [Malb, BRP] the energy between the helical and the ferromagnetic state is given via the second critical field H_{c2}:

$$g\mu_B H_{c2} \approx A k_s^2 \tag{4.3}$$

with the spin wave stiffness $A = J \cdot S \cdot a^2$ where S is the ordered spin and a the lattice constant. By determining k_s, H_{c2} and S all parameter describing the magnetic system are known and it is possible to calculate the ferromagnetic exchange interaction J and the DM interaction D. Below the SQUID magnetisation and SANS results will be presented for $Fe_{1-y}Co_yGe$, followed by the discussion of the role of the cubic anisotropy.

4.3.1 Magnetisation measurements: SQUID

The whole concentration range of $Fe_{1-y}Co_yGe$ compounds with $y \in [0.0, 1.0]$ has been synthesised. Similar to the $Mn_{1-x}Fe_xGe$ compounds discussed in section 4.2.1, they can only be synthesised under high pressure, resulting in a polycrystalline powder with a crystallite size in the order of a few microns (see [Tsv] for details). The B20 structure was confirmed by laboratory x-ray powder diffraction measurements. A more detailed temperature and pressure dependent x-ray diffraction study, analogous to the studies on $Mn_{1-x}Fe_xGe$ presented in section

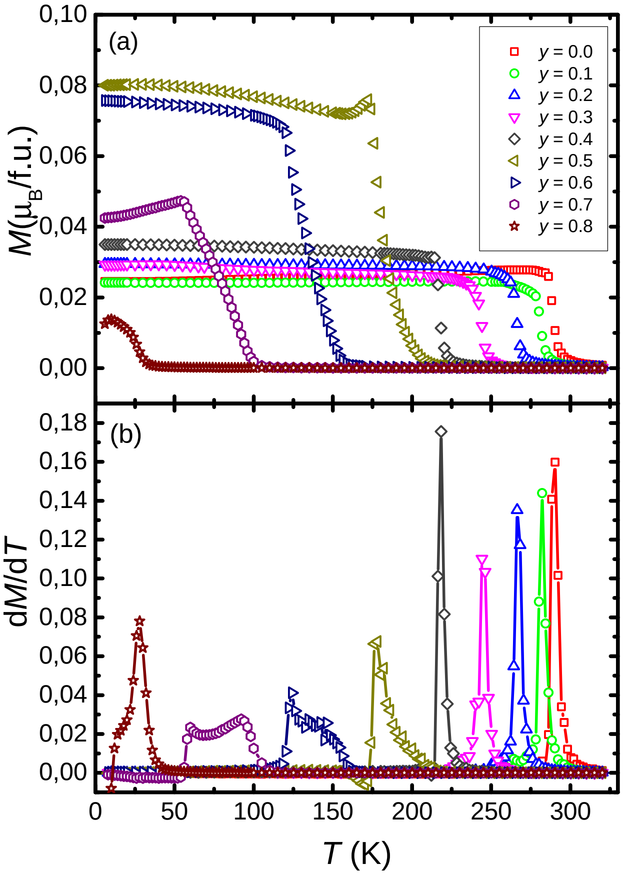

Figure 4.9: (a) The temperature dependence of the magnetisation M for $Fe_{1-y}Co_yGe$ compounds with $y = 0.0 - 0.8$ at $H = 10$ mT measured by SQUID and (b) the first derivative of the magnetisation on the temperature dM/dT (figure taken from [GSA+]).

3.3.1, using synchrotron radiation is planned and will be performed at the PILATUS@SNBL diffractometer (ESRF, Grenoble) in the nearest future. While pure FeGe possess helical and ferromagnetic spin states, as discussed in section 4.2, pure CoGe is a Pauli paramagnet [TSF+]. The macroscopic SQUID magnetisation measurements have been performed analogous to measurements for the $Mn_{1-x}Fe_xGe$ compounds using the same SQUID-magnetometer Quantum Design MPMS-5S (see Appendix A.2 for details). The temperature scans of the magnetic susceptibility for different compounds after zero-field cooling in a field of $H = 10$ mT are plotted in Fig.4.9 (a) and the corresponding first derivative of the magnetisation on the temperature dM/dT in Fig.4.9 (b). As discussed in section 4.2.1, the ordering temperature can be determined as the position of the sharp maxima of the first derivative of the magnetisation in respect to the temperature dM/dT [Fig.4.9 (b)]. This maximum observed for the compounds with $x = 0.0 - 0.5$ transforms into a broader distribution with two peaks for the compounds with $x = 0.6$ and $x = 0.7$. The change of the form from one to two features indicating that the magnetic phase transition for these two concentrations becomes more complex. As it was evidenced for the similar helimagnetic system $Mn_{1-x}Fe_xSi$ (find details in [GMD+b]) and observed in $Mn_{1-x}Fe_xGe$, in the previous section, the temperature driven transition from the paramagnetic to the helical phase may

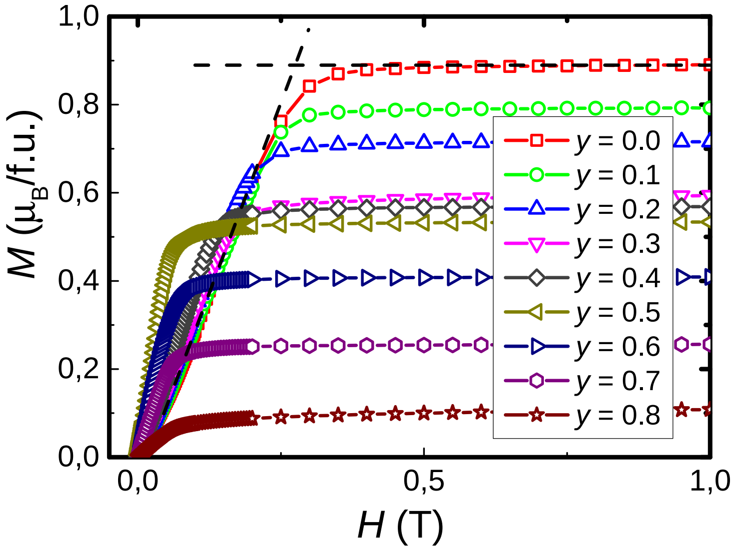

Figure 4.10: The magnetic field dependence of the magnetisation M for $y = 0.0 - 0.8$ at $T = 5$ K. The dashed lines are the linear approximations to the low and high field range. The crossing point is used to estimate the value of the second critical field H_{c2}, as it is done exemplary for $y = 0.0$. (figure taken from [GSA+]).

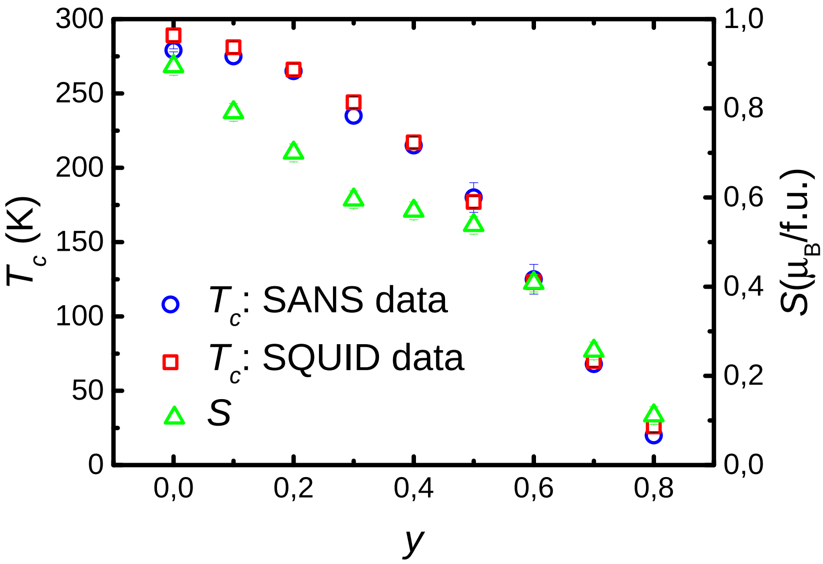

Figure 4.11: Dependence of the critical temperature T_c and the ordered spin value S on the concentration y of $\mathrm{Fe}_{1-y}\mathrm{Co}_y\mathrm{Ge}$ compounds determined by SQUID and unpolarised SANS (described in the next section) measurements (figure taken from [GSA$^+$]).

go through a complex crossover, from paramagnetic to partially chiral, from partially chiral to fully chiral fluctuating state and further to the spiral state. The high-temperature maximum is used to determine the critical temperature for the beginning magnetic ordering for the particular compound. The dependence of the so determined ordering temperatures on the y-concentration is shown in Fig.4.11. T_c decreases monotonically with increasing y and approaches zero for $y \to 0.9$. Besides, magnetisation curves are recorded at low temperature ($T = 5$ K) as plotted in 4.10. These measurements allow to estimate the second critical field H_{c2}, which is a measure for the different energy between the ferromagnetic aligned and the helimagnetic state below and above H_{c2}, respectively. Beside the second critical magnetic field the value of the ordered spin S could be estimated by the SQUID magnetisation measurements. Together with the helical wavevector these two parameters describe the helimagnetic system completely. For all investigated $\mathrm{Fe}_{1-y}\mathrm{Co}_y\mathrm{Ge}$ (with $y = 0.0-0.8$) the magnetisation curves increase linearly at small fields and saturate at H_{c2}, which is a characteristic field of the transformation from the conical (non-collinear) to the ferromagnetic collinear state. The critical field is estimated from the magnetisation as cross points of the linear approximation from the low-field and high field ranges as it is illustrated in Fig.4.10. An example for this is given for $y = 0.0$ in Fig.4.10. Additionally, the values of the ordered spin per atom S as function of the concentration y are plotted in Fig.4.11, as it could be estimated directly from the magnetisation curves. Similar to the critical temperatures, the ordered moments decrease with y, but exhibits a shoulder around $y = 0.4$. In conclusion, the SQUID measurements presented in this section clearly show that magnetic ordering persists up to $y = 0.8$ for the $Fe_{1-y}Co_yGe$ compounds.

4.3.2 Investigation of the helical phase: unpolarised SANS

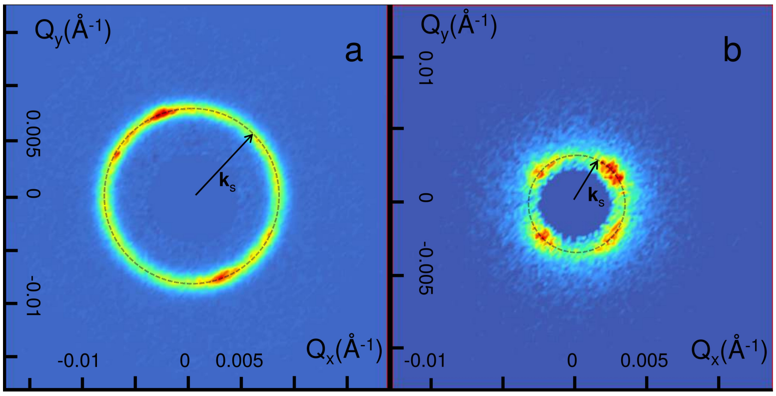

Figure 4.12: The small angle neutron scattering maps for the compounds with $y = 0.1$ (a) and 0.5 (b) at $T \approx 10$ K (figure is taken from [GSA+]).

The microscopic magnetic structure of the $Fe_{1-y}Co_yGe$ compounds has been investigated by small-angle neutron scattering. The experiments were carried out at the SANS-1 at the Maier-Leibnitz-Zentrum (see Appendix A.3 for details), where a Q-range from 2×10^{-2} to 1 nm^{-1} has been covered. The SANS scans have been carried out with a magnetic field perpendicular to the incoming neutron beam and a strength of maximal 0.5 T in a temperature range between 10 and 300 K with an accuracy of $\Delta T = 0.1$ K. Fig.4.12 shows two typical scattering maps for $y = 0.1$ [Fig.4.12(a)] and $y = 0.5$ in [Fig.4.12(b)], both recorded at $T \approx 10$ K. The observed scattering pattern are similar to the ones taken at low temperature and zero magnetic field for $Mn_{1-x}Fe_xGe$ (see Fig.4.4). The intensity ring exhibited in the SANS maps corresponds to the scattering from randomly oriented spiral domains with the same helix wavevector $|\boldsymbol{k}_s|$. The observed spots are due to the scattering of the relative large magnetic domains of the helical spin structure limited by the micrometer sized crystal grains. These are slightly different distributed in size and orientation, resulting in the observed higher intensity spots within the ring. For all measurements in this section the peak width is determined by the resolution of the SANS instrument, analogous to the measurements done at $Mn_{1-x}Fe_xGe$ presented in section 4.2.2. Similar to D22 the Q resolution of SANS-1 is dominated by the $\frac{\Delta\lambda}{\lambda} \approx 10$ % wavelength contribution. In Fig.4.13 the momentum transfer dependences of the scattering intensity $I(Q)$ are plotted. At low temperatures of about 10 K clear diffraction peaks of the helimagnetic spin structure are measured for the concentration $y = 0.0, 0.1, 0.2, 0.3, 0.4, 0.5, 0.7$ and 0.8. At the critical concentration $y_c \approx 0.6$, however, no Bragg peak is observed but instead a tail of diffuse scattering centred around $Q \to 0$, as it is expected for a not fully collinear ferromagnetic-like spin arrangement. The behaviour of the y dependence of the helix wave vector k_s, plotted in Fig.4.14, is qualitatively similar to the one observed in $Mn_{1-x}Fe_xGe$ (see Fig.4.6). In the Fe-rich part ($y \in [0.0 - 0.5]$) k_s decreases, from 0.09 nm^{-1} for pure FeGe to around zero at $y_c \approx 0.6$. Further raising of the Co-concentration results in an increase of the wavevector k_s to a maximum value of 0.14 nm^{-1} at $y = 0.8$. For $y_c \approx 0.6$ the wavevector k_s goes to zero, implying that the helimagnetic structure vanishes. The SQUID magnetisation measurement for this concentration evidenced, on the other hand, still a clear magnetic signal with an ordering temperature of $T_c \approx 130$ K, indicating strongly the transformation of the helical spin state into a ferromagnetic-like spin structure at the critical concentration y_c. According to the model by Bak-Jensen and Kataoka and co-workers

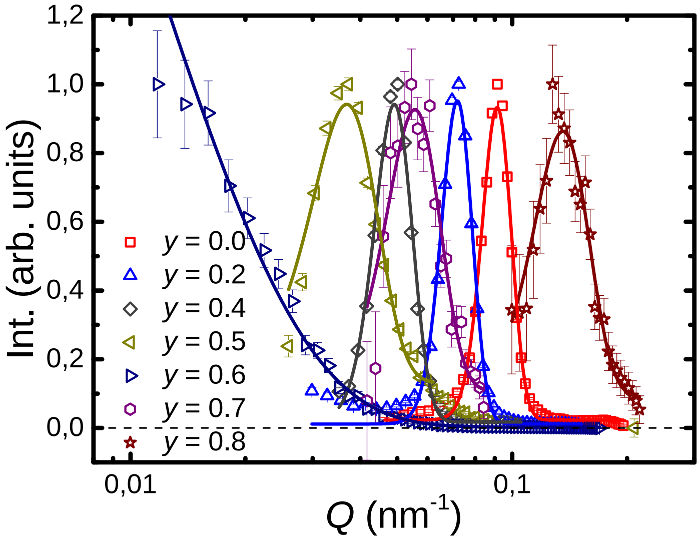

Figure 4.13: Momentum transfer dependence of the SANS intensity (normalised) at $T \approx 10$ K for compounds with $y = 0.0 - 0.8$. The lines are the Gaussian fits (figure is taken from [GSA+]).

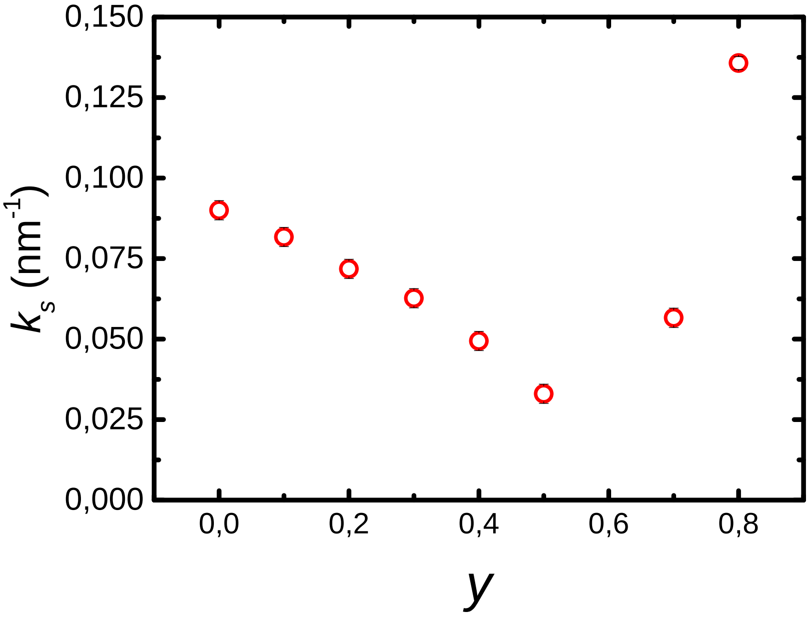

Figure 4.14: Dependence of the helix wavevector k_s on the concentration y of the $Fe_{1-y}Co_yGe$ compounds (figure taken from [GSA$^+$]).

(summarised in sections 1.2.2 and 1.2.3) a ferromagnetic-like structure would be realisable just in the case of a vanishing macroscopic DM constant D. The behaviour of the wavevector k_s can be interpreted as a change of the sign of $\boldsymbol{k}_s$, which would correspond to a change of the magnetic chirality at y_c analogous to the observations for $Mn_{1-x}Fe_xGe$ pointed out in the previous section. For FeGe a left-handed crystalline chirality is connected to a right-handed magnetic chirality as shown in section 4.2.3, while, according to the hypothesis given in [GPS$^+$b], for the Co-based compounds it should be opposite, a left-handed crystalline structure should go ahead with a left-handed magnetic spiral and vice versa. This hypothesis will be checked as soon as sufficient large single-crystalline samples for neutron scattering experiments will be available. As mentioned before, the difference in the energy between the ferromagnetic and the helical state can be measured by the critical field H_{c2} (see Eq.4.3), which is needed to transform the conical into the field aligned spin state. For this reason, it is of great interest to follow the evolution of the magnetic structure in the $Fe_{1-y}Co_yGe$ compounds under an applied magnetic field. An example how a horizontal oriented magnetic field affects the scattering for $y = 0.0$ is demonstrated in Fig.4.15 at $T \approx 10$ K. After zero field cooling, a field of 0.01 T is applied [Fig.4.15 (a)] and a ring-like pattern is observed, due to the randomly oriented spirals of the different crystallites. This picture is similar to the zero field measurements for $y = 0.1$ and $y = 0.5$ shown in Fig.4.12. The relative small field value of 0.01 T is not able to rotate the spiral spin structure into the field direction. Below H_{c1} the helix wavevector is fixed along the easy anisotropic axis of the cubic system. The intensity in the spots parallel to the field increases, due to the alignment of the spirals along the field direction. Starting from the first critical field H_{c1} one observes a reorientation from the multi-domain helical state to a single domain cone structure [Fig.4.15 (b)] oriented along the field direction, which is stable in the field range $H_{c1} < H < H_{c2}$ (see [BJ, Malb]). As discussed above, H_{c1} is a measure for strength of the anisotropic interactions, which aligns the helix wavevector along the principal axis of the system. The ring seen in (a) smoothly transforms into the spots laying on the field axis [Fig.4.15 (c)]. Reaching the second critical field H_{c2} the two spots disappear and just a diffuse scattering around $Q = 0$ remains, characteristic for the ferromagnetic field aligned state [Fig.4.15 (d)]. Both critical fields can be identified from the integrated intensities along the field direction illustrated in Figure 4.16. H_{c1} is determined as the field strength at which the integrated intensity starts growing, while H_{c2} is estimated as the cross point of the linear approximation of the determined curves

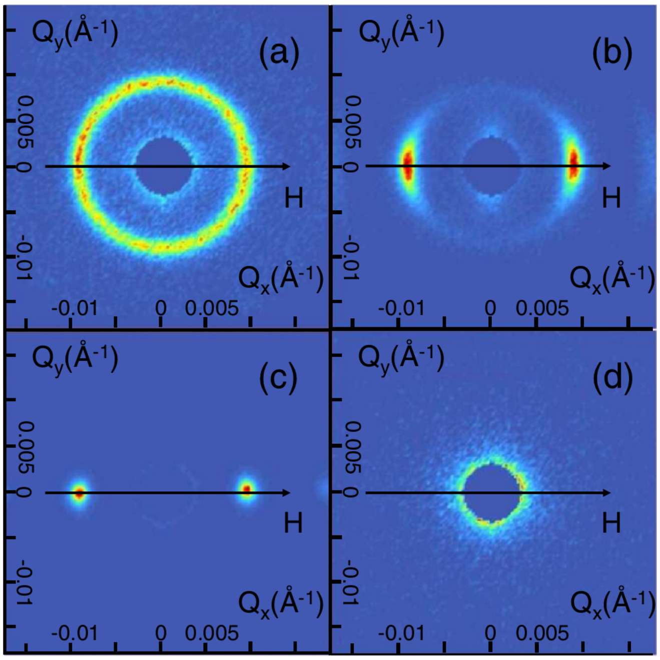

Figure 4.15: Small angle neutron scattering maps for the compound $y = 0.0$ and (a) $H = 0.01$ T, (b) $H = 0.1$ T, (c) $H = 0.25$ T and (d) $H = 0.5$ T at $T \approx 10$ K. The crossing points of the linear fits in the high temperature range with zero determine the value of H_{c2} for each concentration y. As example the critical fields H_{c1} and H_{c2} are given for $x = 0.1$ (figure taken from [GSA$^+$]).

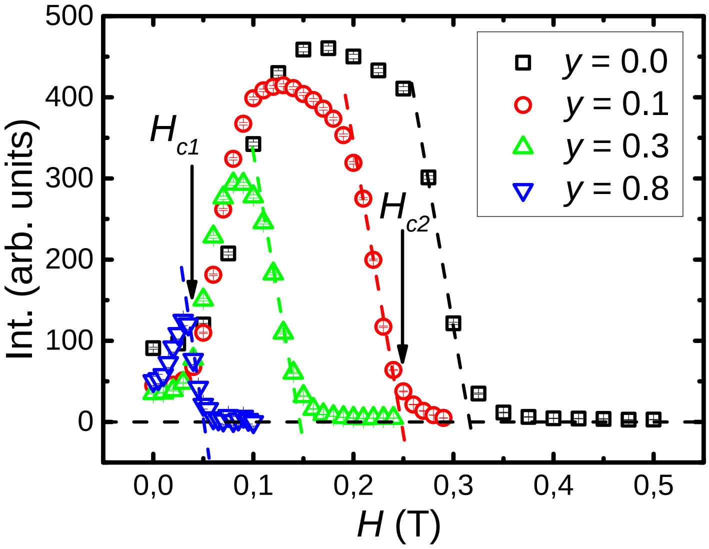

Figure 4.16: Magnetic field dependence of the integral intensity of the peak at $T = 10$ K for the compounds with $y = 0.0, 0.1, 0.3, 0.8$. The two critical fields H_{c1} and H_{c2} could be estimated from this curves as it is exemplified for $y = 0.3$. H_{c1} refers to the point at which the intensities in the two Bragg peaks along the field direction increases due to the alignment of the spirals along the field. H_{c2} is determined from the intersection of the linear approximation of the increasing intensity and the zero intensity line. This point corresponds to the field strength at which the spins are fully transformed from the conical structure to the ferromagnetic-like (figure taken from [GSA+]).

and the H axis as exemplary shown in Fig.4.16. With the method described here one can determine H_{c1}, which is the field at which the spirals start to align along the field, and H_{c2}, at which all spins are supposed to be field aligned. The critical fields H_{c1} and H_{c2} are plotted as function of the concentration y in Figure 4.17. It should be noted that both critical fields depend on the crystallographic orientation. Consequently, due to the powder nature of the investigated samples one can just determine an average over all possible directions in the crystal. As it could be seen in the $H - y$ phase diagram for $Fe_{1-y}Co_yGe$ in Fig.4.17, the values determined by the SANS measurements are in a good agreement with the ones from the SQUID measurements. H_{c1}, with the value of 0.03 T, stays approximately constant for all concentration y within the error bars. H_{c2}, on the other hand, manifests a behaviour similar to k_s. It decreases linear from $H_{c2} \approx 0.3$ T for $y = 0.0$ to $H_{c2} \rightarrow 0$ for $y_c = 0.6$ and slightly increases again for $x = 0.7$. Summarising the experimental

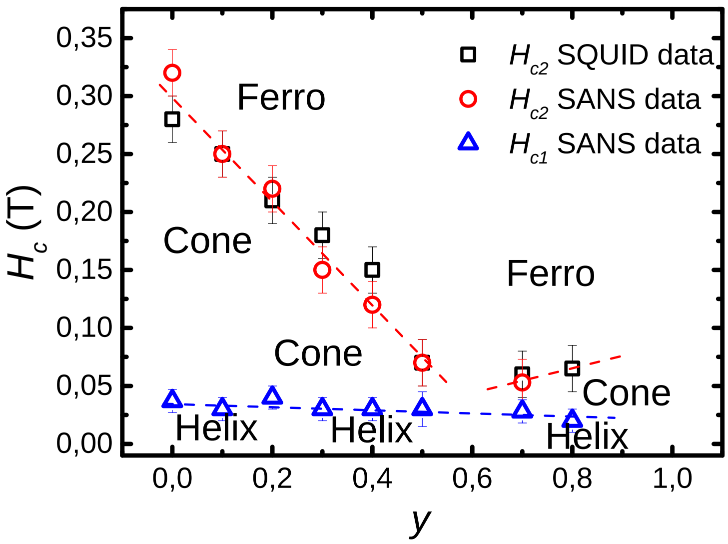

Figure 4.17: Dependence of the critical field H_{c1} and H_{c2} on the concentration y for the $Fe_{1-y}Co_yGe$ with $0.0 \leq y \leq 0.8$. (figure taken from [GSA+]).

findings from SQUID and SANS measurements Figure 4.17 can be interpreted as the following. In zero field the magnetic system is ordered in a plane spin helix. The helices transform into a conical spin state above H_{c1} and further to a field aligned spin state above H_{c2}. The three existing states, namely the helical, conical and ferromagnetic, are separated by the critical magnetic fields H_{c1} and H_{c2}. The experimental data suggest the transformation to a ferromagnetic ground state, when the energy difference between the ferromagnetic and helical state, measured by H_{c2}, becomes smaller than the energy of the anisotropy. This behaviour will be discussed in more detail in the following subsection.

4.3.3 Transformation from the spiral to the ferromagnetic state

The standard model to describe spin structure of cubic, non-centrosymmetric B20 compounds, given by Bak and Jensen [BJ] and Kataoka and co-workers [NYHK], was introduced in subsections 1.2.2 and 1.2.3, respectively. The helical spin structure is based on the hierarchy of the interactions: the ferromagnetic exchange J, the antisymmetric Dzyaloshinskii-Moriya interaction D and the anisotropic exchange interaction. Initially the cubic anisotropy was not included in this model. Kataoka and co-workers, however, already mentioned the importance of it [NYHK].

In the following chapter the essential role of the cubic anisotropy will be introduced based on the work of Maleyev and co-workers [GSM].
According to [BJ, NYHK], the ferromagnetic exchange interaction J and the DM interaction D are balanced in the value of the wavevector k_s (as given in Eq.4.2). Furthermore, the second critical field H_{c2} is a measure for the differences in the energies between the collinear ferromagnetic and the helical state (Eq.4.3). Therefore the experimental parameter set k_s, H_{c2} and S describes completely the magnetic system. Applying Eqs.4.2 and 4.3 to the experimental data given in Fig.4.11, 4.14

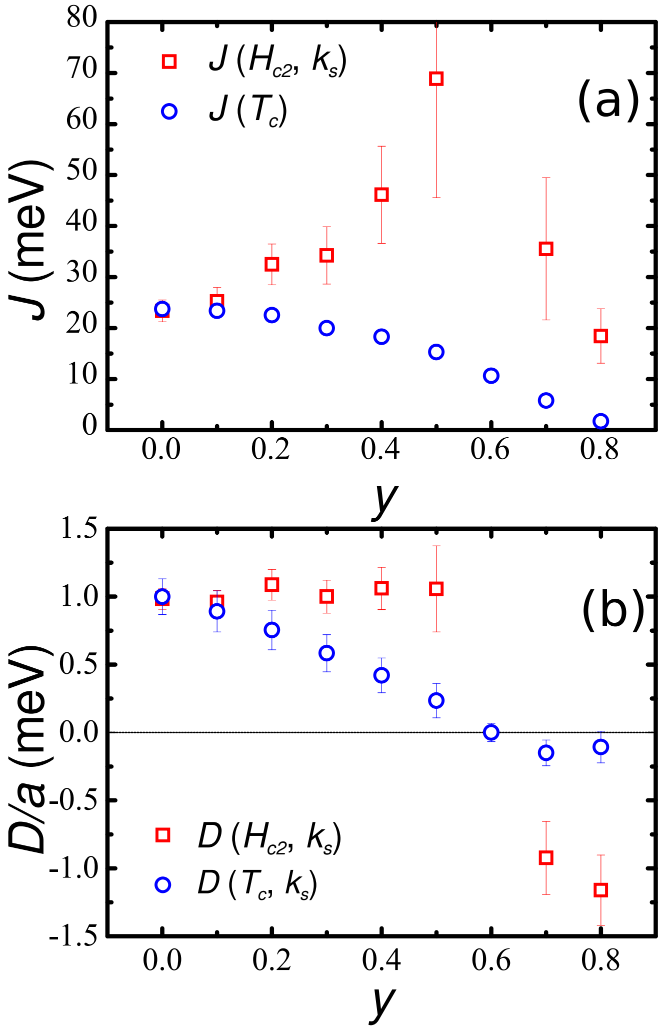

Figure 4.18: (a) Exchange constant J and (b) DM constant D estimated using the model ([BJ, NYHK]+ [Malb, BRP]) and using the model ([BJ, NYHK]+ [SYH$^+$]) in dependence on concentration y of $Fe_{1-y}Co_yGe$ (Reprinted figure with permission from [GSM], Copyright (2015) by the American Physical Society).

and 4.17 one can calculate the major driving interactions via $J = A/\left(Sa^2\right)$ and D/a. From the formula above it is obvious that J is determined by the critical field H_{c2} and k_s. In the following chapter the values for J and D, calculated from k_s and H_{c2}, will be named $J\left(H_{c2}, k_s\right)$ and $D\left(H_{c2}, k_s\right)$ to indicate their dependence of the H_{c2} and k_s. They are plotted in Fig.4.18. A divergent-like behaviour could be observed for J at $y \to 0.6$, related to k_s. The constant D, on the other hand, is nearly independent of y for $y < 0.6$ and changes its sign for $y > y_c$. The transition from the spiral to the ferromagnetic spin structure goes along with both parameters, k_s as well as H_{c2}, reaching zero. The DM constant $D\left(H_{c2}, k\right)$ does here not vanish, but exhibits a step-like behaviour, while the ferromagnetic exchange constant $J\left(H_{c2}, k\right)$ increases dramatically, this behaviour indicate the little physical meaning of both parameters at the critical point. Therefore, the model described by Eqs.4.2 and 4.3 seems to be inapplicable to the mixed $\mathrm{Fe}_{1-y}\mathrm{Co}_y\mathrm{Ge}$ compounds close to y_c.

Another approach was applied by Shibata and co-workers [SYH+]. They used the rough equality between the transition temperature $k_B T_c$ to J. Due the proportionality of the wavevector k_s to D/J one is able to recalculate the change of J and D with the concentration y. Therefore the value of $J\left(T_c\right)$ changes smoothly with y similar to the observed ordering temperature that is also dependent on y. The DM interaction constant $D\left(T_c, k_s\right)$ decreases slowly in this model for $y \leq 0.5$ and crosses zero around $y_c = 0.6$. The behaviour of the effective constant of $D\left(T_c, k_s\right)$ and $J\left(T_c\right)$ is consistent with the hypothesis on an average exchange constant for Fe and Co atoms in the mixed compounds. It is remarkable to mention that both models give the same values if applied to MnSi [GMO+]. In the limited case of small values of y, characterised by a second critical field H_{c2} that is much larger than the first critical field H_{c1}, both models work quite well. As pointed out above, the first critical field H_{c1} is a measure for the anisotropy in the system and H_{c2} for the helix energy, thus one can conclude that there is an influence of the anisotropy on the DM interaction upon formation of the spin helix. Maleyev and co-workers suggested certain modifications of Eq.4.2 to make the approach by Bak and Jensen [BJ] working in case of small k_s. The contribution of the Hamiltonian due to the cubic anisotropy can be written as:

$$H_{CA} = K \sum \{ (S^x_{\boldsymbol{R}})^4 + (S^y_{\boldsymbol{R}})^4 + (S^z_{\boldsymbol{R}})^4 \}. \tag{4.4}$$

In ferromagnets with $\boldsymbol{S}_{\boldsymbol{R}} = \boldsymbol{S}$ and a contribution of the cubic anisotropy to the classical energy term can be now expressed as:

$$E_{CA} = G \begin{cases} 1; \boldsymbol{S} \parallel (1,0,0), \\ 1/3; \boldsymbol{S} \parallel (1,1,1). \end{cases} \tag{4.5}$$

Here $G = KS^4$ and the extrema of E_{CA} are given in the right handed side of Eq.4.5. Two of the three possible axis in the cubic system, namely the $(1,1,1)$ and $(1,0,0)$ are therefore the easy axes for $K > 0$ and $K < 0$, respectively. As calculated in [Malb] the (1,1,0) direction is not possible. As derived in detail in Appendix C (Eqs.C.9 - C.13) the expression for the helix energy taking the cubic anisotropy into account is:

$$\begin{aligned} E = &- \frac{SAk_s^2}{2}\left(1 - \sin^2\alpha\right) + \frac{G}{8}[(3-5C)\left(-7\sin^4\alpha + 6\sin^2\alpha + 1\right) + 8C] \\ &- SH_{\|}\sin\alpha. \end{aligned} \tag{4.6}$$

In zero magnetic field the energy term (Eq.C.13) is minimal for a planar helix ($\alpha = 0$) and $\hat{c} \,||\, (1,1,1)$ for $G > 0$. The helix exists if the helix energy $E = -SAk^2/2 + G/2$ is smaller than the anisotropic energy $G/3$ of the ferromagnetic state. The corresponding conditions are derived by Maleyev and co-workers as:

$$SAk^2 > G/3. \tag{4.7}$$

If the condition above is not fulfilled, the helix is unstable and a ferromagnetic state is energetically favoured. If $G < 0$ the spiral points along the $(1,0,0)$ axis and one get the following condition for the stability of the helical state:

$$SAk^2 > |G|/2. \tag{4.8}$$

The first critical field H_{c1} (depending on the anisotropy G and the ratio of the DM interaction and the cubic anisotropy $r = SAk_s^2/12G$ (for $G > 0$) and $r = SAk_s^2/8|G|$ (for $G < 0$) is given by (see Appendix C for a detailed derivation):

$$H_{c1} = \frac{G}{S}\sin\alpha_{c1}\left(7\sin^2\alpha_{c1} + 12r - 3\right), \quad r > \sqrt{\frac{1}{30}} \tag{4.9}$$

where α_{c1} is the first critical angle. The first critical magnetic field H_{c1} is thus strongly dependent on the angle between the applied magnetic field and the easy axis with a minimum when both directions coincide. The first critical magnetic field is obviously so much less the closer orientation of the magnetic field is to the easy axis. The second critical field H_{c2} (see also Appendix C for a detailed derivation) is given for $G > 0$ by:

$$H_{c2} = Ak_s^2 + \frac{9}{16}\frac{G}{S}, \quad G > 0. \tag{4.10}$$

and for $G < 0$:

$$H_{c2} = Ak_s^2 - \frac{9}{16}\frac{|G|}{S}, \quad G < 0. \tag{4.11}$$

A detailed consideration of the influence of the cubic anisotropy can be found in Appendix C according to [GSM].

4.3.4 Discussion

In summary of the results for the solid solutions of $\mathrm{Fe}_{1-y}\mathrm{Co}_y\mathrm{Ge}$, a transformation from the helical to the ferromagnetic spin structure at $y \to y_c$ has been observed. This transformation results from the different signs of the Dzyaloshinskii-Moriya interaction and the different helix chiralities related to the different magnetic atoms (Co and Fe). Due to the lack of sufficiently big single crystals for polarised neutron studies it was not possible to determine the chiral link between structural and magnetic chirality for the samples with a concentration $x > 0.0$. At the critical concentration the DM constant effectively vanished, while the isotropic, ferromagnetic exchange constant J is positive and finite, i.e. the transformation occurs when H_{c2} becomes comparable to H_{c1}. Furthermore, the competition between the cubic anisotropy and the ferromagnetic exchange could be identified as the mechanism responsible for the transformation from the spiral to the ferromagnetic spin structure. The important role of the cubic anisotropy, in the case of small k_s was already noticed in [NYHK], but is not included in the commonly used phenomenological model by Bak-Jensen [BJ]. Without the cubic anisotropy the model of Bak-Jensen does not impose any limitation for the value of the helical wavevector k_s as well as for the second critical field H_{c2}. Both parameters can become infinitely small. The anisotropic exchange energy, as part of the exchange interaction, cannot provide such a limitation, whereas the cubic anisotropy can limit the stability of the helical phase in the region of small k_s [Eqs.4.7 and 4.8] and in addition, makes a contribution to the value of the second critical field H_{c2} [Eqs.4.10 and 4.11]. Of certain importance is, moreover, the dependence of the critical fields on the orientation of the magnetic field dependent on the position relative to the crystalline axis due the influence of the cubic anisotropy [Eqs.4.10 and 4.11]. The critical field decreases (increases) depending if the energy of the cubic anisotropy is positive (negative). Besides, it has been revealed that if a possible weakening of the DM interaction takes place, a first-order transition from the spiral to the ferromagnetic spin arrangement can occur (for certain orientation of the magnetic field) and the corresponding critical cone angle for this case [Eq.C.22] was determined by Maleyev and co-workers [GSM].

In general, the experimental and theoretical proof for the possible existence of a ferromagnetic phase in non-centrosymmetric cubic magnets with Dzyaloshinskii-Moriya interaction has been given.

4.4 $\mathbf{Fe_{1-z}Co_zSi}$

In the previous sections the transition of the spiral wave vector $k_s = 2\pi/d$ to zero has been shown at a certain critical concentrations x_c, y_c for two kinds of germanide based powder compounds: $Mn_{1-x}Fe_xGe$ [GPS+b, SYH+] and $Fe_{1-y}Co_yGe$ [GSM]. The monotonic behaviour of the wavevector k_s indicating that the DM interaction goes to zero at a certain critical concentration, supports the hypothesis that the effective macroscopic DM constant D changes its sign as a function of x, y. These findings have been considered under the existence of a sign change of the effective macroscopic constant of the DM interaction depending on the $3d$ element occupying metal site. In this section the question is addressed in the case of the solid solutions $Fe_{1-z}Co_zSi$ [SAC+], which manifest chiral magnetic ordering in a certain concentration range. Contrary to the germanides, one is able to grow these silicide based compounds as single crystals of the size of several 100 microns, together with close to 100% control of the structural chirality in the growth process [DGM+]. The large sample size makes it possible to determine the structural chirality Γ_c and furthermore, the magnetic chirality γ_m by resonant x-ray diffraction (introduced in subsection 3.3.2) and polarised neutron scattering (shown in subsection 2.3.3). In consequence, these compounds offer the possibility to directly follow the product of $\Gamma_c \times \gamma_m$ in the whole magnetic ordered range z, as it was not feasible before.
Single crystalline $Fe_{1-z}Co_zSi$ solid solution with z running from 0.5 to 0.8 have been synthesised using the Tri-Arc-Czochralski method [see subsection 3.2.1]. As stated in section 3.3.2, the single crystal x-ray diffraction measurements allow the determination of the absolute crystal structure and due to the possible determination of the Flack parameter the ratio of domains with different handedness. The data for all samples are in good agreement with the structural $P2_13$ model as indicated by the low R-factor (see Tab.3.1). The unit cell dimensions follow the Vegards law, but the atomic positions remain nearly unchanged as a function of the composition and define thus the absolute crystalline structure (see Tab.3.1). Using the previous definition (Refs. [TTIE, GCD+a]) of the structure according to the metal sub-lattice with $u_{\mathrm{Me}} \approx 0.86$ is set to be right-handed ($\Gamma_c = +1$). All investigated samples show the same structural chirality as summarised in Table 3.1, as it is expected due to the chosen seed crystals for the growth process.

4.4.1 Magnetisation measurements: SQUID

Analogous to the previous sections on the $Mn_{1-x}Fe_xGe$ and $Fe_{1-y}Co_yGe$ compounds, the same SQUID-magnetometer Quantum Design MPMS-5S (see Appendix A.2 for details) has been used to carry out magnetic measurements on the synthesised $Fe_{1-z}Co_zSi$ samples. Beille and co-workers gave the experimental evidence for the magnetic order of $Fe_{1-z}Co_zSi$ in the broad doping range between $0.05 \leq z \leq 0.8$ [BVT+, BVR]. The temperature scans of the magnetisation for

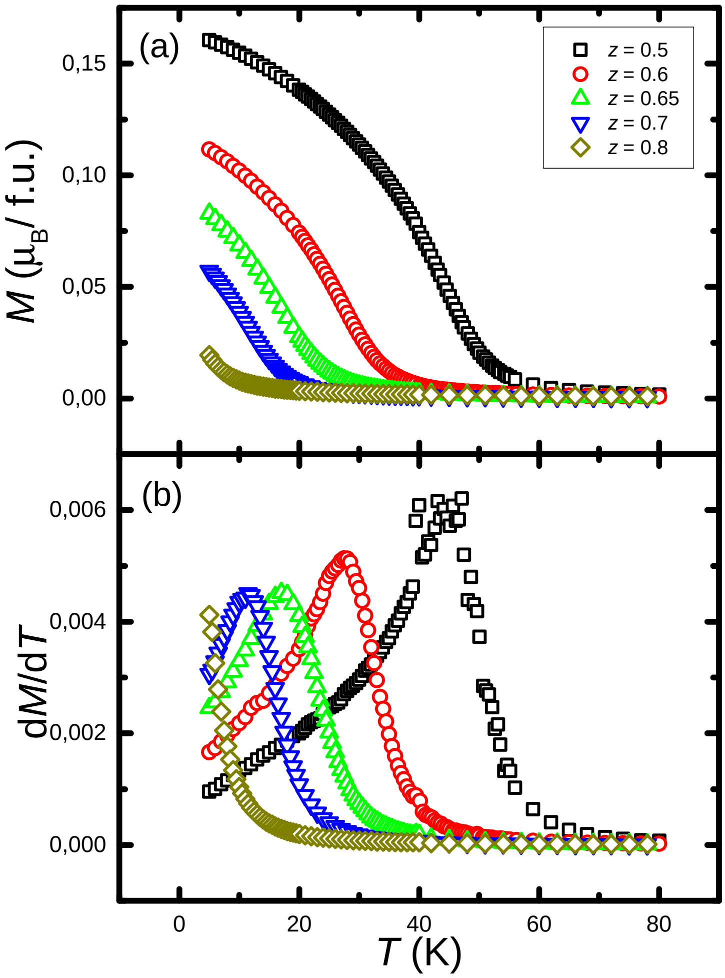

Figure 4.19: (a) The temperature dependence of the magnetisation M for $Fe_{1-z}Co_zSi$ compounds with $z = 0.5 - 0.8$ at $H = 100$ mT. (b) The first derivative of the magnetisation on the temperature dM/dT (figure taken from [SAC+]).

the different compounds are presented in Figure 4.19 (a). The measurements have been carried out in a field of $H = 100$ mT, and thus, above H_{c2} for all investigated compounds, ergo, in the field aligned spin state. Similar to the previous compounds the position of the maxima of the derivation dM/dT as given in Fig.4.19 (b) has been used to determine the ordering temperatures T_c. For the concentrations $z = 0.1 - 0.5$ the same procedure has been applied by Grigoriev and co-workers [GCD+a]. The ordering temperatures of the whole concentration range $z = 0.1 - 0.7$ is summarised in Fig.4.20. T_c increases monotonically with increasing Co-concentration z from 0.1 to 0.4, and decreases again monotonically for $z > 0.4$ with reaching zero at approximately $z = 0.8$. Therefore, all studied compounds are magnetically ordered till $z = 0.7$ (in the accessible temperature range by SQUID, which is down to $T = 5K$).

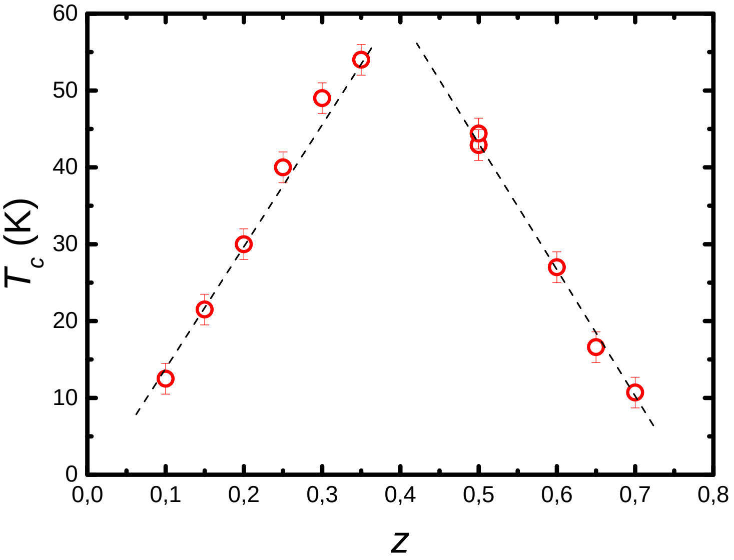

Figure 4.20: Dependence of the critical temperature T_c on the concentration z of $Fe_{1-z}Co_zSi$ compounds. The dashed lines are guides for the eyes (figure taken from [SAC+]).

4.4.2 Investigation of the helical phase: polarised SANS

The single crystalline nature of the samples allows the direct determination of the magnetic chirality by using polarised neutron diffraction [MBS, Blu] analogous to MnSi and FeGe presented in section 4.2.3. The data analysis has been performed analogous to section 4.2.3 and [GCD+a, GPS+b]. The experiments were carried out at the SANS-1 instrument at the Maier-Leibnitz-Zentrum (see Appendix A.3 for details), the wavelength of the neutron beam was varied in a range from 0.6 nm and 1.2 nm depending on the required Q range. A position sensitive detector with 128×128 pixels and a pixel size of 8 mm was used to record the two dimensional scattered intensity contribution. These settings allow to cover a Q range from 0.02 nm^{-1} to 1 nm^{-1}. The initial degree of polarisation of the incident neutron

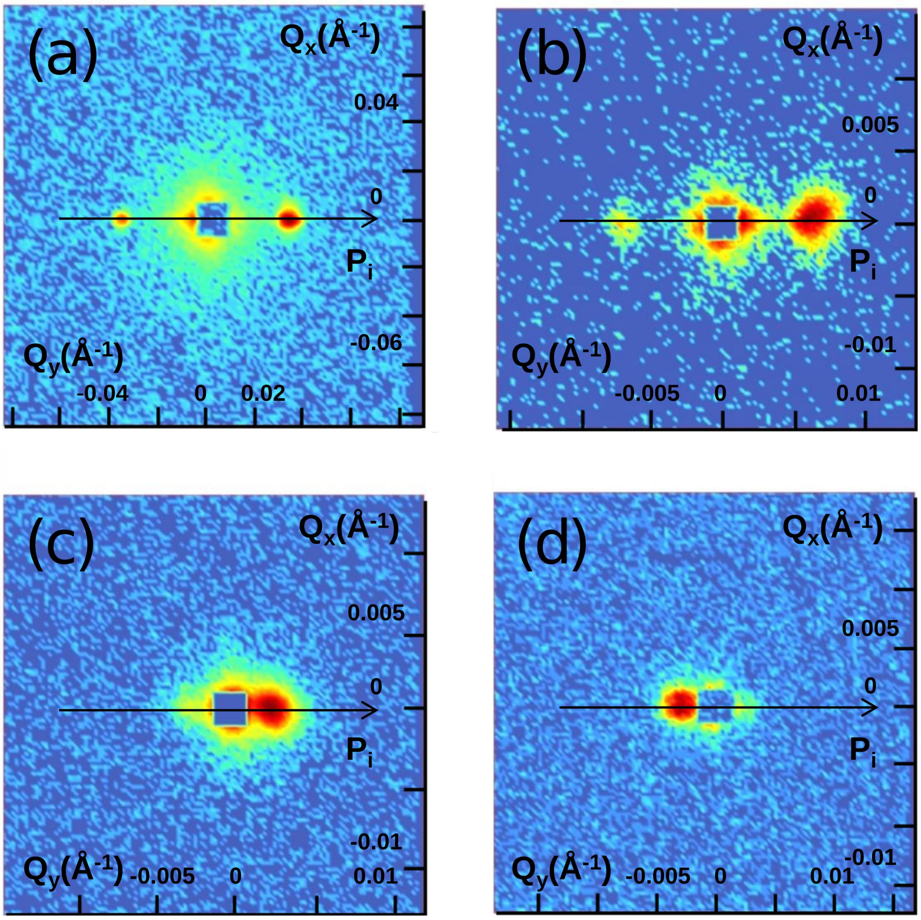

Figure 4.21: Maps of polarised SANS intensities of MnSi (a) and of Fe$_{1-z}$Co$_z$Si with $z = 0.5$ (b), 0.6 (c), 0.7 (d) for polarisation $+\boldsymbol{P}_i$ along the guide field at $T \approx 3.5$ K (figure taken from [SAC+]).

beam was $P_0 \approx 0.9$. Similar to the previous section, the well studied MnSi has

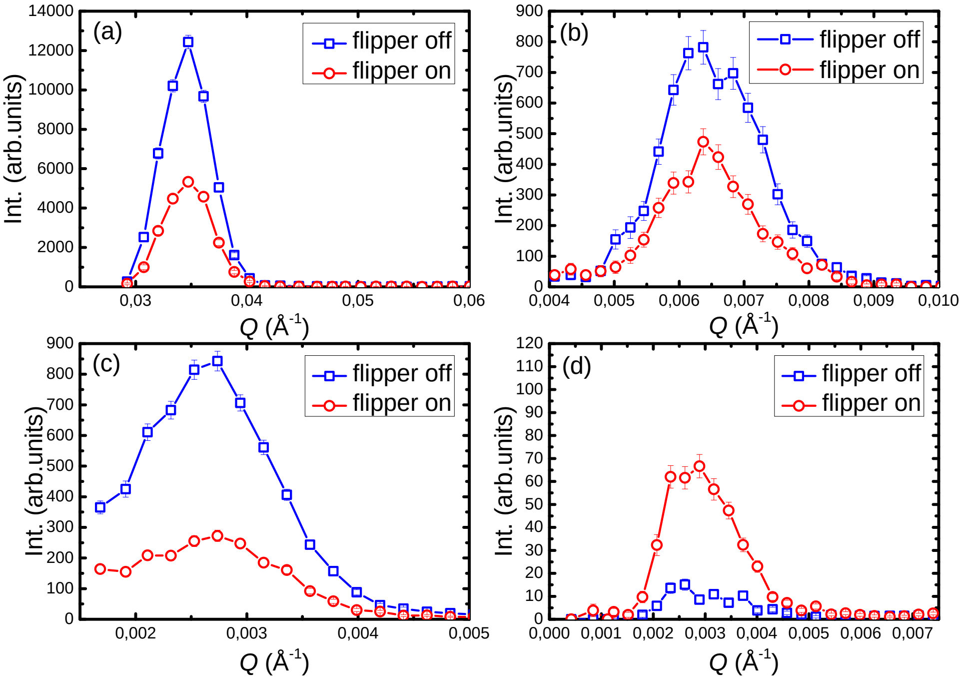

Figure 4.22: The integrated intensities of MnSi (a) and of Fe$_{1-z}$Co$_z$Si with $z = 0.5$ (b), 0.6 (c), 0.7 (d) for the right Bragg peak (polarisation $+\boldsymbol{P}_i$ along/opposite the guide field at $T \approx 3.5$K).

been used as a reference sample[5]. The polarised small angle neutron scattering maps for the compound MnSi and Fe$_{1-z}$Co$_z$Si with $z = 0.5$, 0.6 and 0.7 measured at approximate 3.5 K and are presented in Fig.4.21 for the polarisation along the magnetic field. The corresponding integrated intensities for the right magnetic Bragg peak with the polarisation along the magnetic field direction is presented in Fig.4.22. For all investigated Fe$_{1-z}$Co$_z$Si compounds one can determine the lower limit of the correlation length as 600 nm, using the peak width. It should be noticed that the width is mainly determined by the low wavelength resolution of $\frac{\Delta\lambda}{\lambda} \approx 10\%$ and the real size of the homochiral, helimagnetic domains is assumed to be significant larger. MnSi has a maximum of the scattering intensity at the right part of the detector for the polarisation along the field direction as it could be seen in Fig.4.21 (a). The associated integrated intensity is plotted in Fig.4.22 (a). In agreement with the previously obtained results for MnSi [TTIE, GCD$^+$a, GPS$^+$b]

---

[5] It is remarkable to mention that the reference sample is just necessary to determine the absolute sign value.

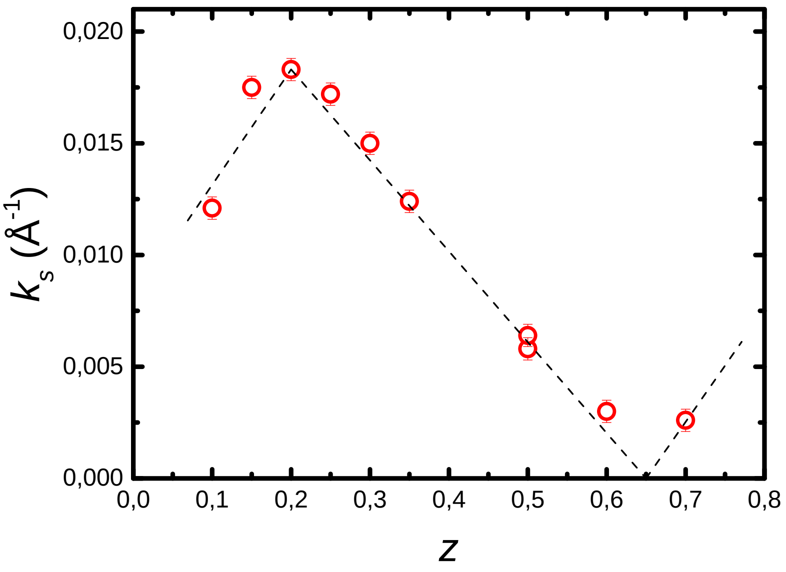

Figure 4.23: Dependence of the helix wavevector $|\boldsymbol{k}_s|$ on the concentration z of the $\mathrm{Fe}_{1-z}\mathrm{Co}_z\mathrm{Si}$ compounds (figure taken from [SAC+]).

the magnetic chirality for this configuration is γ_m = -1, i.e. the magnetic structure is left-handed. Since the integrated intensities from the polarised SANS maps for $\mathrm{Fe}_{0.5}\mathrm{Co}_{0.5}\mathrm{Si}$ and $\mathrm{Fe}_{0.4}\mathrm{Co}_{0.6}\mathrm{Si}$ looks similar [Figs.4.21, 4.22 (b,c)], it can be concluded that also the magnetic chirality is the same. The $\mathrm{Fe}_{0.3}\mathrm{Co}_{0.7}\mathrm{Si}$ sample, on the other hand, shows the opposite behaviour [Figs.4.21, 4.22 (d)] with $\gamma_m = +1$, and thus, possess a right-handed spiral spin structure. The analogous measurements have been done for the opposite polarisation, confirming the here presented results (see Appendix D). Besides, the magnetic chirality, the helix wavevector $|\boldsymbol{k}_s|$ can be determined from the scattering maps at $T \approx 3.5$ K. Figure 4.23 (a) illustrates the z dependence of $|\boldsymbol{k}_s|$ for $z = 0.1 - 0.7$ [GCD+a, SAC+]. The value of

Table 4.2: Crystal chirality Γ_c and magnetic chirality γ_m of the compounds with $P2_13$ structure (+1) and (-1) corresponds to the right and left chirality, respectively [TTIE, GCD+a, GPS+b, SAC+].

Compound	$\Gamma_c \to \gamma_m$	$\Gamma_c \times \gamma_m$
MnSi	$+1(-1) \to +1(-1)$	$+1$
$\mathrm{Fe}_{0.5}\mathrm{Co}_{0.5}\mathrm{Si}$	$+1 \to -1$	-1
$\mathrm{Fe}_{0.4}\mathrm{Co}_{0.6}\mathrm{Si}$	$+1 \to -1$	-1
$\mathrm{Fe}_{0.3}\mathrm{Co}_{0.7}\mathrm{Si}$	$+1 \to +1$	$+1$

the wavevector increases from $|\boldsymbol{k}_s| = 0.121\ \mathrm{nm}^{-1}$ at $z = 0.1$ to its maximum value of $|\boldsymbol{k}_s| = 0.185\ \mathrm{nm}^{-1}$ at $z = 0.2$. With further increasing of z above 0.2 the value of $|\boldsymbol{k}_s|$ decreases quasi linearly until it reaches zero at the critical concentration of $z_c \approx 0.65$, while thereafter it increases again to $|\boldsymbol{k}_s| = 0.026\ \mathrm{nm}^{-1}$ for the highest Co-concentration of $z = 0.7$. As already discusses earlier, the helix wavevector is linked to the Dzyaloshinskii constant D via Eq.4.1. Since the spinwave stiffness A and the spin value S are expected to be monotonic functions of the Co content [MSD+, GMD+a], the vanishing $|\boldsymbol{k}_s|$ value implies that also the macroscopic DM constant becomes zero, at the critical concentration z_c. The availability of the sufficiently large single crystals in the case of $\mathrm{Fe}_{1-z}\mathrm{Co}_z\mathrm{Si}$ allows the direct demonstration of the separation in two regions with different signs of the DM constant D at the critical concentration z_c, while the crystalline chirality remains the same.

4.4.3 Discussion

In summary the results obtained for $\mathrm{Fe}_{1-z}\mathrm{Co}_z\mathrm{Si}$ reveal that the chiral magneto-lattice coupling, i.e. the link between structural and magnetic chirality, mapped phenomenologically as the DM, could be applied to control the magnetic chirality. The product $\mathrm{sgn}(D) \times \Gamma_c \times \gamma_m$ is an invariant with respect to inversion and time-reversal operations ensuring that left-handed and right-handed polymorphs have the same energy. The sign of the Dzyaloshinskii constant D, controlling the magnetic chirality, depends on the $3d$-element occupying the metal site in $\mathrm{Fe}_{1-z}\mathrm{Co}_z\mathrm{Si}$, and as extensively discussed in section 4.2 and 4.3 in monogermanides [GPS+b, SYH+, GSA+, SAC+]. For the single crystalline $\mathrm{Fe}_{1-z}\mathrm{Co}_z\mathrm{Si}$ it was for the first time possible, to directly follow the change of the product of the structurally chirality and the magnetic chirality $\Gamma_c \times \gamma_m$ in the whole magnetic ordered range, measuring the flip of the chiral link between structure and magnetism in $\mathrm{Fe}_{1-z}\mathrm{Co}_z\mathrm{Si}$. It seems likely that the dynamic of the $d_{x^2-y^2}$-like states of the transition metal is the responsible mechanism for the observed behaviour. As calculated by Gayles and co-workers for $\mathrm{Mn}_{1-x}\mathrm{Fe}_x\mathrm{Ge}$, with increasing x (change of the carrier density) the $d_{x^2-y^2}$ states move from above to below the Fermi level, become occupied, and enter the d_{xy} state with the opposite spin (see section 4.2.4). It is very likely that the observed change of the sign of D is based on a similar mechanism. Moreover, the transition from the spiral spin to the ferromagnetic spin structure at a critical concentration $z \to z_c$, in zero magnetic field, has also been discovered in a monosilicide based compound. The obtained results allow the conclusion that the cubic anisotropy plays the same important role in the range of small helix wavevector $|\boldsymbol{k}_s|$ as for the monogermanides (see section 4.3.3). The products of the lattice chirality Γ_c and the magnetic chirality γ_m as function of the concentration z are given in Figure 4.24. The lattice chirality has the same sign for all considered samples, while the magnetic chirality has an opposite sign

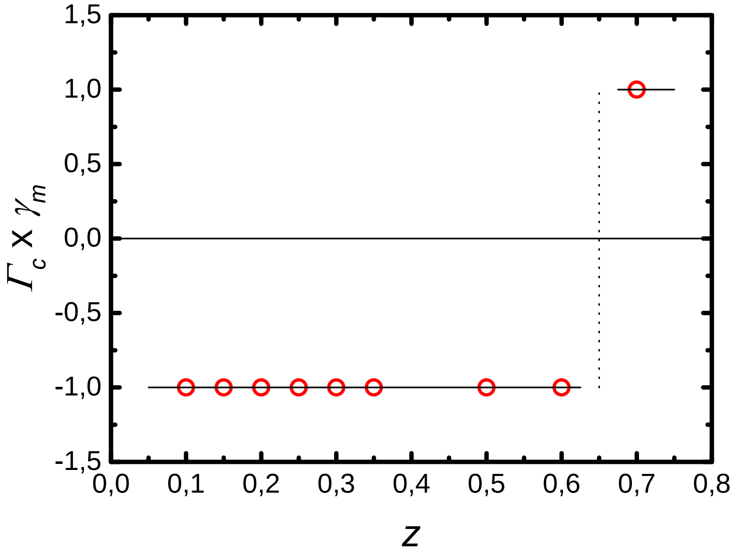

Figure 4.24: Dependence of the product of structural and magnetic chiralities $\Gamma_c \times \gamma_m$ on the concentration z, the lines are guides for the eyes (figure taken from [SAC$^+$]).

for $z < z_c$ and $z > z_c$.

Chapter 5

Conclusion and Outlook

The cubic B20 compounds have a non-centrosymmetric crystallographic structure described by the P$2_1$3 space group. The lack of a symmetry center for the crystalline structure produces the chiral Dzyaloshinskii-Moriya interaction [Dzyb,Mor]. The appearance of the DM interaction results in the spiral spin arrangement. Previous investigation assumed that the spin helix exists in a certain chirality γ_m, rigorously determined by the structural chirality Γ_c via the sign of the DM interaction [TTIE, IEM+, GCD+a, GCD+b, DGM+, MSK+]. However, it was known from former investigations that the crystalline Γ_c and magnetic chirality γ_m have the same sense for the Mn-based compounds ($\mathrm{Mn}_{1-x}\mathrm{Fe}_x\mathrm{Si}$ and $\mathrm{Mn}_{1-x}\mathrm{Co}_x\mathrm{Si}$), while for the Fe based compounds these two chiralities are opposite to each other ($\mathrm{Fe}_{1-z}\mathrm{Co}_z\mathrm{Si}$ at $z \leq 0.5$). It is obvious that the magnetic chirality is not strictly following the structural chirality and that their link may dependent on the contributing sites of the individual compounds. Hence, it is of great interest to follow the change of the link between the structural and magnetic chiralities by varying the concentration ratio between the different contributing $3d$ transition metal sides. Unfortunately, for $\mathrm{Mn}_{1-x}\mathrm{Fe}_x\mathrm{Si}$ this is just possible in a very limited range, because of the narrow ordered range of $x \in [0.0 - 0.17]$. In the framework of this thesis the evolution of the chiral magnetic structure in the two monogermanide based compounds $\mathrm{Mn}_{1-x}\mathrm{Fe}_x\mathrm{Ge}$ and $\mathrm{Fe}_{1-y}\mathrm{Co}_y\mathrm{Ge}$, as well as in the Si based compound $\mathrm{Fe}_{1-z}\mathrm{Co}_z\mathrm{Si}$ for $z \geq 0.5$ have been investigated and correlated to their structural chirality for the first time. The results of this work have been prepublished in [GPS+b], [GSA+] and [SAC+], respectively. SQUID magnetisation measurements have been used to determine the macroscopic magnetic order, while the crystallographic chirality Γ_c and the magnetic chirality γ_m of the investigated compounds have been determined via combined x-ray diffraction [Fla,FB,SSF] and polarised small angle neutron scattering [MBS, Blu]. Three of the most brilliant x-ray and neutron sources, i.e. ESRF (Grenoble, France), the MLZ (Garching, Germany) and the ILL (Grenoble, France), have been used for the performed ex-

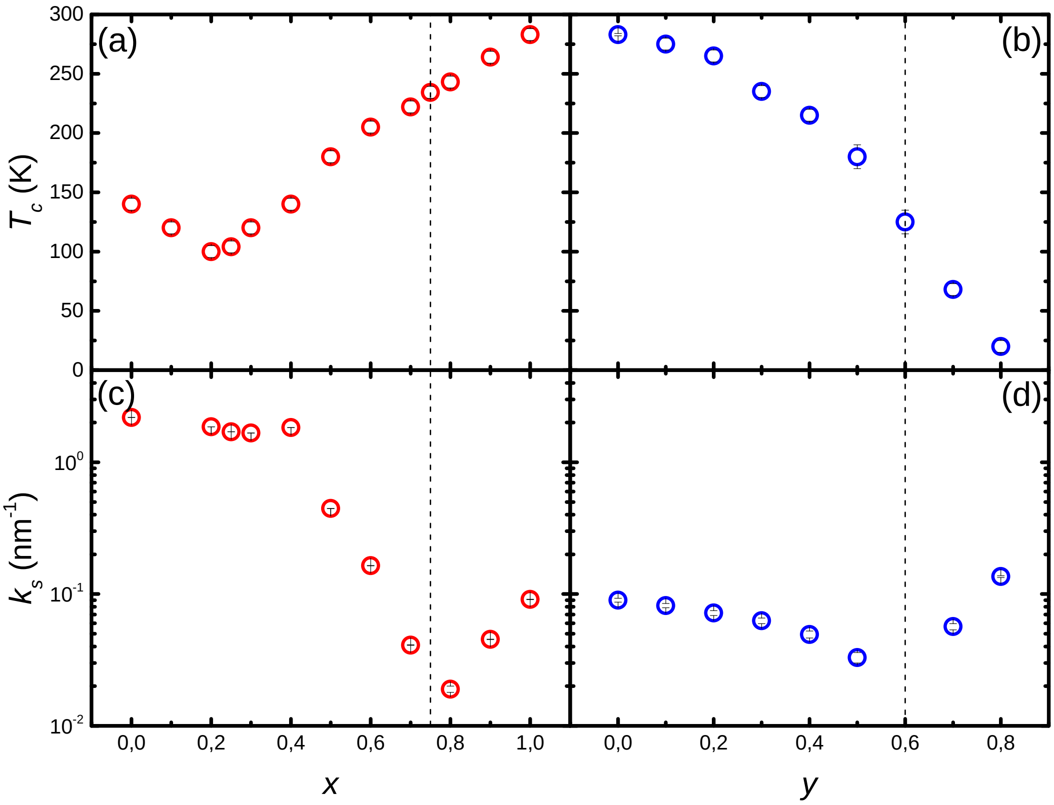

Figure 5.1: Dependence of the critical temperature T_c (a,b) and the helix wavevector k_s (c,d) on x and y for $\mathrm{Mn}_{1-x}\mathrm{Fe}_x\mathrm{Ge}$ and $\mathrm{Fe}_{1-y}\mathrm{Co}_y\mathrm{Ge}$, respectively (the critical concentrations x_c and y_c are marked by the dashed lines) [GPS⁺b, GSA⁺].

periments. In the framework of this work several significant new findings have been obtained: the ability of controlling the size of the magnetic structure is for practical reasons of great interest for future applications as for e. g. the Racetrack memory that is mentioned in the introduction. The measurements, summarised in Figs.5.1 and 5.2, reveal the feasibility to tune the size of the helix wavevector in the order of two magnitudes, from $|\boldsymbol{k}_s| = 2.2\ \mathrm{nm}^{-1}$ for pure MnGe down to $|\boldsymbol{k}_s| = 0.02\ \mathrm{nm}^{-1}$ for $\mathrm{Mn}_{0.2}\mathrm{Fe}_{0.8}\mathrm{Ge}$, along with a variation of the magnetic ordering temperature up to a maximum of approximate 280 K for pure FeGe. This corresponds to a range of the helix length between approximately 3 nm and 300 nm. In addition, it has been experimentally revealed that a transformation from the helix to a ferromagnetic structure occurs at the critical concentrations x_c, y_c, z_c for $\mathrm{Mn}_{1-x}\mathrm{Fe}_x\mathrm{Ge}$ [GPS⁺b], $\mathrm{Fe}_{1-y}\mathrm{Co}_y\mathrm{Ge}$ [GSA⁺], and $\mathrm{Fe}_{1-z}\mathrm{Co}_z\mathrm{Si}$ [SAC⁺]. These transformations can be interpreted as effect of the different signs of the Dzyaloshinskii-Moriya interaction and consequently, resulting different helix chiralities, related to the different magnetic

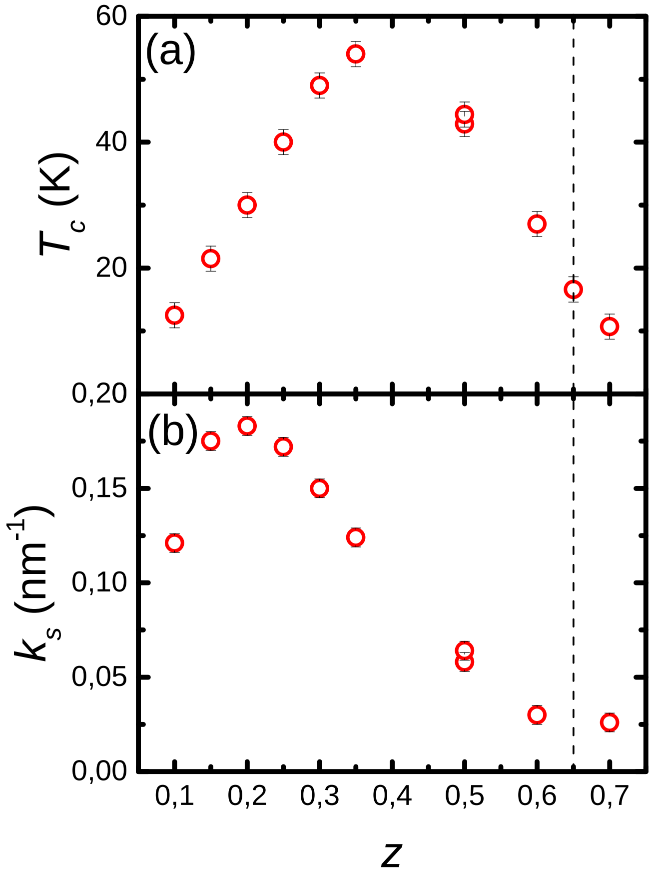

Figure 5.2: Dependence of the critical temperature T_c (a) and the helix wavevector k_s (b) on z for $Fe_{1-z}Co_zSi$ (the critical concentration z_c is marked by the dashed line) [SAC+].

atoms Mn/Co and Fe. Thus, within this work the flip of the chiral link between structural and magnetic chirality has been discovered as generic new property of transition metal monosilicides and -germanides.
After the presentation of the results obtained within this thesis at the Flipper-2013 workshop [GPS+a], showing the flip of the chiral link between structure and magnetism in the helical phase of $Mn_{1-x}Fe_xGe$, Shibata and co-workers were able to find a similar effect for the chiral link within the so-called *skyrmion* structure in the *A-phase* in $Mn_{1-x}Fe_xGe$ using Lorentz microscopy [SYH+]. The subsequently findings of Shibata and co-workers are consistent with the results obtained in the framework of this thesis. Recent Monte-Carlo simulation [CXYL] as well as density functional theory calculations [GFS+,KNA] were able to reproduce the experimen-

tal results theoretically. The dynamic of the $d_{x^2-y^2}$ states, moving from above the Fermi level to below, with the change of the concentration x (due the change of the carrier density) has been determined as driving mechanism for the change of the sign of D. The magnetic phase diagram of the cubic B20 helimagnets is interpreted in the frame of the widely used phenomenological model of Bak and Jensen [BJ], that is based on the hierarchy of the ferromagnetic exchange interaction, the antisymmetric Dzyaloshinskii-Moriya interaction and the anisotropic exchange interaction. The anisotropic exchange energy, as part of the exchange interaction, cannot limit the values of k_s and H_{c2}, therefore both values could become infinitely small. Consequently, the transformation from the spiral structure to the ferromagnetic one, in absence of a magnetic field, cannot be described in the framework of the Bak-Jensen model. Based on the experimental results of this work the important role of the cubic anisotropy was introduced. It competes with the Dzyaloshinskii-Moriya interaction in the case of small k_s, that may lead to a ferromagnetic state in a cubic B20 compound with DM interaction [GSM].
Maleyev and co-workers [GSM] predicted a concentration range close to the critical concentrations, where the second H_{c2} becomes comparable with the first critical field H_{c1}. This seems to be recognisable in the slightly different critical concentrations of $Fe_{1-y}Co_yGe$ ($y_c \approx 0.6$) and $Fe_{1-z}Co_zSi$ ($z_c \approx 0.65$), both concentrations could be examples of a broader critical concentration range. A more detailed sampling near the critical concentration could clarify the borders of this range. Additional field dependent measurements for the two compounds $Mn_{1-x}Fe_xGe$ and $Fe_{1-z}Co_zSi$ will help to prove the behaviour of the two critical fields close to x_c and z_c. The first critical field H_{c1} is related to the anisotropy and the second critical field H_{c2} is related to the helix energy, as soon as these two fields become comparable, the competition between the cubic anisotropy and the DM interaction becomes well noticeable and destabilises the helix spin structure. The hypothesis that Mn and Co based monogermanide/-silicide compounds have the same sense of chirality, opposite to the Fe based compounds, will be tested by investigating the mixed $Mn_{1-x}Co_xGe$ compounds in the nearest future.
This work further exploits the idea to control the sign of the DM in the monosilicide series $Fe_{1-z}Co_zSi$ by the controlled change of the $3d$ element concentration. The single crystalline nature of these compounds offers the opportunity to grow crystals with a nearly 100 % controlled structural chirality by using the Czochralski method [DGM+]. It reveals the ability to produce samples with fully controlled structural and magnetic chirality, this is a key for crystal engineer of customised novel spintronic application, exploiting the chirality of the magnetic structure for information storage.

Appendix A

Instruments

A.1 PILATUS@SNBL

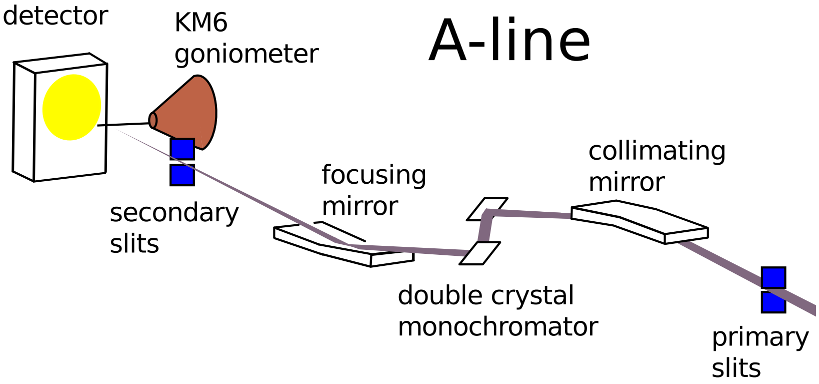

Figure A.1: Schematic layout of the Swiss-Norwegian beamline A (figure taken from [ESR]).

The powder and single crystal x-ray diffraction experiments have been performed using the PILATUS@SNBL diffractometer [DPDC] at the Bending Magnet beamline 1A (BM01A) at the Swiss Norwegian Beam Line (SNBL) [schematically shown in Fig.A.1] at the European Synchrotron Radiation Facility (ESRF) in Grenoble, France. At the BM1A station a 2 mrad fan of radiation is firstly vertically collimated by a primary mirror, with a cut-off angle of 24 keV. Afterwards the reflected beam passes a double crystal monochromator and is finally vertical focused by the second mirror. The diffractometer itself combines a flexible kappagoniometer with a fast hybrid-pixel Pilatus2M detector, which can be translated into two directions as well as rotated. As result, a large variety of diffraction experiments can be performed: single crystal-, thin film- and powder diffraction, with a broad covering of the reciprocal space and an optimal angular resolution.

A.2 SQUID

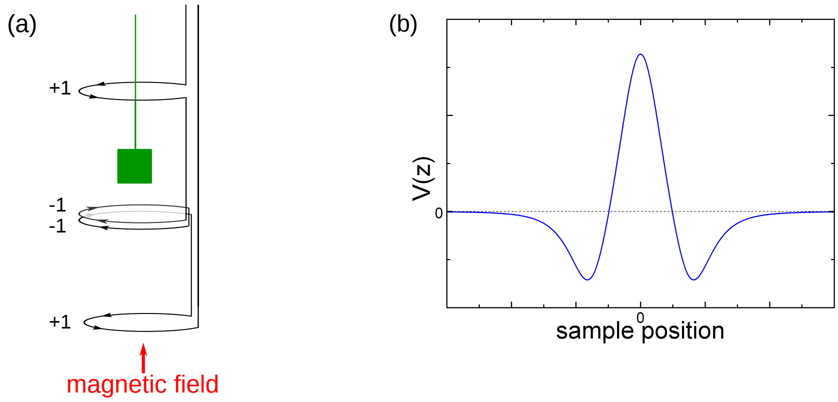

Figure A.2: Second-order-gradiometer detection coils (a) and the output voltage dependent on the sample position within the detection coils (b).

To measure the magnetic properties of small amounts of materials one can use two principal methods. The first that requires the motion of the sample (e.g. vibrating sample, SQUID), and the second measures a force or torque on the samples (e.g. torque magnetometers, Faraday balance). The temperature dependent magnetic susceptibility and field depend magnetisation measurement in this work have been carried out by using a commercial available magnetic property measurements system (MPMS-3S) by Quantum design, which is located at the Institute for Physics of Condensed Matter at the Technische Universität Braunschweig, Germany. The accessible temperature range is between 1.8 K and 400 K with a magnetic field range up to 5.0 T. For the measurement the magnetic moment of the samples can be approximated as a magnetic dipole with a constant sign and value. The measurement with the MPMS is performed by moving the sample through a superconducting, second-order-gradiometer detection coils [Fig.A.2 (a)]. The opposite electric fields in the two coils, induced by the spatial homogeneous external field, cancel each other out, while the inhomogeneous field induced by the sample, approximated as dipole field, induces different currents in the coils. The detection coils are coupled to the Superconducting QUantum Interference Device (SQUID), which works in principal as highly linear current-to-voltage converter [the typical measured voltage is shown in FigA.2 (b)]. The dc-SQUID device as used in this work consists of a superconducting ring with two Josephson junctions. A bias current is driven through the ring, if the magnetic flux in the ring changes, the voltage oscillates. This oscillation belongs to the increase of the magnetic field by one flux quantum $\Phi_0 = h/2e = 2.07 \cdot 10^{-15}$ T·m^2 within the ring.

A.3 SANS-1

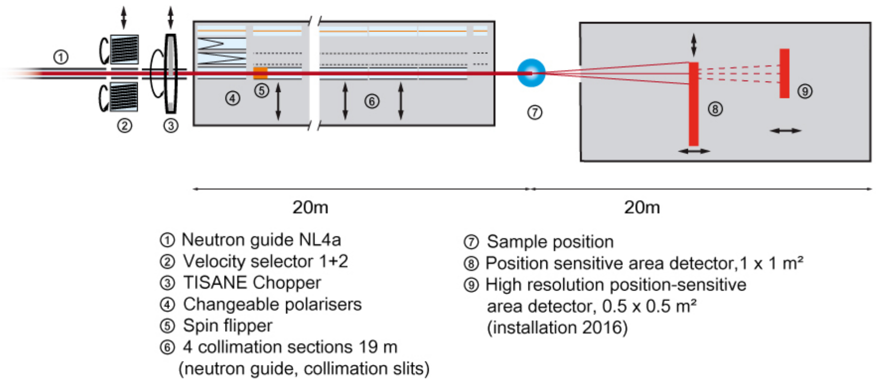

Figure A.3: Schematic view of SANS-1 small angle neutron scattering instrument at the MLZ Garching, Germany [san].

The SANS-1 [GOS$^+$, GOP, MHW$^+$] small angle scattering instrument is located at the 20 MW research reactor Munich II (FRM II), based at the Heinz Maier-Leibnitz-Zentrum (MLZ) in Garching, Germany. A schematic view of the instrument is shown in Figure A.3. During this work the monochromatically mode has been used, with the low resolution velocity selector, which can be changed automatically to a higher resolution one, if required. The available wavelength band is in the range of 4 Å to 30 Å. A S-shaped neutron guide, coming from the cold source, is used in front of the velocity selector to reduce the background from fast neutrons. Behind the selector tower, an optional Fe/Si transmission polariser can be installed for polarised measurements, covering the full wavelength band. In the following part a flexible 20 m collimation system, with additional slits, is attached. The primary 1 × 1 m^2 detector is located inside the detector tube and can be used for sample-detector positions between 0.5 m and 20 m. This detector is made of 128 He^3 position sensitive tubes with a spatial resolution of 8 mm × 8 mm and an active area of 1000 × 1020 mm^2. It is planned to install a second, high resolution detector (3 mm × 3 mm, active area of 500 × 500 mm^2) in 2016. Additional the installation of a TISANE chopper disc set-up is planned for the end of 2015, enable kinetic neutron scattering experiments in the μs regime, a complete upgrade to a time-of-flight (TOF) option is planned for the future. The technical data for SANS-1 are summarised in Table A.1.

A.4 D22

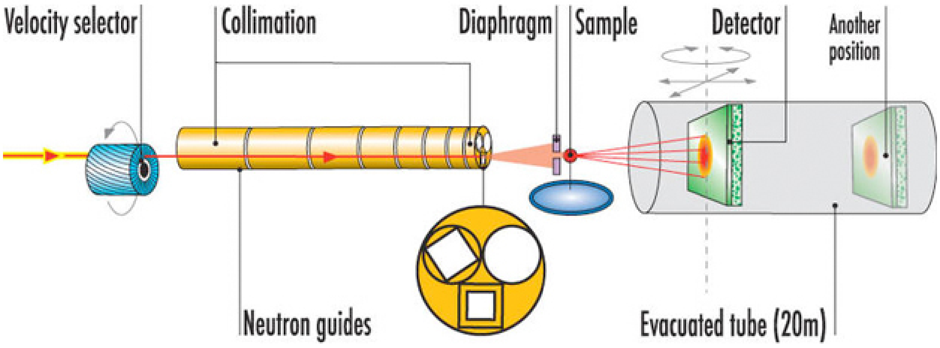

Figure A.4: Schematic view of the D22 small angle neutron scattering instrument at the ILL, Grenoble, France [d22].

The second SANS instrument used in this work is D22, which is shown schematically in Fig.A.4. Analogue to SANS-1, it is a standard, pinhole like small angle neutron scattering machine, located at the cold source of the 58 MW reactor at the Institute Laue Langevin (ILL) in Grenoble, France. It is operated monochromatically, with a maximal collimation length of 20 m and an analogue sample detector distance. The characteristics of D22 are also summarised in Table A.1.

Table A.1: Characteristics of the small angle neutron scattering instruments SANS-1 [san] and D22 [d22]

	SANS-1	D22
velocity selector $\Delta\lambda/\lambda$	10 % low resolution 6 % high resolution	standard:10 %, 8 - 20 % by vertical rotation of the selector
wavelength λ	4.5 - 30 Å	4.5 - 40 Å
source-to-sample	1, 2, 4, 8, 12, 16, 20 m	1.4, 2.0, 2.8, 4.0, 5.6, 8.0, 11.2, 14.4, 17.6 m
maximum flux at sample (for $\Delta\lambda/\lambda$ 10 %)	6.1×10^7 n cm^{-2} s^{-1} for 5.5 Å	1.2×10^8 n cm^{-2} s^{-1} for 6 Å
sample-detector	1.2 - 20 m	1.1 - 17.6 m
Q-range	0.0005 - 1Å^{-1}	0.0015 - 1Å^{-1}
det. 1: active area	1000 × 1020 mm^2	1024 × 980 mm^2
pixel size	8 mm × 8 mm	8 mm × 8 mm
maximal count rate	1 MHz	5 MHz

Appendix B

Theoretical approach $Mn_{1-x}Fe_xGe$

Recently, the possibility was shown to reproduce the experimentally observed change of the sign of the DM constant D in the $Mn_{1-x}Fe_xGe$ system theoretically. In this section the short overview given above in section 4.2.4 will be completed. It is very likely that the same mechanism, which is responsible for sign change observed in $Mn_{1-x}Fe_xGe$ is also responsible for the flip of the chiral link in $Fe_{1-y}Co_yGe$, as well as, $Fe_{1-z}Co_zSi$. In the first part of this chapter the results of Chen and co-workers [CXYL], using monte carlo simulations will be presented and afterwards the density functional calculations by Koretsune and co-workers [KNA] and Gayles and co-workers [GFS⁺].

Monte Carlo simulation

Chen and co-workers used a simple spin model on a 2D lattice with a hybrid DM interaction [CXYL]:

$$\begin{aligned}\mathcal{H} = &- J\sum_i S_i\left(S_{i+\hat{x}} + S_{i+\hat{y}}\right)\\ &- D\sum_i \left(S_i \times S_{i+\hat{x}} \cdot \hat{x} + S_i \times S_{i+\hat{y}} \cdot \hat{y}\right)\\ &- A\sum_i \left(S_i^x S_{i+\hat{x}}^x + S_i^y S_{i+\hat{y}}^y\right) - H\sum_i S_i\end{aligned} \tag{B.1}$$

H represents the magnetic field along the z-axis, J the ferromagnetic exchange (FM) interaction, D the DM interaction, A the anisotropy between neighbouring atoms. They simply assume the effective parameters between the Mn-Fe pairs as: $J \equiv (J_{Mn} + J_{Fe}/2)$, $D \equiv (D_{Mn} + D_{Fe}/2)$ and $A \equiv A_{Mn}/2$. This approach

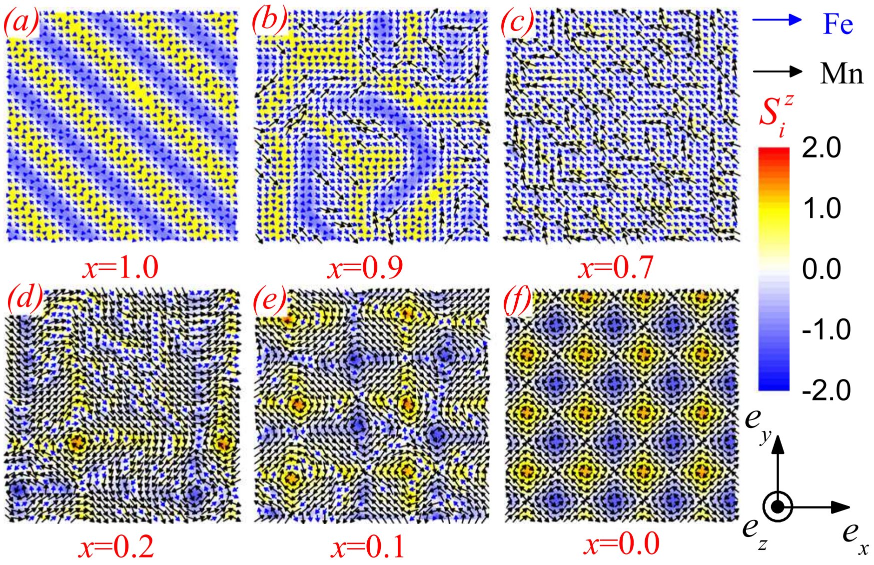

Figure B.1: A series of typical spin lattice s with various concentration x under H = 0.16 T for $Mn_{1-x}Fe_xGe$ (Reprinted from [CXYL], with the permission of AIP Publishing).

is phenomenological solid, but has a lack of a rigorous theoretical foundation. For their simulations they randomly distribute the Mn and Fe species on the 2D square lattice for x. They used a positive and negative DM constant for MnGe ($D_{Mn} = \sqrt{6}$) and FeGe ($D_{Fe} = -1.44$), respectively. Snapshots of typical spin lattices received by Monte Carlo simulation are shown in Fig.B.1. For pure FeGe the spin structure has been identified as single helix [Fig.B.1 (a)], while the spin structure of pure MnGe [Fig.B.1 (f)] has been identified as a superposition of two orthogonal helices [CXYL]. Additional, Chen and co-workers received the concentration dependence of $\langle \gamma_m \rangle$ given in Fig.B.2 (a) as well as the temperature dependence of $\langle \gamma_m \rangle$ [Fig.B.2 (b)] and $\langle M \rangle$ [Fig.B.2 (c)]. The $\langle \gamma_m \rangle$-x dependence received by Monte Carlo simulation is in a good agreement with the experimental determined behaviour from the polarised neutron scattering experiments in the helical phase as well as the Lorentz transmission electron microscopy measurements in the *A-phase* by Shibata and co-workers [SYH$^+$]. The change of the sign of $\langle \gamma_m \rangle$ is given at $x = 0.7$ accompanied by ferromagnetic-like behaviour. The temperature dependence of $\langle \gamma_m \rangle$ fluctuates around 0 for $x_c = 0.7$ and is positive, negative for $x < x_c = 0.7$, $x > x_c = 0.7$, respectively. The additional calculated susceptibility data χ are in a good agreement with the experimental one. The curve for the sample with the concentration of $x = 0.7$ has a Curie-Weiss-like shape, typically

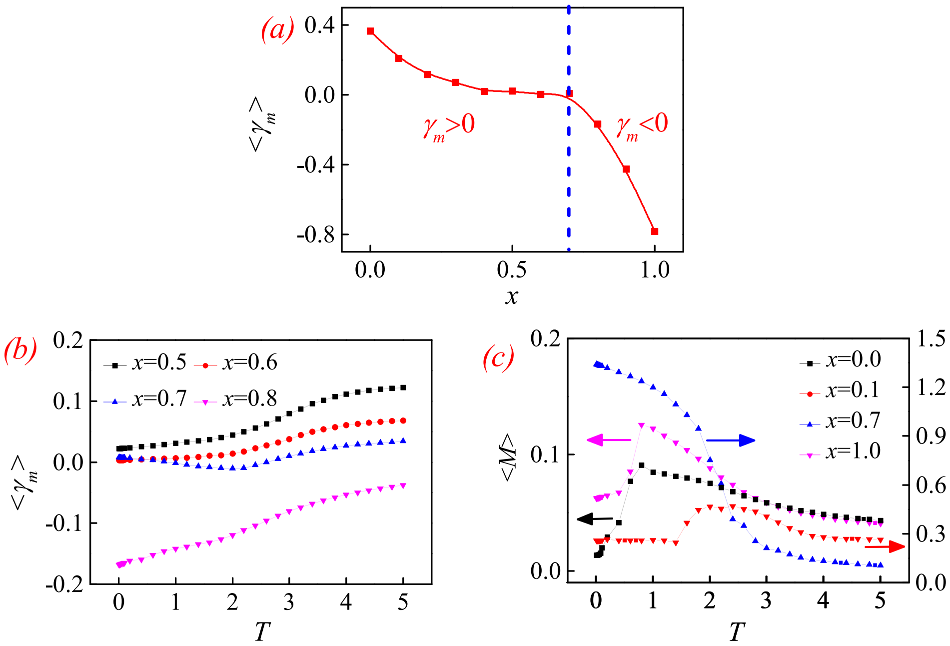

Figure B.2: Plots for (a) $\langle\gamma_m\rangle$-x, (b) $\langle\gamma_m\rangle$-T and (c) $\langle M\rangle$-T for various x under $H = 0.16$ for $\mathrm{Mn}_{1-x}\mathrm{Fe}_x\mathrm{Ge}$ (Reprinted from [CXYL], with the permission of AIP Publishing).

for a ferromagnetic spin arrangement, all other compounds show a helimagnetic-like shape.

Density functional calculations

In addition to the Monte Carlo simulation results shown in the previous section there are two approaches using density functional theory (DFT) calculations. Koretsune and co-workers [KNA] used DFT calculation to compute the spin susceptibility that is directly proportional to the DM interaction. In their approach they used a rigid band approximation starting from the electronic structure of FeGe as well as MnGe. Their results for the DM interaction coefficients and the anomalous hall effect (AHE) are shown in Fig.B.3 (starting from the FeGe band structure). From both starting points (MnGe and FeGe) they have been able to qualitatively reproduce the change of the sign of D in $\mathrm{Mn}_{1-x}\mathrm{Fe}_x\mathrm{Ge}$ with the variation of the Mn/Fe ratio. Their results show $D < 0$ below x_c (MnGe-like region) and $D > 0$ for $x > x_c$ (FeGe-like region). The calculated critical concentration however differs slightly from the experimental determined value of $x_c \approx 0.75$. Gayles and co-

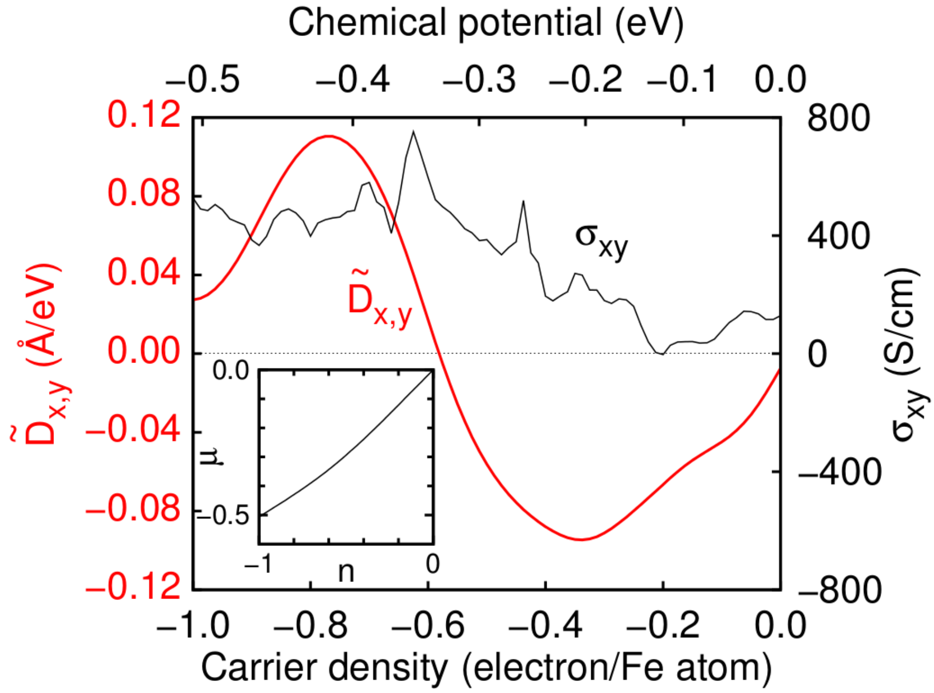

Figure B.3: DM interaction and AHC as function of the carrier density n starting from the FeGe electronic structure. The inset shows the dependence of the chemical potential μ on the carrier density n (figure taken from [KNA]).

workers [GFS⁺], on the other hand, have chosen two similar approaches. In their first method, they used the expression for the DM based on the Berry phase in the weak spin orbit interaction limit (SOI). The second one is based on the evaluation of the linear slope of the dispersion energy of the long wavelength flat spiral solution including the SOI within the first order perturbation theory. The calculated strength of the DM interaction is shown in Fig.4.8. The observed change of the sign of D could be reproduced with both methods and the critical Fe-concentration has been determined as $x_c = 0.8$, which is in excellent agreement with the experimental value of $x_c \approx 0.75$. Moreover, they developed a minimal tight-binding model which allows to identify the main mechanism behind the change of D. They established the dynamics of the d_{xy} and $d_{x^2-y^2}$-like states as the responsible mechanism for the changing behaviour of the DM. Strictly speaking, the d_{xy} and $d_{x^2-y^2}$ states move down and up, and thus become occupied and unoccupied with increasing concentration x, respectively.

Appendix C

The role of the cubic anisotropy

To be complete, the calculations concerning the role of the cubic anisotropy transforming the spiral to the ferromagnetic spin structure in B20 compounds (summarised in section 4.3.3) are given here in more detail according to [GSM].

Bak-Jensen model

Resuming the results of the Bak-Jensen model from section 1.2.2, the DM interaction disorders the ferromagnetic structure in cubic B20 compounds and stabilises a helical state [BJ, Malb]. The corresponding Hamiltonian is a sum of the exchange energy H_{EX}, the DM energy H_{DM}, the anisotropic exchange energy H_{AE} and the Zeeman energy H_Z:

$$\begin{aligned} H_{EX} &= -\frac{1}{2}\sum J_{\boldsymbol{R}-\boldsymbol{R}'}\boldsymbol{S}_{\boldsymbol{R}}\cdot\boldsymbol{S}_{\boldsymbol{R}'}; \\ H_{DM} &= \frac{1}{2}\sum D_{\boldsymbol{R}-\boldsymbol{R}'}(\nabla-\nabla')[\boldsymbol{S}_{\boldsymbol{R}}\times\boldsymbol{S}_{\boldsymbol{R}'}]; \\ H_{AE} &= \frac{1}{2}\sum F_{\boldsymbol{R}-\boldsymbol{R}'}\{(\nabla_x S^x_{\boldsymbol{R}})(\nabla'_x S^x_{\boldsymbol{R}'}) \\ &\quad + (\nabla_y S^y_{\boldsymbol{R}})(\nabla'_y S^y_{\boldsymbol{R}'}) + (\nabla_z S^z_{\boldsymbol{R}})(\nabla'_z S^z_{\boldsymbol{R}'})\}; \\ H_Z &= -\boldsymbol{H}\sum \boldsymbol{S}_{\boldsymbol{R}}, \end{aligned} \tag{C.1}$$

where $\boldsymbol{H} = g\mu_B\boldsymbol{B}_{in}$ with an internal magnetic field $\boldsymbol{B}_{in}$ [Malb]. The general form of the spin helix is given by:

$$\boldsymbol{S}_{\boldsymbol{R}} = S[\hat{c}\sin\alpha + (\boldsymbol{A}e^{i\boldsymbol{k}\cdot\boldsymbol{R}} + \boldsymbol{A}^{*}e^{-i\boldsymbol{k}\cdot\boldsymbol{R}})\cos\alpha] \tag{C.2}$$

Here α is the angle between the spins and the spin rotation plane and $\boldsymbol{k}$ is the helix wave-vector. Using $\boldsymbol{A} = (\hat{a} - i\hat{b})/2$ to determine vector $\boldsymbol{A}$ and the unit vectors $\hat{a}, \hat{b}, \hat{c}$ form the right handed orthogonal frame with $[\hat{a}\times\hat{b}] = \hat{c}$. Thus, one has

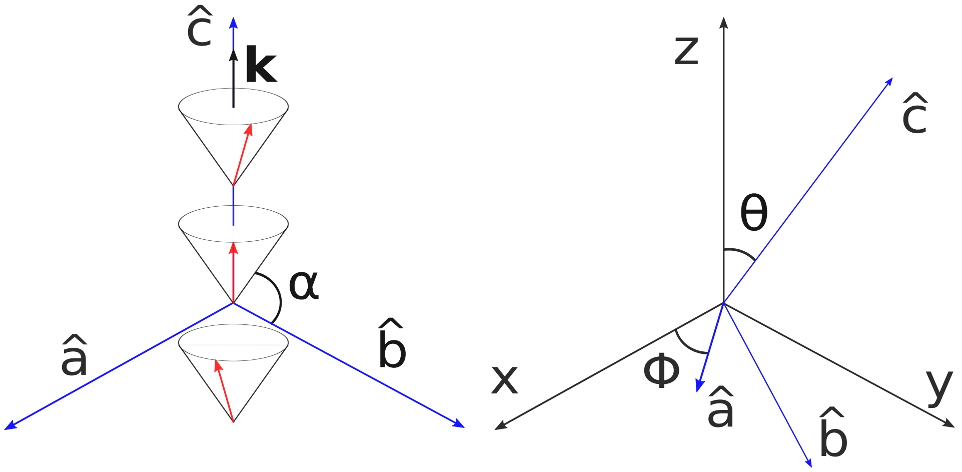

Figure C.1: Spherical coordinates.

$(\boldsymbol{A}\cdot\boldsymbol{A}) = 0, (\boldsymbol{A}\cdot\boldsymbol{A}^*) = 1/2, [\boldsymbol{A}\times\boldsymbol{A}^*] = i\hat{c}/2$. In spherical coordinates with the angles ϕ, θ bound to the spin helix, the basics vectors $\hat{a}, \hat{b}$ and $\hat{c}$ can be rewritten as (see Fig.C.1 for illustration):

$$\begin{aligned}\hat{a} &= (\cos\phi, \sin\phi, 0);\\ \hat{b} &= (-\sin\phi\cos\theta, \cos\phi\cos\theta, -\sin\theta);\\ \hat{c} &= (-\sin\phi\sin\theta, \cos\phi\sin\theta, \cos\theta).\end{aligned} \tag{C.3}$$

The classical energy (approximated in k^2) can be obtained by inserting Eq.C.2 in Eq.C.1:

$$E_{BJ} = -\frac{S^2 J_0}{2} + \left[\frac{Ak^2}{S} + \frac{F_0 I(\boldsymbol{k})}{2} - 2D_0(\boldsymbol{k}\cdot\hat{c})\right]\frac{S^2\cos^2\alpha}{2} - SH_{\|}\sin\alpha, \tag{C.4}$$

with the spin wave stiffness $A = S(J_0 - J_{\boldsymbol{k}})/k^2$ [Malb], the $\boldsymbol{k}$-dependent functions are determined as $J_{\boldsymbol{k}} = \sum J_{\boldsymbol{R}}\exp(\boldsymbol{k}\cdot\boldsymbol{R})$, $I(\boldsymbol{k}) = \sum k_j^2(\hat{a}_j^2 + \hat{b}_j^2)$ is a cubic invariant and $H_{\|} = (\boldsymbol{H}\cdot\hat{c})$. E_{BJ} refers to the Bak-Jensen (BJ) model [BJ]. The energy can be minimised with respect to $\boldsymbol{k}$ with:

$$\begin{aligned}Ak_j + SF_0k_j(\hat{a}_j^2 + \hat{b}_j^2)/2 &= SD_0\hat{c}_j;\\ A\boldsymbol{k}^2 + SF_0I(\boldsymbol{k})/2 &= SD_0(\boldsymbol{k}\cdot\hat{c}),\end{aligned} \tag{C.5}$$

the first line in Eq.C.5 demonstrated the weak dependence of the orientation of $\boldsymbol{k}$ on the crystal structure. Neglecting this, one obtain:

$$\boldsymbol{k}_s = SD_0\hat{c}/A. \tag{C.6}$$

The final expression for E_{BJ} can be obtained by substituting $D_0 = Ak_s/S$ into Eq.C.4:

$$E_{BJ} = -\frac{S^2 J_0}{2} - \frac{SAk_s^2 \cos^2\alpha}{2}\left[1 - \frac{SF_0 I(\hat{c})}{2A}\right] - SH_{\parallel}\sin\alpha. \tag{C.7}$$

Here the second term represents the DM interaction and corresponds to the energy gain of the helical state as compared with the ferromagnetic one. The cubic invariant $I(\hat{c})$ has the minimum $I = 0$ and the maximum $I = 2/3$ at $\hat{c} = (1,0,0)$ and $\hat{c} = (1,1,1)/\sqrt{3}$, respectively. For small magnetic fields $H \ll |F_0|k_s^2$ the vector $\boldsymbol{k}_s$ points along the cubic edge or diagonal for $F_0 > 0$ and $F_0 < 0$, respectively [BJ, Malb]. For the opposite case $H \gg |F_0|k_s^2 \sim H_{c1}$ one can find the helix wave vector along the field axis $\boldsymbol{k}_s \parallel \boldsymbol{H}$. Not considering the F_0 term (connecting to the exchange anisotropy and minimising the energy with respect to the angle α) in Eq.C.7:

$$\sin\alpha = H/Ak_s^2. \tag{C.8}$$

Accordingly, for $H = 0$, then $\alpha = 0$, resulting in a plane helix. In consequence, a field of $H \neq 0$ implies the existence of a conical spin alignment. Reaching the critical field H_{c2}, $\alpha = \pi/2$ and $H_{c2} = Ak_s^2$, the cone transforms to a field aligned (ferromagnetic) state, for $H > H_{c2}$ [Malb].

Cubic anisotropy

The anisotropic exchange is small compared to the isotropic one, in consequence, Maleyev and co-workers neglected the F_0 from Eq.C.7. However, another anisotropic term, the cubic anisotropy has to be considered:

$$H_{CA} = K\sum\{(S_{\boldsymbol{R}}^x)^4 + (S_{\boldsymbol{R}}^y)^4 + (S_{\boldsymbol{R}}^z)^4\}. \tag{C.9}$$

In case of a ferromagnet: $\boldsymbol{S_R} = \boldsymbol{S}$ and the contribution of the cubic anisotropy to the classical energy can be written as:

$$E_{CA} = G\begin{cases} 1; \boldsymbol{S} \parallel (1,0,0), \\ 1/3; \boldsymbol{S} \parallel (1,1,1). \end{cases} \tag{C.10}$$

Here, $G = KS^4$ and the extrema of E_{CA} are shown in the right handed side of Eq.C.10. The directions $(1,1,1)$ and $(1,0,0)$ are for this reason the easy axes for $K > 0$ and $K < 0$, respectively. Inserting Eq.C.6 in Eq.C.9 and combine it with Eq.C.7, one gets the helix energy in a magnetic field, taking the cubic anisotropy into account:

$$\begin{aligned} E = &-(SAk_s^2/2)\cos^2\alpha + G[C\sin^4\alpha + (3/8)B\cos^4\alpha \\ &+ 3I\sin^2\alpha\cos^2\alpha] - SH_{\parallel}\sin\alpha. \end{aligned} \tag{C.11}$$

with the cubic invariants C, B, I given by:

$$C = \sum \hat{c}_j^4; \quad B = \sum (\hat{a}_j^2 + \hat{b}_j^2)^2; \quad I = \sum \hat{c}_j^2 (\hat{a}_j^2 + \hat{b}_j^2). \tag{C.12}$$

They depend on the angles ϕ, θ determining the $\hat{c}$ direction (see details at the end of this chapter). Considering Eq.C.30 and rewrite Eq.C.11, one gets:

$$\begin{aligned} E = & -\frac{SAk_s^2}{2}\left(1 - \sin^2\alpha\right) + \frac{G}{8}[(3-5C)\left(-7\sin^4\alpha + 6\sin^2\alpha + 1\right) + 8C] \\ & - SH_{\|}\sin\alpha. \end{aligned} \tag{C.13}$$

In this term the first expression gives the energy of the helical structure with the wave vector k_s, appearing as a result of the competition between the ferromagnetic exchange and the DM interaction. The second term gives the anisotropic energy of the spiral and depends on the angles ϕ, θ of the direction of the vector $\hat{c}$. In this expression the cubic anisotropy is a function of one cubic invariant C and of the powers of sine and conical angle α only. The spin structure and the magnetic field behaviour of the B20 helimagnets is determined by the minimum of this energy. The situation for zero magnetic field is discussed above in section 4.3.3. Now the case with an applied magnetic field will be considered in more detail. Considering a positive anisotropy $G > 0$ and an arbitrary oriented magnetic field in the range of ϕ between 0 and $\pi/4$ and θ between 0 and $\pi/2$, the energy of the helix in the magnetic field is given by:

$$\begin{aligned} E = & \frac{SAk_s^2}{2}\sin^2\alpha + \frac{G}{16}W(-7\sin^4\alpha + 6\sin^2\alpha + 1) \\ & - SH\cos(\theta - \theta_H)\cos(\phi - \phi_H)\sin\alpha - \frac{SAk_s^2}{2} + GC, \end{aligned} \tag{C.14}$$

with θ_H and ϕ_H denote the angles of the magnetic field direction. Putting the cubic invariant $W(\theta, \phi) \equiv 10C - 6$ (Eq.C.31), with increasing magnetic field the planar spiral ($\alpha = 0$), aligned along the $(1, 1, 1)$-axis, i.e. $(\theta, \phi) = (\pi/2 - \arctan(1/\sqrt{2}), \pi/4)$, will turn toward the (θ_H, ϕ_H). Moreover, the conical angle α will increase. The condition corresponding to the minimum of the energy in respect to α, θ and ϕ is given by:

$$\begin{aligned} \partial E/\partial\alpha &= 0 \\ \partial E/\partial(\theta, \phi) &= 0. \end{aligned} \tag{C.15}$$

To estimate the critical field H_{c1}, at which the helix is aligned along the field direction, one has to consider the limiting case of the field orientation along the hard axis (0,0,1). Thus, $\theta_H = 0, \phi_H = \pi/4$ in Eq.C.14 and θ runs from $\pi/2 -$

$\arctan(1/\sqrt{2})$ (diagonal of the cube) to 0 with constant $\phi = \pi/4$. From the solution of Eq.C.15, with respect to α and substituting $\theta = 0$, the conical angle at H_{c1} is given by:

$$\sin^2 \alpha_{c1} = \frac{4}{7}\left(1 + r - \sqrt{r^2 + 2r + \frac{9}{16}}\right), \quad r > \sqrt{\frac{1}{30}}, \tag{C.16}$$

with the ratio of the DM interaction $r = SAk_s^2/12G$ and the cubic anisotropy. Combining Eq.C.15 with Eq.C.16 the corresponding critical field is given by:

$$H_{c1} = \frac{G}{S} \sin \alpha_{c1} \left(7 \sin^2 \alpha_{c1} + 12r - 3\right), \quad r > \sqrt{\frac{1}{30}}. \tag{C.17}$$

It can be seen that the value of the critical field H_{c1} is smaller, the closer the applied field is to the easy axis. For the second critical field H_{c2} one can consider the equation:

$$SH = \frac{7}{4} GW(\theta_H, \phi_H) \sin^3 \alpha + \left(SAk_s^2 - \frac{3}{4} GW(\theta_H, \phi_H)\right) \sin \alpha, \tag{C.18}$$

where (θ, ϕ) are already equal to (θ_H, ϕ_H). Equation C.18 describes the behaviour of the helix above H_{c1}. The value for H_{c2} is also dependent on the field direction. It can be seen that the cubic invariant W is negative for those (θ, ϕ) which are close to the cube diagonal and is positive for those (θ, ϕ) close to the cube edge. One can distinguish between two cases: for $W(\theta_H, \phi_H) \geq 0$ the solution for $\sin \alpha = 1$ is given by:

$$H_{c2} = Ak_s^2 + W(\theta_H, \phi_H) \frac{G}{S}. \tag{C.19}$$

In the second case $W(\theta_H, \phi_H) < 0$, the result depends on the ratio of the DM and the cubic anisotropy and for $SAk_s^2/G \geq 18|W|/4$, Eq.C.18 has a solution for $\sin \alpha = 1$ at:

$$H_{c2} = Ak_s^2 - |W(\theta_H, \phi_H)| \frac{G}{S}. \tag{C.20}$$

In the opposite case $SAk_s^2/G < 18|W|/4$, a first order transition to the ferromagnetic state takes place at the critical field:

$$H_{c2} = \sin \alpha_{c2} \left(\frac{2}{3} Ak_s^2 + \frac{1}{2} |W(\theta_H, \phi_H)| \frac{G}{S}\right). \tag{C.21}$$

with the corresponding critical cone angle:

$$\sin \alpha_{c2} = \sqrt{\frac{4}{21|W|} \frac{SAk_s^2}{G} + \frac{1}{7}}. \tag{C.22}$$

In Fig.C.2 the dependence of the critical field H_{c2} on the field direction in the particular case of the field oriented between the hard $(0,0,1)$ axis and the easy $(1,1,1)$ axis is shown. Maleyev and co-workers plotted Eqs.C.17, C.18 and C.19, for example, for $Ak_s^2 = 12G/S$ and $Ak_s^2 = 5G/S$. The position of the curve along the H_{c2} axis is given by SAk_s^2/G, and its form by W (Eq.C.32). In the case of $Ak_s^2 < 12G/S$ a part of the curve corresponds to the first order phase transition described by Eq.C.21. Fig.C.3 also shows the critical field H_{c2} and the critical cone angle [Eq.C.22] as function of the ratio r for the field along $(1,1,1)$. For polycrystalline samples, one has to take the average of the magnetic field applied to all directions. For this reason, $W(\theta,\phi)$ [Eq.C.31] must be averaged on θ,ϕ and:

$$H_{c2} = Ak_s^2 + \frac{9}{16}\frac{G}{S}, \quad G > 0. \tag{C.23}$$

In the case of $G < 0$, the first critical field H_{c1} is equal to Eq.C.17 but for $r = SAk_s^2/8|G|$. Eq.C.18 includes G only in the term $G \cdot W$, for the case of negative anisotropy $G < 0$, the replacement $G \to -|G|$ is equivalent to replacement $W \to -|W|$. Averaging of W gives in this case:

$$H_{c2} = Ak_s^2 - \frac{9}{16}\frac{|G|}{S}, \quad G < 0. \tag{C.24}$$

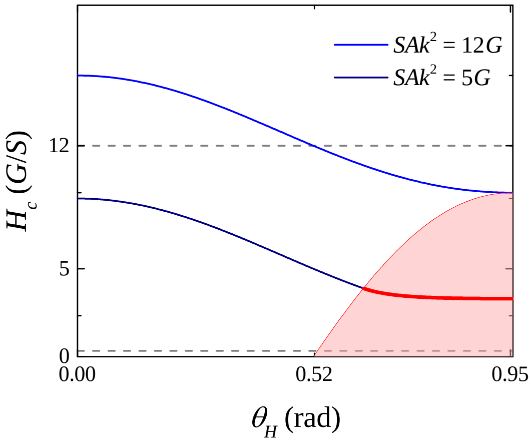

Figure C.2: Dependence of the critical magnetic field H_{c2} (in units G/S) on the orientation of the magnetic field within $\phi = \pi/4$ plane changing from $(0, 0, 1)$ to $(1, 1, 1)$ directions for two variants of the ratio of the DM interaction and the cubic anisotropy. The top dashed line corresponds to the ratio SAk_s^2/G, which does not imply any first order phase transition in any field direction. The bottom dashed line corresponds to the minimal stable value of the SAk_s^2/G equals $1/3$. The red area shows the condition of the first order phase transition, which depends on the angle θ and the ratio SAk_s^2/G (Reprinted figure with permission from [GSM], Copyright (2015) by the American Physical Society).

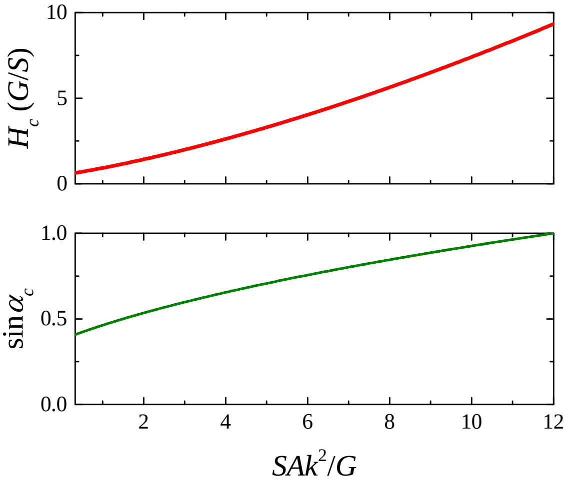

Figure C.3: Dependence of the sine of the critical cone angle α_{c2} and the critical magnetic field (along the $(1, 1, 1)$ direction) of the first order phase transition H_{c2} on the ratio SAk_s^2/G (Reprinted figure with permission from [GSM], Copyright (2015) by the American Physical Society).

Cubic invariants

For completeness the expressions for the cubic invariants are given here analogously to [GSM]. For the cubic anisotropy:

$$E_{CA} = G[(\cos^4\phi + \sin^4\phi)\sin^4\theta + \cos^4\theta], \tag{C.25}$$

and Eq.C.10 is a result of the standard calculations. With Eq.C.3 insert in $I(\hat{c})$ of Eq.C.7, one obtain:

$$I(\hat{c}) = [2\sin^2\phi\cos^2\phi + (1 + \sin^4\phi + \cos^4\phi)\cos^2\theta]\sin^2\theta. \tag{C.26}$$

The cubic invariant $I(\hat{c})$ has minimum $I = 0$ and maximum $I = 2/3$ at $\hat{c} = (1, 0, 0)$ and $\hat{c} = (1, 1, 1)/\sqrt{3}$, respectively. The first invariants of the two given in Eq.C.12 is given as:

$$C = \sum c_j^4 = \begin{cases} 1; \hat{c} \parallel (0, 0, 1) \\ 1/3; \hat{c} \parallel (1, 1, 1). \end{cases} \tag{C.27}$$

The right handed side gives the extrema of C and the second invariant is determined as:

$$B = \sum (a_j^2 + b_j^2)^2 = (\cos^2\phi + \sin^2\phi\cos^2\theta)^2 + (\sin^2\phi + \cos^2\phi\cos^2\theta)^2 + \sin^4\theta, \tag{C.28}$$

and one get for the extrema:

$$B = \begin{cases} 2; \hat{c} \parallel (0, 0, 1) \\ 4/3; \hat{c} \parallel (1, 1, 1). \end{cases} \tag{C.29}$$

The simple relations between cubic invariants are given by:

$$C - B = 1, \quad I + C = 1, \quad I + B = 2. \tag{C.30}$$

The extrema of cubic invariant $W \equiv 10C - 6$:

$$W = \begin{cases} 4; \hat{c} \parallel (0, 0, 1) \\ -8/3; \hat{c} \parallel (1, 1, 1). \end{cases} \tag{C.31}$$

At $\phi = \pi/4$ W has the simple form:

$$W(\theta, \phi = \pi/4) = 15\cos^4\theta - 10\cos^2\theta - 1. \tag{C.32}$$

Appendix D

$\mathrm{Fe}_{1-z}\mathrm{Co}_z\mathrm{Si}$ polarised measurements

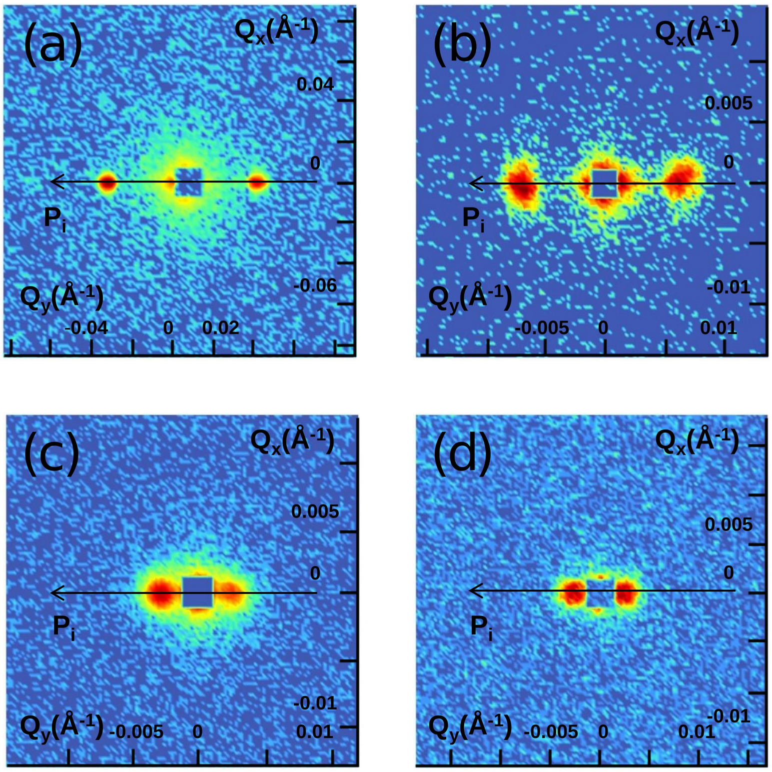

Figure D.1: Maps of polarised SANS intensities of MnSi (a) and of $\mathrm{Fe}_{1-z}\mathrm{Co}_z\mathrm{Si}$ with $z = 0.5$ (b), 0.6 (c), 0.7 (d) for polarisation $+\boldsymbol{P}_i$ opposite to the guide field at $T \approx 3.5$K.

In addition to section 4.4.2 the corresponding measurements for MnSi, $\mathrm{Fe}_{1-z}\mathrm{Co}_z\mathrm{Si}$

(z = 0.5, 0.6, 0.7) with the flipped polarisation direction opposite to the field Fig.D.1 as well as the integrated intensities for the left Bragg peak for the flipper off and on measurements Fig.D.2 are presented here.

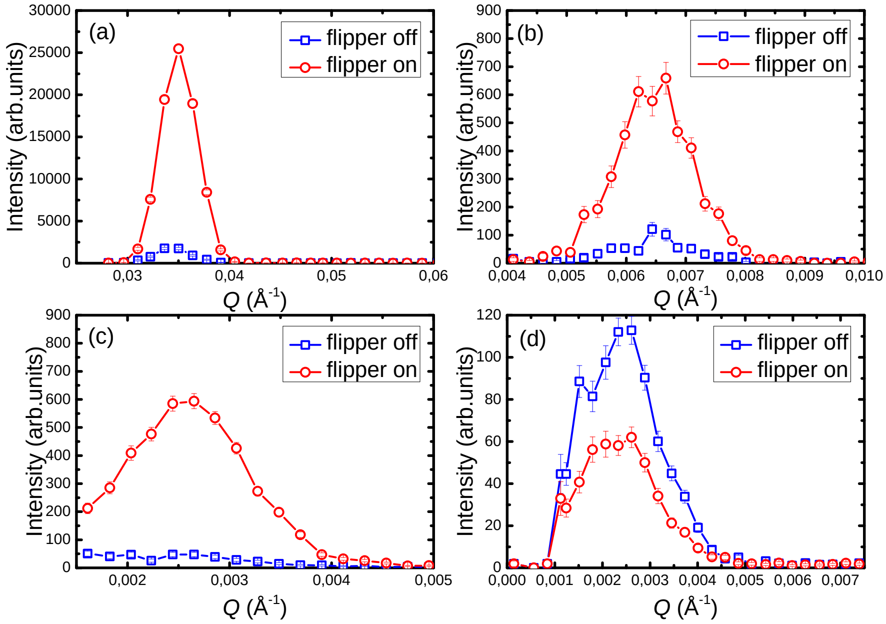

Figure D.2: The integrated intensities of MnSi (a) and of Fe$_{1-z}$Co$_z$Si with $z = 0.5$ (b), 0.6 (c), 0.7 (d) for the left Bragg peak (polarisation $+\boldsymbol{P}_i$ along/opposite the guide field at $T \approx 3.5$K).

Appendix E

Physical quantities and symbols

Notation	Name
A	spin wave stiffness
b_j	nuclear scattering length of nucleus j
D	Dzyaloshinskii-Moriya constant
$\boldsymbol{k}_i$, $\boldsymbol{k}_f$	initial and final wave vector of neutrons
$\boldsymbol{k}_s$	helix wave vector
$\boldsymbol{l}$	lattice vector
$\boldsymbol{M}_{\boldsymbol{Q}}$	magnetic structure vector
$\boldsymbol{M}_{\boldsymbol{Q}_\perp}$	magnetic interaction vector
$\boldsymbol{N}_{\boldsymbol{Q}}$	nuclear structure factor
$\boldsymbol{P}_i$, $\boldsymbol{P}_f$	initial and final polarisation vector
$\widetilde{\boldsymbol{P}}$	polarisation tensor
$\boldsymbol{Q}$	scattering vector
$\hat{\sigma}_i$	Pauli matrices
$\boldsymbol{S}_l$	average spin of a magnetic atom at the site l
$\boldsymbol{\tau}$	reciprocal lattice vector
$V(\boldsymbol{r})$	neutron scattering potential
$x_{(c)}$	(critical) Fe concentration in $\mathrm{Mn}_{1-x}\mathrm{Fe}_x\mathrm{Ge}$
$y_{(c)}$	(critical) Co concentration in $\mathrm{Fe}_{1-y}\mathrm{Co}_y\mathrm{Ge}$
$z_{(c)}$	(critical) Co concentration in $\mathrm{Fe}_{1-z}\mathrm{Co}_z\mathrm{Si}$
$\lvert\uparrow\rangle$, $\lvert\downarrow\rangle$	spin up, spin down

Quantity	Name	Value
e	Elementary charge	$1.602\ 176\ 6208 \times 10^{-19}$ C
$\hbar$	Planck constant over 2π	$6.582119514 \times 10^{-16}$ eV s
m_e	mass of electron	$9.10938356 \times 10^{-31}$ kg
m_n	mass of neutron	$1.674927471 \times 10^{-27}$ kg
m_p	mass of proton	$1.672621898 \times 10^{-27}$ kg
μ_B	Bohr magneton	$9.274009994 \times 10^{-24}$ J T^{-1}
μ_N	nuclear magneton	$5.05078353 \times 10^{-21}$ J T^{-1}
μ_0	vacuum permeability	$1.2566370614 \times 10^{-6}$ N A^{-2}
r_0	classical electron radius	$2.82179403267 \times 10^{-15}$ m
γ_N	gyromagnetic ratio of the neutron	1.913

Table E.1: Symbols and values of physical quantities used in this thesis

List of Figures

List of Tables

Bibliography

[Åke] J. Åkerman. Toward a universal memory. *Science, 308(5721):508-510, 2005.*

[And] P. W. Anderson. New Approach to the Theory of Superexchange Interactions. *Phys. Rev., 115:2-13, Jul 1959.*

[ASD$^+$] E. Altynbaev, S.-A. Siegfried, V. Dyadkin, E. Moskvin, D. Menzel, A. Heinemann, C. Dewhurst, L. Fomicheva, A. Tsvyashchenko, and S. Grigoriev. Intrinsic instability of the helix spin structure in MnGe and order-disorder phase transition. *Phys. Rev. B, 90:174420, Nov 2014*.

[Bara] L. D. Barron. Molecular light scattering and optical activity. *Cambridge University Press, second edition, Cambridge Books Online, 2004*.

[Barb] L. D. Barron. True and false chirality and absolute asymmetric synthesis. *Journal of the American Chemical Society 108(18):5539-5542, 1986.*

[Bera] L. Berger. Emission of spin waves by a magnetic multilayer traversed by a current. *Phys. Rev. B, 54:9353-9358, Oct 1996.*

[Berb] L. Berger. Possible existence of a Josephson effect in ferromagnets. *Phys. Rev. B, 33:1572-1578, Feb 1986.*

[BJ] P. Bak and M. H. Jensen. Theory of helical magnetic structures and phase transitions in MnSi and FeGe. *Journal of Physics C: Solid State Physics, 13(31):L881, 1980*.

[Blu] M. Blume. Polarization Effects in the Magnetic Elastic Scattering of Slow Neutrons. *Phys. Rev., 130:1670-1676, Jun 1963*.

[BM] S. E. Barnes and S. Maekawa. Current-spin coupling for ferromagnetic domain walls in fine wires. *Phys. Rev. Lett., 95:107204, Sep 2005.*

[Broa] P. J. Brown. Polarised neutrons and complex antiferromagnets: an overview. *Physica B: Condensed Matter, 297(14):198-203, 2001. Proceeding of the Third International Workshop on Polarised Neutrons.*

[Brob] P. J. Brown. Spherical Neutron Polarimetry in T. Chatterji (Ed.) Neutron Scattering from Magnetic Materials. *Elsevier Science, 2005.*

[BRP] A.N. Bogdanov, U.K. Rössler, and C. Pfleiderer. Modulated and localized structures in cubic helimagnets. *Physica B: Condensed Matter, 359-361:1162-1164, 2005. Proceedings of the International Conference on Strongly Correlated Electron Systems.*

[BVR] J. Beille, J. Voiron, and M. Roth. Long period helimagnetism in the cubic B20 $Fe_{1-x}Co_xSi$ and $Co_xMn_{1-x}Si$ alloys. *Solid State Communications, 47(5):399-402, 1983.*

[BVT+] J. Beille, J. Voiron, F. Towfiq, M. Roth, and Z. Y. Zhang. Helimagnetic structure of the $Fe_{1-x}Co_xSi$ alloys. *Journal of Physics F: Metal Physics, 11(10):2153, 1981.*

[Car] L. Caroll. Through the Looking-Glass. *Macmillan, 1871.*

[CXYL] J. P. Chen, Y. L. Xie, Z. B. Yan, and J.-M. Liu. Tunable magnetic helicity in $Mn_{1-x}Fe_xGe$: A Monte Carlo simulation. *Journal of Applied Physics, 117(17), 2015.*

[Czo] J. Czochralski. Ein neues Verfahren zur Messung der Kristallisationsgeschwindigkeit der Metalle. *Zeitschrift für Physikalische Chemie 92, 219-221, 1918.*

[d22] D22. `http://www.ill.eu/d22/`. Accessed: 2015-08-10.

[DBT+] M. Deutsch, P. Bonville, A. V. Tsvyashchenko, L. N. Fomicheva, F. Porcher, F. Damay, S. Petit, and I. Mirebeau. Stress-induced magnetic textures and fluctuating chiral phase in MnGe chiral magnet. *Phys. Rev. B, 90:144401, Oct 2014.*

[DCGD] V. Dmitriev, D. Chernyshov, S. Grigoriev, and V. Dyadkin. A chiral link between structure and magnetism in MnSi. *Journal of Physics: Condensed Matter, 24(36):366005, 2012.*

[Deb] P. Debye. Interferenz von Röntgenstrahlen und Wärmebewegung. *Annalen der Physik, 348(1):49-92, 1913.*

[Dew] C. D. Dewhurst. Grasp. `http://www.ill.eu/lss/grasp/`. Accessed: 2015-10-08.

[DGM+] V. A. Dyadkin, S. V. Grigoriev, D. Menzel, D. Chernyshov, V. Dmitriev, J. Schoenes, S. V. Maleyev, E. V. Moskvin, and H. Eckerlebe. Control of chirality of transition-metal monosilicides by the Czochralski method. *Phys. Rev. B, 84:014435, Jul 2011.*

[DGO+] V. Dyadkin, S. Grigoriev, S. V. Ovsyannikov, E. Bykova, L. Dubrovinsky, A. Tsvyashchenko, L.N. Fomicheva, and D. Chernyshov. Crystal structure and thermal expansion of $Mn_{1-x}Fe_xGe$. *Acta Crystallographica Section B, 70(4):676-680, Aug 2014.*

[DMH+] M. Deutsch, O. L. Makarova, T. C. Hansen, M. T. Fernandez-Diaz, V. A. Sidorov, A. V. Tsvyashchenko, L. N. Fomicheva, F. Porcher, S. Petit, K. Koepernik, U. K. Rößler, and I. Mirebeau. Two-step pressure-induced collapse of magnetic order in the MnGe chiral magnet. *Phys. Rev. B, 89:180407, May 2014.*

[DPDC] V. Dyadkin, P. Pattison, V. Dmitriev, and D. Chernyshov. A new multipurpose diffractometer PILATUS@SNBL. *Journal of Synchrotron Radiation, 23(3):825-829, May 2016.*

[DPG+] V. Dyadkin, K. Prša, S. V. Grigoriev, J. S. White, P. Huang, H. M. Rønnow, A. Magrez, C. D. Dewhurst, and D. Chernyshov. Chirality of structure and magnetism in the magnetoelectric compound Cu_2OSeO_3. *Phys. Rev. B, 89:140409, Apr 2014.*

[Dya] V. A. Dyadkin. SNBL Tool Box, Release 2013-1. *Swiss Norwegian Beam Lines at ESRF, Grenoble, France, 2013.*

[Dzya] I. E. Dzyaloshinskii. Theory of Helicoidal Structures in Antiferromagnets. I. Nonmetals. *Zh. Eksp. Teor. Fiz., 46:1420, 1964 [Sov. Phys. JETP 19, 960 (1964)].*

[Dzyb] I. Dzyaloshinsky. A thermodynamic theory of weak ferromagnetism of antiferromagnetics. *Journal of Physics and Chemistry of Solids, 4(4):241-255, 1958.*

[ESR] ESRF. BM01A Beamline . `http://www.esrf.eu/UsersAndScience/Experiments/CRG/BM01/bm01-a`. Accessed: 2015-08-24.

[EWP+] W. Eerenstein, M. Wiora, J. L. Prieto, J. F. Scott, and N. D. Mathur. Giant sharp and persistent converse magnetoelectric effects in multiferroic epitaxial heterostructures. *Nat Mater, 6(5):1476-1122, 2007.*

[FB] H. D. Flack and G. Bernardinelli. Absolute structure and absolute configuration. *Acta Crystallographica Section A, 55(5):908-915, Sep 1999.*

[FCS] A. Fert, V. Cros, and J. Sampaio. Skyrmions on the track. *Nat Nano, 8:152-156, March 2013.*

[Fla] H. D. Flack. On enantiomorph-polarity estimation. *Acta Crystallographica Section A, 39(6):876-881, Nov 1983.*

[FYN$^+$] S. Fukami, M. Yamanouchi, Y. Nakatani, K.-J. Kim, T. Koyama, D. Chiba, S. Ikeda, N. Kasai, T. Ono, and H. Ohno. Distribution of critical current density for magnetic domain wall motion. *Journal of Applied Physics, 115(17), 2014.*

[GCD$^+$a] S. V. Grigoriev, D. Chernyshov, V. A. Dyadkin, V. Dmitriev, S. V. Maleyev, E. V. Moskvin, D. Menzel, J. Schoenes, and H. Eckerlebe. Crystal Handedness and Spin Helix Chirality in $\mathrm{Fe}_{1-x}\mathrm{Co}_x\mathrm{Si}$. *Phys. Rev. Lett., 102:037204, Jan 2009.*

[GCD$^+$b] S. V. Grigoriev, D. Chernyshov, V. A. Dyadkin, V. Dmitriev, E. V. Moskvin, D. Lamago, Th. Wolf, D. Menzel, J. Schoenes, S. V. Maleyev, and H. Eckerlebe. Interplay between crystalline chirality and magnetic structure in $\mathrm{Mn}_{1-x}\mathrm{Fe}_x\mathrm{Si}$. *Phys. Rev. B, 81:012408, Jan 2010.*

[GFS$^+$] J. Gayles, F. Freimuth, T. Schena, G. Lani, P. Mavropoulos, R. A. Duine, S. Blügel, J. Sinova, and Y. Mokrousov. Dzyaloshinskii-Moriya Interaction and Hall Effects in the Skyrmion Phase of $\mathrm{Mn}_{1-x}\mathrm{Fe}_x\mathrm{Ge}$. *Phys. Rev. Lett., 115:036602, Jul 2015.*

[GGa] R. Gähler and R. Golub. Neutron resonance spin echo, bootstrap method for increasing the effective magnetic field. *J. Phys. France, 49(7), 1988.*

[GGb] R. Golub and R. Gähler. A neutron resonance spin echo spectrometer for quasi-elastic and inelastic scattering. *Physics Letters A, 123(1):43-48, 1987.*

[GGK] R. Gähler, R. Golub, and T. Keller. A plane wave approach to particle beam magnetic resonance. *Am. J. Phys., 62, 1994.*

[GGS] M. Goldhaber, L. Grodzins, and A. W. Sunyar. Helicity of Neutrinos. *Phys. Rev., 109:1015-1017, Feb 1958.*

[GMD+a] S. V. Grigoriev, S. V. Maleyev, V. A. Dyadkin, D. Menzel, J. Schoenes, and H. Eckerlebe. Principal interactions in the magnetic system $Fe_{1-x}Co_xSi$: Magnetic structure and critical temperature by neutron diffraction and SQUID measurements. *Phys. Rev. B, 76:092407, Sep 2007.*

[GMD+b] S. V. Grigoriev, E. V. Moskvin, V. A. Dyadkin, D. Lamago, T. Wolf, H. Eckerlebe, and S. V. Maleyev. Chiral criticality in the doped helimagnets $Mn_{1-x}Fe_xSi$. *Phys. Rev. B, 83:224411, Jun 2011.*

[GMO+] S. V. Grigoriev, S. V. Maleyev, A. I. Okorokov, Yu. O. Chetverikov, P. Böni, R. Georgii, D. Lamago, H. Eckerlebe, and K. Pranzas. Magnetic structure of MnSi under an applied field probed by polarized small-angle neutron scattering. *Phys. Rev. B, 74:214414, Dec 2006.*

[GOP] R. Gilles, A. Ostermann, and W. Petry. Monte Carlo simulations of the new small-angle neutron scattering instrument SANS-1 at the Heinz Maier-Leibnitz Forschungsneutronenquelle. *Journal of Applied Crystallography, 40(s1):s428-s432, Apr 2007.*

[GOS+] R. Gilles, A. Ostermann, C. Schanzer, B. Krimmer, and W. Petry. The concept of the new small-angle scattering instrument SANS-1 at the FRM-II. *Physica B: Condensed Matter, 385386, Part 2(0):1174 -1176, 2006. Proceedings of the Eighth International Conference on Neutron Scattering.*

[GP] C. Grande and N. H. Patel. Nodal signalling is involved in left-right asymmetry in snails. *Nature, 457:1007-1011, Oct 2009.*

[GPS+a] S. V. Grigoriev, N. M. Potapova, S.-A. Siegfried, E. V. Altynbaev, V. A. Dyadkin, E. V. Moskvin, V. Dmitriev, D. Menzel, C. D. Dewhurst, A. V. Tsvyashchenko, and D. Chernyshov. Spin chirality of transition metal monogermanides. *Flipper: International Workshop on Single-Crystal Diffraction with Polarised Neutrons, Jan. 2013*.

[GPS+b] S. V. Grigoriev, N. M. Potapova, S.-A. Siegfried, V. A. Dyadkin, E. V. Moskvin, V. Dmitriev, D. Menzel, C. D. Dewhurst, D. Chernyshov, R. A. Sadykov, L. N. Fomicheva, and A. V. Tsvyashchenko. Chiral Properties of Structure and Magnetism in $Mn_{1-x}Fe_xGe$ Compounds: When the Left and the Right are Fighting, Who Wins? *Phys. Rev. Lett., 110:207201, May 2013.*

[Gri] I. Grillo. Small-Angle Neutron Scattering and Applications in Soft Condensed Matter in Borsali, Pecore (Eds.) Soft matter charaterization. *Springer, 2008.*

[GS] C. N. Guy and J. O. StromOlsen. Magnetic anisotropy in manganese silicide. *Journal of Applied Physics, 50(B3), 1979.*

[GSA$^+$] S. V. Grigoriev, S.-A. Siegfried, E. V. Altynbayev, N. M. Potapova, V. Dyadkin, E. V. Moskvin, D. Menzel, A. Heinemann, S. N. Axenov, L. N. Fomicheva, and A. V. Tsvyashchenko. Flip of spin helix chirality and ferromagnetic state in $\mathrm{Fe}_{1-x}\mathrm{Co}_x\mathrm{Ge}$ compounds. *Phys. Rev. B, 90:174414, Nov 2014.*

[GSM] S. V. Grigoriev, A. S. Sukhanov, and S. V. Maleyev. From spiral to ferromagnetic structure in B20 compounds: Role of cubic anisotropy. *Phys. Rev. B, 91:224429, Jun 2015.*

[Hah] T. Hahn. (Ed.) International Tables for Crystallography A, 5th ed. *Wiley, 2005.*

[Ham] A. Hammersley. FIT2D. *Internal Report ESRF97HA02T. European Synchrotron Radiation Facility, Grenoble, France, 1997.*

[HDH$^+$] W. Heil, J. Dreyer, D. Hofmann, H. Humblot, E. Lelievre-Berna, and F. Tasset. 3He neutron spin-filter. *Physica B: Condensed Matter, 267268(0):328-335, 1999.*

[Hei] W. Heisenberg. Zur Theorie des Ferromagnetismus. *Zeitschrift für Physik, 49:619-636, September 1928.*

[Her] R. P. Hermann. Spin Dependent and Magnetic Scattering in Brückel, Heger, Richter, Roth, Zorn (Eds.) Laboratory Course: Neutron Scattering. *Forschungszentrum Jülich GmbH, 2013.*

[IEM$^+$] M. Ishida, Y. Endoh, S. Mitsuda, Y. Ishikawa, and M. Tanaka. Crystal Chirality and Helicity of the Helical Spin Density Wave in MnSi. II. Polarized Neutron Diffraction. *Journal of the Physical Society of Japan, 54(8):2975-2982, 1985.*

[IKB] Y. Ishikawa, T. Komatsubara, and D. Bloch. Magnetic phase diagram of MnSi. *Physica B+C, 8688, Part 1(0):401-403, 1977.*

[ITBR] Y. Ishikawa, K. Tajima, D. Bloch, and M. Roth. Helical spin structure in manganese silicide MnSi. *Solid State Communications, 19(6):525-528, 1976.*

[Jen] J. Jensen. Rare Earth Magnetism: Structures and Excitations. *Clarendon Press, Oxford, 1991.*

[JMP$^+$] F. Jonietz, S. Mühlbauer, C. Pfleiderer, A. Neubauer, W. Münzer, A. Bauer, T. Adams, R. Georgii, P. Böni, R. A. Duine, K. Everschor, M. Garst, and A. Rosch. Spin Transfer Torques in MnSi at Ultralow Current Densities. *Science, 330(6011):1648-1651, 2010.*

[Jou] J. P. Joule. On the effects of magnetism upon the dimensions of iron and steel bars. *Philos. Mag., 30:76-87, 1847.*

[Kap] T. A. Kaplan. Classical spin-configuration stability in the presence of competing exchange forces. *Phys. Rev., 116:888-889, Nov 1959*.

[Kel] W. T. Kelvin. Baltimore Lectures. *J. C. Clay and Sons, London, 1804.*

[KKI$^+$] N. Kanazawa, J.-H. Kim, D. S. Inosov, J. S. White, N. Egetenmeyer, J. L. Gavilano, S. Ishiwata, Y. Onose, T. Arima, B. Keimer, and Y. Tokura. Possible skyrmion-lattice ground state in the $B20$ chiral-lattice magnet MnGe as seen via small-angle neutron scattering. *Phys. Rev. B, 86:134425, Oct 2012.*

[KNA] T. Koretsune, N. Nagaosa, and R. Arita. Control of Dzyaloshinskii-Moriya interaction in $Mn_{1-x}Fe_xGe$: a first-principles study. *Scientific Reports, 5:13302, August 2015.*

[KOA$^+$] N. Kanazawa, Y. Onose, T. Arima, D. Okuyama, K. Ohoyama, S. Wakimoto, K. Kakurai, S. Ishiwata, and Y. Tokura. Large Topological Hall Effect in a Short-Period Helimagnet MnGe. *Phys. Rev. Lett., 106:156603, Apr 2011.*

[KVN] L. G. Khvostantsev, L. F. Vereshchagin, and A. P. Novikov. Device of toroid type for high pressure generation. *High Temp.- High Pressures, 9:637-639, 1977.*

[LB] S. W. Lovesey and E. Balcar. The scattering of polarized neutrons by a magnetic material. *Physica B: Condensed Matter, 267268(0):221-226, 1999.*

[LBA$^+$] L. Ludgren, O. Beckman, V. Attia, S. P. Bhattacheriee, and M. Richardson. Helical Spin Arrangement in Cubic FeGe. *Physica Scripta, 1(1):69, 1970.*

[LBF] B. Lebech, J. Bernhard, and T. Freltoft. Magnetic structures of cubic FeGe studied by small-angle neutron scattering. *Journal of Physics: Condensed Matter, 1(35):6105, 1989.*

[LL] L. D. Landau and E. M. Lifshits. Quantum Mechanics: Non-relativistic Theory. *Butterworth-Heinemann, 1977.*

[Lov] S. W. Lovesey. Theory of Neutron Scattering from Condensed Matter Vol.I/II. *Cambridge University Press, 2004.*

[LY] T. D. Lee and C. N. Yang. Question of Parity Conservation in Weak Interactions. *Phys. Rev., 104:254-258, Oct 1956.*

[LZ] Z. Li and S. Zhang. Domain-wall dynamics and spin-wave excitations with spin-transfer torques. *Phys. Rev. Lett., 92:207203, May 2004.*

[Mala] S. V. Maleev. Polarized neutron scattering in magnets. *Physics-Uspekhi, 45(6):569, 2002.*

[Malb] S. V. Maleyev. Cubic magnets with Dzyaloshinskii-Moriya interaction at low temperature. *Phys. Rev. B, 73:174402, May 2006.*

[MBS] S. V. Maleyev, V. G. Baryahtar, and R. A. Suris. *Fiz. Tverd. Tela (Leningrad) 4, 3461 (1962) [Sov. Phys. Solid State., 4:2533, 1963].*

[MGD+] E. Moskvin, S. Grigoriev, V. Dyadkin, H. Eckerlebe, M. Baenitz, M. Schmidt, and H. Wilhelm. Complex Chiral Modulations in FeGe Close to Magnetic Ordering. *Phys. Rev. Lett., 110:077207, Feb 2013.*

[MHW+] S. Mühlbauer, A. Heinemann, A. Wilhelm, L. Karge, A. Ostermann, I. Defendi, A. Schreyer, W. Petry, and R. Gilles. The new small-angle neutron scattering instrument SANS-1 at MLZ - characterization and first results. *Nuclear Instruments and Methods in Physics Research Section A: Accelerators, Spectrometers, Detectors and Associated Equipment, 832:297-305, 2016.*

[Mor] T. Moriya. Anisotropic Superexchange Interaction and Weak Ferromagnetism. *Phys. Rev., 120:91-98, Oct 1960.*

[MRK] R. M. Moon, T. Riste, and W. C. Koehler. Polarization Analysis of Thermal-Neutron Scattering. *Phys. Rev., 181:920-931, May 1969.*

[MSD+] N. Manyala, Y. Sidis, J. F. DiTusa, G. Aeppli, D.P. Young, and Z. Fisk. Magnetoresistance from quantum interference effects in ferromagnets. *Nature, 404:581-584, 2000.*

[MSK$^+$] D. Morikawa, K. Shibata, N. Kanazawa, X. Z. Yu, and Y. Tokura. Crystal chirality and skyrmion helicity in MnSi and (Fe, Co)Si as determined by transmission electron microscopy. *Phys. Rev. B, 88:024408, Jul 2013.*

[MTA$^+$] O. L. Makarova, A. V. Tsvyashchenko, G. Andre, F. Porcher, L. N. Fomicheva, N. Rey, and I. Mirebeau. Neutron diffraction study of the chiral magnet MnGe. *Phys. Rev. B, 85:205205, May 2012.*

[MYS$^+$] M. Mochizuki, X. Z. Yu, S. Seki, N. Kanazawa, W. Koshibae, J. Zang, M. Mostovoy, Y. Tokura, and N. Nagaosa. Thermally driven ratchet motion of a skyrmion microcrystal and topological magnon Hall effect. *Nat Mater, 13:241-246, Oct 2014.*

[Nob] The Nobel Prize in Chemistry 2001. `http://www.nobelprize.org/nobel_prizes/chemistry/laureates/2001/`. Accessed: 2015-08-10.

[Now] E. Nowak. Scattering of slow neutrons by bound nuclei. *Zeitschrift für Physik B Condensed Matter, 45(3):265-271, 1982.*

[NYHK] O. Nakanishi, A. Yanase, A. Hasegawa, and M. Kataoka. The origin of the helical spin density wave in MnSi. *Solid State Communications, 35(12):995-998, 1980.*

[Par] S. S. P. Parkin. Shiftable magnetic shift register and method of using the same, December 21 2004. US Patent 6,834,005.

[Pas] L. Pasteur. On the Relationships between the Crystalline Form, Chemical Composition and the Direction of Optical Rotation. *Annales de Chimie et de Physique, 24(6):442-459, 1948.*

[PHT] S. S. P. Parkin, M. Hayashi, and L. Thomas. Magnetic domain-wall racetrack memory. *Science, 320(5873):190-194, 2008.*

[PJK$^+$] S. Parkin, Xin Jiang, C. Kaiser, A. Panchula, K. Roche, and M. Samant. Magnetically engineered spintronic sensors and memory. *Proceedings of the IEEE, 91(5):661-680, May 2003.*

[PPM] J. S. Pedersen, D. Posselt, and K. Mortensen. Analytical treatment of the resolution function for small-angle scattering. *Journal of Applied Crystallography, 23(4):321-333, Aug 1990.*

[PS] L. Passell and R. I. Schermer. Measurement of the Spin Dependence of the $\mathrm{He}^3(n,p)\mathrm{T}$ Reaction and of the Nuclear Susceptibility of Adsorbed He^3. *Phys. Rev., 150:146-151, Oct 1966.*

[RC] J. Rodriguez-Carvajal. Recent advances in magnetic structure determination by neutron powder diffraction. *Physica B: Condensed Matter, 192(12):55-69, 1993.*

[RHM+] N. Romming, C. Hanneken, M. Menzel, J. E. Bickel, B. Wolter, K. von Bergmann, A Kubetzka, and R. Wiesendanger. Writing and Deleting Single Magnetic Skyrmions. *Science, 341(6146):636-639,2013.*

[Rob] R. T. Robiscoe. A spin flip problem. *American Journal of Physics, 39(2), 1971*.

[SAC+] S.-A. Siegfried, E. V. Altynbaev, N. M. Chubova, V. Dyadkin, D. Chernyshov, E. V. Moskvin, D. Menzel, A. Heinemann, A. Schreyer, and S. V. Grigoriev. Controlling the Dzyaloshinskii-Moriya interaction to alter the chiral link between structure and magnetism for $Fe_{1-x}Co_xSi$. *Phys. Rev. B, 91:184406, May 2015.*

[SAMM] G. Shirane, J. D. Axe, C. F. Majkrzak, and T. Mizoguchi. Magnetic excitations in amorphous ferromagnets. *Phys. Rev. B, 26:2575-2583, Sep 1982.*

[san] SANS-1: Small angle neutron scattering. *Journal of large-scale research facilities, 1, A10, 2015*.

[Sch] O. Schärpf. Polarization analysis techniques for quasielastic neutron scattering. *Physica B: Condensed Matter, 182(4):376-388, 1992.Quasielastic Neutron Scattering.*

[Sea] V. F. Sears. Neutron scattering lengths and cross sections. *Neutron News, 3(3):26-37, 1992.*

[She] G. M. Sheldrick. A short history of *SHELX*. *Acta Crystallographica Section A, 64(1):112-122, Jan 2008.*

[Shu] C. G. Shull. Production of Highly Polarized Neutron Beams by Bragg Reflection from Ferromagnetic Crystals. *Phys. Rev., 81:626-626, Feb 1951.*

[Sky] T. H. R. Skyrme. A unified field theory of mesons and baryons. *Nuclear Physics, 31:556-569, 1962.*

[Slo] J. C. Slonczewski. Current-driven excitation of magnetic multilayers. *Journal of Magnetism and Magnetic Materials, 159(1):L1-L7, 1996.*

[Squ] G. L. Squires. Introduction to the Theory of Thermal Neutron Scattering. *Cambridge University Press, 2012.*

[SSF] U. Shmueli, M. Schiltz, and H. D. Flack. Intensity statistics of Friedel opposites. *Acta Crystallographica Section A, 64(4):476483, Jul 2008.*

[SYH+] K. Shibata, X. Z. Yu, T. Hara, D. Morikawa, N. Kanazawa, K. Kimoto, S. Ishiwata, Y. Matsui, and Y. Tokura. Towards control of the size and helicity of skyrmions in helimagnetic alloys by spin-orbit coupling. *Nat Nano, 8:723-728, 2013.*

[TBLB+] F. Tasset, P. J. Brown, E. Lelivre-Berna, T. Roberts, S. Pujol, J. Allibon, and E. Bourgeat-Lami. Spherical neutron polarimetry with Cryopad-II. *Physica B: Condensed Matter, 267268(0):69-74, 1999.*

[Tec] Agilent Technologies. CrysAlisPro software system. *Oxford(UK): Agilent Technologies UK Ltd. 2013.*

[TK] G. Tatara and H. Kohno. Theory of current-driven domain wall motion: Spin transfer versus momentum transfer. *Phys. Rev. Lett.,92:086601, Feb 2004.*

[TNMS] A. Thiaville, Y. Nakatani, J. Miltat, and Y. Suzuki. Micromagnetic understanding of current-driven domain wall motion in patterned nanowires. *EPL (Europhysics Letters), 69(6):990, 2005.*

[TR] F. Tasset and E. Ressouche. Optimum transmission for a 3He neutron polarizer. *Nuclear Instruments and Methods in Physics Research Section A: Accelerators, Spectrometers, Detectors and Associated Equipment, 359(3):537-541, 1995.*

[TSES] H. Takizawa, T. Sato, T. Endo, and M. Shimada. High-pressure synthesis and electrical and magnetic properties of MnGe and CoGe with the cubic B20 structure. *Journal of Solid State Chemistry, 73(1):40-46, 1988.*

[TSF+] A. V. Tsvyashchenko, V.A. Sidorov, L.N. Fomicheva, V.N. Krasnorussky, R.A. Sadykov, J.D. Thompson, K. Gofryk, F. Ronning, and V.Y. Ivanov. High Pressure Synthesis and Magnetic Properties of Cubic B20 MnGe and CoGe. *Solid State Phenomena, 190:225-228, June 2012.*

[Tsv] A. V. Tsvyashchenko. High pressure synthesis of RE_6Cu_{23} compounds (RE, Tb, Dy, Yb, Lu). *Journal of the Less Common Metals, 99(2):L9-L11, 1984.*

[TTIE] M. Tanaka, H. Takayoshi, M. Ishida, and Y. Endoh. Crystal Chirality and Helicity of the Helical Spin Density Wave in MnSi. I. Convergent-Beam Electron Diffraction. *Journal of the Physical Society of Japan, 54(8):2970-2974, 1985.*

[Vil] J. Villain. La structure des substances magnetiques. *Journal of Physics and Chemistry of Solids, 11(3):303-309, 1959*.

[Wag] G. H. Wagnière. On chirality and the universal asymmetry. *Helvetica Chimica Acta [u.a.], 2007.*

[WAH$^+$] C. S. Wu, E. Ambler, R. W. Hayward, D. D. Hoppes, and R. P. Hudson. Experimental Test of Parity Conservation in Beta Decay. *Phys. Rev., 105:1413-1415, Feb 1957.*

[Wal] I. Waller. Zur Frage der Einwirkung der Wärmebewegung auf die Interferenz von Röntgenstrahlen. *Zeitschrift für Physik, 17(1):398- 408, 1923.*

[WH] R. Wäppling and L.S Häggström. Mössbauer study of cubic FeGe. *Physics Letters A, 28(3):173-174, 1968.*

[WSCG$^+$] H. Wilhelm, M. Schmidt, R. Cardoso-Gil, U. Burkhardt, M. Hanfland, U. Schwarz, and L. Akselrud. Structural investigations of ε-FeGe at high pressure and low temperature. *Science and Technology of Advanced Materials, 8(5):416, 2007.*

[Yos] A. Yoshimori. A new type of antiferromagnetic structure in the rutile type crystal. *Journal of the Physical Society of Japan, 14(6):807-821, 1959*.

[ZL] S. Zhang and Z. Li. Roles of nonequilibrium conduction electrons on the magnetization dynamics of ferromagnets. *Phys. Rev. Lett., 93:127204, Sep 2004.*

Eidesstattliche Versicherung

Hiermit erkläre ich an Eides statt, dass ich die vorliegende Dissertationsschrift selbst verfasst und keine anderen als die angegebenen Quellen und Hilfsmittel benutzt habe.

Hamburg, den 12.09.2016

Sven-Arne Siegfried

Acknowledgements

I would like to thank all people who supported me through the last years and made this thesis possible:

- Prof. Andreas Schreyer for giving me the opportunity to work in your group at the Helmholtz-Zentrum Geesthacht. Thank you for always supporting and discuss my research and giving me the freedom to work on my own ideas.
- Prof. Sergey V. Grigoriev for introducing me to neutron scattering and chiral magnetism. Thank you for all the interesting discussions, the work with you was a great pleasure. In addition, I would like to thank you for the invitation to your working group at the Petersburg Nuclear Physics Institute in Gatchina, which was a great experience and a very fruitful period during my Phd time.
- Dieter Lott for your help and support and especially for the proofreading, and very useful editorial advices for this manuscript.
- Nadya M. Chubova, Evgeny V. Altynbaev and Evgeny V. Moskvin for your help and the nice company throughout the various experiments, conferences and workshops we spent together.
- André Heinemann, Sebastian Mühlbauer, Andreas Wilhelm, Svatopluk Semecky and Sebastian Busch for your support during our numerous days of measurement at SANS-1 and for granting us additional internal beamtime.
- Charles D. Dewhurst and Dirk Honecker for your assistance during all our SANS experiments at the ILL.
- Dirk Menzel for all the SQUID measurements performed in your work group at the Institute for Condensed Matter Physics at the TU Braunschweig.
- Vadim A. Dyadkin, Dmitry Chernyshov and Prof. Vladimir Dmitriev for the single crystal and powder x-ray diffraction measurement at the ESRF.

- Anatoly V. Tsvyashchenko, Ravil A. Sadykov, Sergey N. Axenov and Ludmila N. Formicheva for the high pressure synthesis of all the $Mn_{1-x}Fe_xGe$ and $Fe_{1-y}Co_yGe$ compounds at the Institute for high pressure physics in Troisk.

- Dirk Menzel and Vadim A. Dyadkin for your support during the Czochralski-growing of the single crystalline $Fe_{1-z}Co_zSi$ samples at the Institute for Condensed Matter Physics at the TU Braunschweig.

- Prof. Sergey V. Maleyev and Alexander S. Suhkanov for you theoretical work, clarifying the important role of the cubic anisotropy.

- The technical staff from the MLZ and ILL for the support during our experiments, without which our experiments would have been hardly possible.

- Jean-Francois Moulin, Martin Haese and Matthias Pomm for your help during the REFSANS experiments.

- My colleagues at the MLZ, especially from the HZG outstation for the nice working atmosphere during the last years.

- My family for all your support far in excess of this thesis.

- Lorena for your love, patience and support.